Department of Precision and Microsystems Engineering

Optimized MEMS-based Nanoreactor for *In-Situ* Transmission Electron Microscopy Studies at High Temperature and Atmospheric Pressure

Ronald Gerardus Spruit

Report no : 2017.045
Coaches : Dr. M.K. Ghatkesar, Dr. H.H. Pérez Garza
Professor : Dr. Ir. M. Tichem
Specialisation : Micro and Nano Engineering
Type of Report : Master Thesis
Date : September 29, 2017

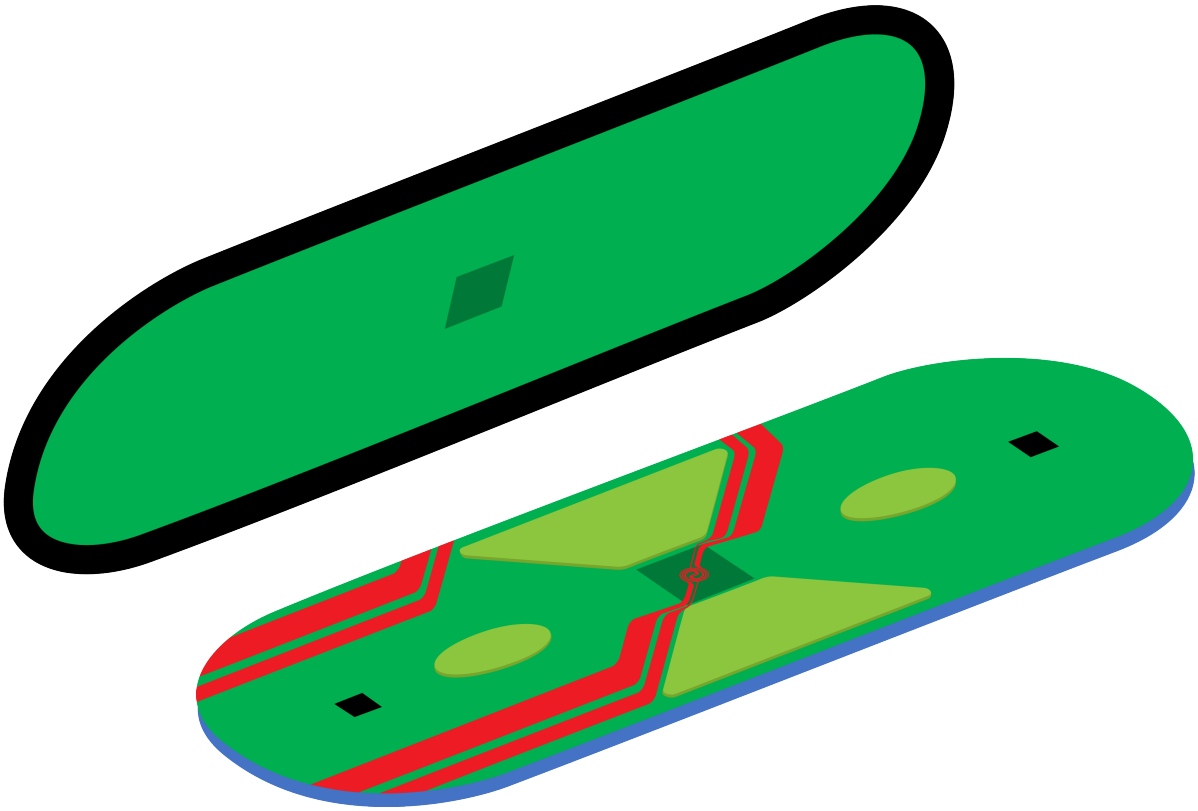

Optimized MEMS-based Nanoreactor for *In-Situ* Transmission Electron Microscopy Studies at High Temperature and Atmospheric Pressure

by

Ronald Gerardus Spruit

to obtain the degree of Master of Science

at the Delft University of Technology,

to be defended publicly on Friday September 29, 2017 at 12.45 PM.

Student number: 4148789

Project duration: September 1, 2016 – September 29, 2017

Thesis committee:

Dr. Ir. M. Tichem	3mE, PME, Micro and Nano Engineering
Dr. M. K. Ghatkesar	3mE, PME, Micro and Nano Engineering
Prof. Dr. P. G. Steeneken	3mE, PME, Dynamics of Micro and Nano Systems
Prof. Dr. P. J. French	EWI, ME, Electronic Instrumentation
Dr. H. H. Pérez Garza	DENSsolutions B.V.

This thesis is confidential and cannot be made public until September 29, 2019.

TU Delft

DENS solutions

Abstract

Transmission electron microscopy (TEM) is a powerful and commonly used tool to study nanoparticles, nanowires, and 2D materials. It provides static information on a sample with atomic resolution, in high vacuum and at ambient temperature. However, in real processes, the environment is often different and dynamic. MEMS-based sample carriers became a breakthrough for *in-situ* TEM where they function as a micro-sized laboratory. The Nanoreactor allows for manipulation of samples by simultaneously applying heat and gas stimuli, which enables real-time studies of solid-gas interactions inside the TEM.

Depending on the nature and type of experiment, the thermo-electro-mechanical performance of the Nanoreactor is not always sufficient for rapid dynamic studies. The stimuli do not only affect the sample, but they also affect the Nanoreactor performance and suffer from undefined settling trajectories. These lead to operational inconveniences as well as limited possibilities for science. Reducing the Nanoreactor's sensitivity to stimuli and improving its response time would open up the door to new applications and will help to study fast dynamic processes in more detail and with higher accuracy.

To find out which mechanisms are currently limiting real-time TEM imaging, and to identify potential solutions, a literature review was performed to study the state of the art in MEMS heating and gas flow technology. The encountered technological advancements and the relevant underlying physics were translated into a set of design guidelines that enable the design of an optimized Nanoreactor. Next to that, it was concluded that the Nanoreactor operates in various transition regimes in between thermal advection or diffusion, laminar or molecular flow, and gas advection or diffusion.

In this project, the electro-thermo-mechanical behavior of the Nanoreactor is characterized using various analytical techniques. These had to be selected carefully, as the tiny scale and the extreme conditions at which the Nanoreactor must operate, limit the number of suitable tools to characterize and help understand its behavior. The obtained results are used to develop a finite element model that simulates the behavior of the Nanoreactor. Using the acquired theoretical knowledge and the predictions from the model, an optimized Nanoreactor design is proposed that improves membrane deflection from 22 µm to 9.3 µm, spatial sample drift (through reducing the power consumption by 43–50 %), temperature homogeneity from 93.9 % to 97.7 %, temperature stability by 9.8 %, gas flow speed from 4.3 $\mathrm{cm\,s^{-1}}$ to 33.1 $\mathrm{cm\,s^{-1}}$ and gas switching time from 2.9 s to 0.175 s. The obtained improvements in homogeneity, stability and gas switching make sure the sample experiences more accurately defined stimuli such that it is known exactly under which circumstances the investigated phenomena occur. The improvements on deflection and drift reduce the loss of focus and ease tracing of the sample, which effectively allows to exploit higher magnifications and to obtain higher quality results on rapid solid-gas interactions inside the TEM.

Preface

This thesis is the record of my master project. The project was conducted mostly at DENSsolutions B.V. and partially within the group of Micro and Nano Engineering at the faculty of Mechanical Engineering. Short experiments were conducted at The National Centre for High Resolution Electron Microscopy (faculty of Applied Sciences) and Novel Aerospace Materials (faculty of Aerospace Engineering).

First of all, I would like to express my appreciation to the committee members that are willing to examine my work: Marcel Tichem, Murali Ghatkesar, Peter Steeneken, Paddy French, and Hugo Pérez Garza.

During my project, Hugo was my daily supervisor at DENSsolutions. He provided me with the opportunity to do my thesis project on a topic that involves all the subjects that have fascinated me the most throughout my studies. Optimizing the Nanoreactor design allowed me to explore multiple types of physics and acquire experience with various experimental characterization techniques. At the same time, I could stay in touch with my interests in elementary particles through the involvement of SEM and TEM. I would like to thank him for allowing me to shape and guide my own project towards the topics that I found most interesting, for giving me the chance to contribute to and co-author a paper [1], for letting me visit the International Micro-NanoConference and the Vision Dynamics Nano-Fabrication, Devices & Metrology Workshop, and above all, for making me part of his team, and for his genuine support, motivation and enthusiasm which really made this a very enjoyable year. I could not have wished for a nicer and more supportive supervisor.

The triweekly meetings with Murali, my supervisor from the Micro and Nano Engineering group, manifest themselves strongest in the structure of this thesis project. I always enjoyed our meetings that varied from deep technical discussions to asking me the right questions that forced me to take a step back and not lose track of the covering goal and research questions. These meetings deviated more than occasionally from the thesis subject, taught me a lot about the scientific community, and often took much longer than the hour that was planned for them. I would like to thank Murali for all his support, insights and knowledge that have definitely raised the quality of my work.

Throughout this project, I received a lot of help from Tijn van Omme, directly and indirectly. He trained me in operating the Raman setup, helped me to obtain the temperature distributions, and provided me with hotstage calibration results which I could use to ensure high temperature accuracy. Many of the insights that emerged from our discussions are reflected in this thesis, especially regarding the heater optimization. I am very thankful to him for sharing many of his results that greatly sped up the project. Without his help, this project would not have come as far.

The four of us have managed to push the literature review one step further into a manuscript of which the revision has recently been submitted to the IEEE Journal of Microelectromechanical Systems. Hopefully, it will get accepted.

Furthermore I want to thank Shibabrata Basak for helping me with an actual *in-situ* TEM experiment, Ann Marshall from Stanford University for providing the sample and granting me permission to use the results in my thesis, Nan Zhong for helping me to use his infrared camera, René Henderikx and Martijn Krijnen for training me in using the gas supply system, Mariya Sholkina for training me in doing temperature calibrations, and Ben Bormans, Qiang Xu, Eric Kievit, Sander van Weperen, Marina Zakhozheva, Yevheniy Pivak, Ronald Marx, Diederik Morsink, Merijn Pen, Ton Kerpel, Samuel Korfmacher, Sabine Colen, Mauro Porcu, Jeff Xu and Ryan Ramsay for ensuring a great time at the office and the necessary distractions.

Last but definitely not least, I would like to thank Tessa Driessen for her large contributions to many of the visuals and schematics, for extensively proofreading the thesis (including this sentence), and of course, for her unconditional support and belief in me.

Ronald Spruit
Delft, September 2017

Contents

1 Introduction

1.1. Transmission electron microscopy at high temperature and atmospheric pressure

Transmission electron microscopy (TEM) has enabled imaging with sub-atomic resolution. In the ultra high vacuum environment of the TEM column (~10^{-7}mbar), the electrons are accelerated to voltages of ~200 kV, before transmitting through a sample of typically a single to a few hundred nanometer thick. Upon passing through the sample, the electrons interact with the atoms of the sample and form an image. The image is focused on a fluorescent screen or a CCD camera. Based on the interactions, information such as differences in composition or thickness, crystal structure and chemical identity can be obtained. Therefore, TEM is a commonly used technique in material sciences to study nanoparticles, nanowires, lamellas and 2D materials.

With progressing technology, and continuous improvement of inspection techniques and data handling, new possibilities arose regarding temporal resolution [2]. Where formerly only static information could be obtained in ultra high vacuum and at room temperature, the desire to study dynamics and interactions between materials grew [3]. These processes can be triggered by exposing the sample to different temperatures or gases. However, the triggers that are abundant in real processes had not been available inside the TEM until the last few decades. The development of *in-situ* heating sample carriers started with crucible heating holders [4] and in 2008 Saka *et al.* [5] introduced a battery-powered filament wire heating holder. Although this enabled *in-situ* temperature stimulus of over 1500 °C, it suffered greatly from spatial sample drift (0.1–0.5 nm s^{-1}) due to thermal expansion as a result of its high power consumption. Therefore, it does not allow for studies on dynamic heating and quenching with high magnification. The gas stimulus has been introduced with the environmental TEM (ETEM). This has made it possible to sustain low gas pressures locally around the sample, while maintaining high vacuum in the major part of the TEM column. However, to maintain high resolution, the maximum pressure is limited to ~10 mbar, because of the strong interaction between the electrons and gas molecules [6].

Microelectromechanical systems (MEMS) technology has become a breakthrough for *in-situ* TEM by miniaturizing the heater—Microheaters—with a drastic reduction in thermal mass and power consumption as a result. The impact of these reductions come from greatly improved response time, settling time and the thermal drift. Replacing the traditional copper grids by Microheaters enables *in-situ* thermal studies like heat treatment, annealing, phase transitions and failure analysis in real-time while changing the temperature. To do research in the emerging field of catalysis, only recently, MEMS-based sample carriers have been introduced—Nanoreactors—that allow to simultaneously apply heat and gas stimuli. Nanoreactors enable the *in-situ* study of solid-gas interactions at high temperature and atmospheric gas pressure. Understanding solid-gas interactions at industrially relevant conditions is paramount to develop catalytic nanomaterials for applications in energy conversion and storage, transportation, food production and environmental protection [7].

The Nanoreactor discussed in this project is part of the "Climate" system which consists of: a gas supply system (figure 1.1a) that pre-mixes gases and supply them at various pressures and flow rates, a heating control unit that has the electronics required to attain very high temperature stability, and the MEMS holder (figure 1.1b) that accommodates the Nanoreactor in the tip and provides the interface to the TEM. The gas

supply system and heating control unit are connected to the backside of the holder which contains vacuum throughputs to let gas tubing and electric wires pass towards the Nanoreactor. The tip of the holder has contact needles and vacuum sealing to transfer the stimuli to the Nanoreactor (figure 1.1c).

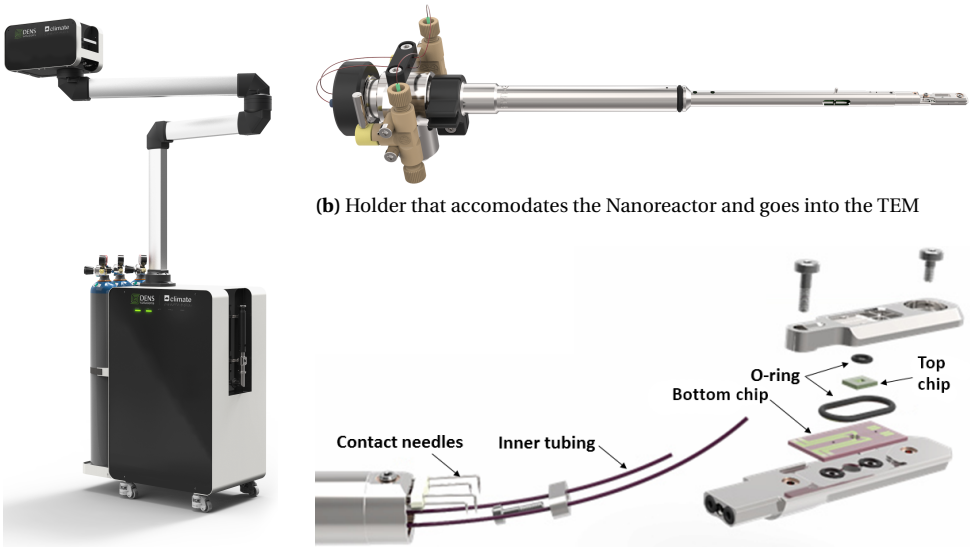

(a) Gas supply system

(b) Holder that accomodates the Nanoreactor and goes into the TEM

(c) Components of the tip of the MEMS holder

Figure 1.1: The "Climate" system which was introduced before by Pérez Garza *et al.* [8, 9]. **(a)** the gas supply system that mixes and supplies gas to the holder. **(b)** The holder to bring the Nanoreactor in the TEM. **(c)** The components of the holder showing the tip of the holder and how the bottom and top chip of the Nanoreactor fit in.

1.2. Problem statement

Although the Nanoreactor enables the observation of solid-gas interactions inside the TEM, depending on the nature of the experiment and the required operating conditions, the thermo-electro-mechanical performance of the Nanoreactor is not sufficient for rapid dynamic studies. During an experiment, stimuli—temperature, gas composition, pressure and flow rate—are varied over time. The stimuli affect the performance of the Nanoreactor and have undefined settling trajectories, which lead to operating inconveniences as well as limited possibilities for science. Reducing the Nanoreactor's sensitivity to stimuli and improving its response time would open up the door to new applications and will help to study fast dynamic processes in more detail and with higher accuracy.

Real-time studies of rapid solid-gas interactions inside the TEM require fast and accurately defined stimuli in order to know exactly under which circumstances the investigated phenomena occur.

The performance parameters that limit the possibilities of the Nanoreactor are:

1. **Membrane deflection**
   As the sample is located on a very thin suspended membrane, the exerted force by the gas, or thermal expansion due to temperature, cause the membrane to deflect. Upon changes in pressure and temperature, the membrane deflection will vary, causing the sample to move out of focus. Next to the fact that having to readjust focus is inconvenient, valuable information of the dynamic processes that happen during readjusting will be lost. In addition, the deflections cause micrometers of variance in gas layer thickness which makes the experimental conditions less well-defined.

2. **Spatial sample drift**
   The need for sample tracking is inherent to TEM experiments. Due to the high magnification, fractions of nanometers of lateral sample movement cause the sample to move out of field of view. Spatial sample drift becomes a lot more pronounced when stimuli are applied; heat losses from the Microheater to the MEMS holder can already cause nanometers of drift due to thermal expansion, the same applies for mechanical forces exerted on the chip by gas flow. Large drift means high magnification cannot be used, which limits the information that can be obtained from the sample.

3. **Temperature homogeneity**
   The applied temperature stimulus has to be accurate, to know the circumstances under which certain phenomena happen to the sample. The sample is typically spread over an area on the Microheater with imperfect temperature homogeneity. As a result, not all particles experience the exact same temperature, meaning that temperature dependent statistics of sample activity cannot be obtained properly.

4. **Temperature stability**
   Extremely high temperature stability has already been achieved in stationary conditions. However, when correlated stimuli are changed, the temperature experiences distortions. For example, when the gas composition is changed, the heater has to compensate for changes in thermal losses. During that time, it is hard to distinguish whether phenomena are caused by the change in gas composition or sudden temperature fluctuations.

5. **Gas flow speed**
   The current configuration allows for gas flow through the Nanoreactor. However, only a small and undetermined portion of the gas actually passes the sample and as a result the local gas flow speed is unknown. Being able to know and control it, can certainly be beneficial to mimic real process conditions more accurately. Additionally, with only a small portion of the gas interacting with the sample, reaction products get diluted by the excess of gas. Improving the gas flow may greatly enhance the detectability of reaction products in, for example, a mass spectrometer.

6. **Gas switching time**
   To study reversible or catalytic solid-gas interactions, it will required to change the gas composition during the experiment (e.g. to study catalyst degradation over many cycles). Ideally the gas composition should change rapidly to the set values, to ensure the condition at which certain phenomena occur. However, a certain gas switching time is required due to the dead volume in the Nanoreactor. This results in a trajectory in which the concentrations of the gases change and settle slowly, and thus a time frame in which the gas composition is not known accurately.

Challenges are still to be faced in further optimization of the Nanoreactor. For this to happen, closer analysis is required regarding its thermo-electro-mechanical behavior. The microscopic scale and the extreme conditions at which these devices must operate, make conventional tools to characterize their behavior unsuitable. The goal of this project is to:

Design an optimized Nanoreactor that enables real-time in-situ TEM studies without interventions, while applying and changing stimuli to the sample.

1.3. Organization of this thesis

Optimizing the Nanoreactor starts with its main component; the Microheater. Since a lot of literature is available on the development of Microheaters—mostly because they have a broader application field than the Nanoreactor—this was the most evident topic to dive into first. Chapter 2 starts with a literature review on Microheaters. The chapter has additional sections that relate closer to the gas and TEM aspects of the Nanoreactor and ends with a section on key takeaways and research questions. At the start of chapter 3, potential solutions are identified based on literature and theory. The chapter continues with the experimental and numerical methods used to determine the performance and specification of the current design and the methods which were used to come to the optimized design. The results of both the characterization and optimization processes are presented in chapter 4, which ends with an optimized design proposal in the last section. Subsequently, in chapter 2.1.4, the performance and specifications of the optimized design are compared to the current design, including a critical reflection on whether the obtained improvement complies with what was aimed for. The contents of appendices A, B, C, D and E concern material property characterization to facilitate reliable modeling, extensive data from experiments and simulations on which the results are based, and error analyses of experiments and simulations, respectively.

2

Literature and theory

2.1. Manuscript: a review on Microheaters

A Review on Development and Optimization of Microheaters for High-Temperature *In-Situ* Studies

Ronald G. Spruit, J. Tijn van Omme, Murali K. Ghatkesar, and H. Hugo Pérez Garza

Manuscript submitted on July 4, 2017. Revision submitted on August 28, 2017, to the IEEE Journal of Microelectromechanical Systems.
R. G. Spruit and M. K. Ghatkesar are with the Department of Precision and Microsystems Engineering, Delft University of Technology, Mekelweg 2, Delft, 2628 CD, The Netherlands (e-mail: Ronald.Spruit@student.tudelft.nl; M.K.Ghatkesar@tudelft.nl).
R. G. Spruit, J. T. van Omme and H. H. Pérez Garza are with DENSsolutions B.V., Informaticalaan 12, Delft, 2628 ZD, The Netherlands (e-mail: Ronald.Spruit@DENSsolutions.com; Tijn.vanOmme@DENSsolutions.com; Hugo.Perez@DENSsolutions.com).

Abstract
MEMS-based sample carriers became a breakthrough for *in-situ* inspection techniques, especially in transmission electron microscopy (TEM) where the sample carrier functions as a micro-sized laboratory and enables dynamic studies on samples such as: nanoparticles, nanowires, lamellas and 2D-materials. Microheaters allow for *in-situ* manipulation of samples by applying heat stimuli such that sample properties and interactions can be studied in real time at elevated temperatures. However, currently developed Microheaters still suffer from undesired effects such as mechanical deflection and limitations in temperature range, accuracy and homogeneity. This review discusses advancements in the technological development of Microheaters. Methods and results found in literature are categorized to provide an overview of optimization methods for thermo-electro-mechanical design aspects. The knowledge from various application fields, including a critical reflection on mesoscopic material properties, is combined into a series of design guidelines. These compose instructions for developing and optimizing Microheater characteristics such as mechanical and thermal stress, temperature accuracy and homogeneity, power consumption, response time and sample drift. Although this review and guide are applicable to many application fields that require a Microheater, emphasis is laid on aspects most relevant to the Microheater as a high-temperature sample carrier for *in-situ* experiments.

Keywords
Electron microscopy, high-temperature, *in-situ*, material properties, microelectromechanical systems (MEMS), microheater, microhotplate, sample carrier, sample manipulation.

2.1.1. Introduction

Microelectromechanical systems (MEMS) technology paved the way for miniaturization of heaters (often referred to as hotplates in other literature). Typical advantages of downscaling are a reduced thermal mass and power consumption, which allow for faster response times, higher temperatures and battery driven technology. Many complementary metal-oxide-semiconductor (CMOS) compatible MEMS heating devices have been designed for various applications with different requirements, each with its own possibilities and limitations. Although the applications vary, Microheater requirements overlap among application fields. Therefore, experience obtained in one Microheater application field can be of use in another. The overall design varies in how the heater is supported and attached to the substrate. Different heater and substrate materials have been investigated, as well as variations in heater geometry and dimensions, usually with the goal to improve certain mechanical and thermal properties. The largest application field is gas sensors, in which the Microheater controls the temperature of a solid with temperature dependent gas reactivity. Bhattacharyya [10] wrote an excellent review paper that focuses on the development of Microheaters with respect to gas sensors. Furthermore, the use of Microheaters is reported for infrared emitters [11], fuel cells [12], thermal atomic force microscopy [13], thermal actuators [14], air bearing controllers [15], convective accelerometers [16], fingerprint sensors [17], *in-situ* synthesis of carbon nanotubes [18], thermal lithography [19], optical filters [20], mass flow meters [21], wind sensors [22], protein traps [23], polymerase chain reaction devices [24], and—the application field this review will focus on mostly—*in-situ* sample manipulation [25].

Formerly, only static information could be obtained from the sample, but with progressing research and continuous improvement of inspection techniques, new possibilities arose and the desire to apply *in-situ* stimuli grew [3]. In real processes the environment is often changing, or is different from the environment in which the sample is inspected (e.g. vacuum). Fully understanding a process, and optimizing it, requires understanding of the dynamic behavior of the sample. MEMS sample carriers enable *in-situ* manipulation and dynamic studies of small samples like nanoparticles, nanowires, lamellas and 2D-materials using all types of microscopy, spectroscopy, thermometry or diffraction. The embedded heater exposes the sample to the heating stimulus, allowing research on material properties and interactions at elevated temperatures (for example, failure analysis, annealing, phase transitions, material growth, or catalysis).

Transmission electron microscopy (TEM) in particular is a commonly used tool in material science, which requires nanoscale samples. Not surprisingly, replacing the traditional copper grid with MEMS sample carriers became a breakthrough in the *in-situ* TEM field. Combining the functionality of a sample carrier and heater into a single device opened many possibilities described in *in-situ* TEM review papers [2, 26–28]. Thorough Microheater optimization research and several *in-situ* TEM sample carriers have been reported in literature [8, 29–32]. However, a review of all the different designs and design considerations with respect to the Microheater as a sample carrier is not yet available.

This review is intended to address Microheater design considerations and challenges in general and specifically for high-temperature and *in-situ* sample manipulation with emphasis on TEM. The review starts with an explanation of Microheater characteristics and how these intertwine through underlying physics and material choices. Next, the state of the art is presented including the undertaken methods and achieved improvements. First, the topic covers mechanical stability, in which material properties, mechanical stress, thermal stress, and spatial sample drift are discussed. Second, temperature and heat are examined with respect to range, lifetime, homogeneity, accuracy, stability, power consumption and response time. Finally, the methods and results are discussed regarding their performance and applicability for high-temperature and *in-situ* experiments. The influential factors are summarized in a table together with design guidelines. This review aims to provide a tool for designers who want to implement a Microheater in their sample carrier or MEMS device in general. Fig. 2.1 is given for the convenience of the reader, to better understand the structure of the article and to have clarity on the function of the different sections.

2.1.2. Characteristics

This section starts with a brief description of the working principle of a Microheater. The main overall MEMS designs and relevant nomenclature will be introduced. Commonly used materials will be discussed with special attention for material properties at the microscale and high temperature. This section ends with a list defining the characteristics and parameters through which Microheater performance is expressed.

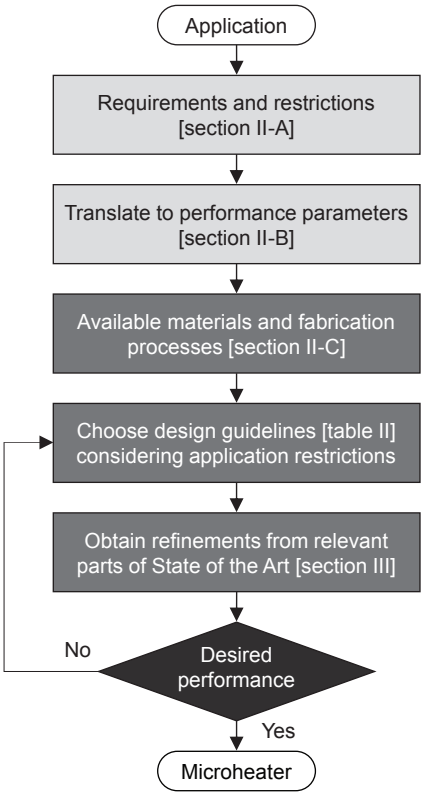

Figure 2.1: Flowchart showing the structure of the article, the function of each of the sections and how they are linked. The first steps in the lighter shade of gray directly depend on the application and are to be fulfilled by the designer. The steps in dark gray concern the Microheater design, which this review elaborates on extensively.

The Microheater

Generally, a Microheater consists of a silicon substrate (or occasionally gallium arsenide [33]) with thermally insulating dielectric thin-film layers on top. The heater itself is an electrically conducting thin-film, which operates through Joule heating—the process in which passing electric current supplied by a voltage or current source produces heat. To improve thermal insulation, the substrate directly underneath the heater is usually removed such that a suspended membrane is formed by the stack of thin-film layers. In the case of transmission-based inspection techniques, transparent windows are embedded in the suspended membranes. The nature of the windows depends on what has to be transmitted. In the case of TEM, the windows can be holes or spots in which the membrane is as thin as a few tens of nanometers to let electrons pass through without scattering them significantly [32, 34]. The overall designs can roughly be split into four types: the Microheater directly on the substrate, on a closed or open suspended membrane, or on a cantilever, illustrated in Fig. 2.2. The closed and open suspended membranes are the most common designs. Reasons to choose one or the other depend on the desired application and specifications, these will be discussed in section 2.1.3.

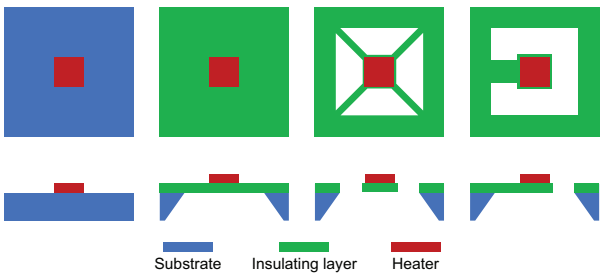

Figure 2.2: Schematics of the top view and cross-section of the four main MEMS designs for Microheaters. The substrate is shown in blue, insulating layer(s) in green and the Microheater area or the region of interest in red. From left to right: directly on substrate [17, 35–37], closed membrane [8, 12, 14, 29–31, 33, 34, 38–61], open membrane [19, 62–74] and cantilever [13, 18, 75–81].

Usually the heater area is the region of interest; this is the functional area of the sample carrier where the sample is placed. Depending on the application, the region of interest is sometimes confined to the center of the heater, for example to have better temperature homogeneity in the functional area. The electrically conducting heating layer can be metal, ceramic or doped polysilicon. Metal requires low voltages and responds very fast due to its low resistivity and high current density. Ceramic has good inertness and therefore allows for usage in harsher environments. Doped polysilicon has the advantage of being easiest to incorporate in standard CMOS processes, because it does not limit the available subsequent steps as is the case with metalization [82].

Metal is the most commonly used heater in literature. First, because it allows for a lot of freedom in geometrical design. Due to its low resistivity, the heater design has a minor effect on the operation requirements; regardless of the design it does not require high voltages to operate. Second, because the linear temperature coefficient of resistance (TCR) allows for accurate temperature (closed-loop feedback) control through resistance measurements, which can be done accurately through a four-point-probe. Third, because its biggest downside—its reactivity to other substances in the environment—can easily be overcome by encapsulation with an inert passivation layer.

Many different metal heater geometries have been explored like S-shaped, circular spirals, curved corners and parallel wires, but most frequently recurring are the double spiral and meander, shown in Fig. 2.3 together with the four-point-probe. In addition, the number of heating lines, width and pitch are varied.

Performance parameters

The characteristics of Microheaters are typically expressed in performance parameters which can be split in two categories. The first category—mechanical robustness and stability—consists of: mechanical stress, thermal stress, stress distribution, and spatial sample drift. The second category—temperature and heat—consists of: range and lifetime, homogeneity, accuracy, stability, power consumption, and response time.

The combination of mechanical stress and thermal stress, and their distribution, determine whether the Microheater is mechanically robust enough to endure large temperature ranges for long lifetimes. The microfabrication procedure is the most influential on mechanical stress and on possible stress concentrations due to lattice defects. For thermal stress, this is the coefficient of thermal expansion (CTE), mismatch of CTE between different membrane layers and local temperature gradient. The distribution is determined by the ability to release stress and, therefore, by the geometrical design and Young's moduli of the stacked layers.

Spatial sample drift determines whether the Microheater will be mechanically stable enough to use it with the desired inspection method. Usually this is only an issue in techniques involving high magnification and relies mostly on mechanical and thermal stabilization of the sample carrier.

The temperature range that can be achieved is largely determined by the materials chosen; by their melting point, temperature dependent stress development, yield strength and electromigration. A higher temperature requires better thermal insulation to keep the power consumption—and thus spatial sample drift—to a minimum. The insulation also plays an important role in temperature homogeneity, which is governed by the mechanisms that determine the spatial in- and outflow of heat.

Accuracy depends on how accurate the TCR is known and the resistance can be measured. Obtaining the TCR is largely a calibration issue and is prone to degradation. So accuracy, and similarly stability, depend

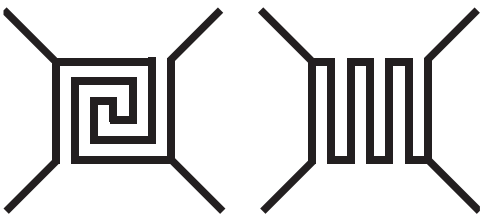

Figure 2.3: Schematics of the common metal heater designs for Microheaters: (left) double spiral [8, 12, 14, 29, 33, 34, 40–49, 51, 56–58, 60, 67] and (right) meander [11, 16–19, 39, 44, 52, 54, 59, 62–64, 66, 68–71, 76, 81, 83–85]. The metal heater designs include the four electrical contacts that make up the four-point-probe: two for supplying the power and two for sensing the resistance change over the wire (see subsubsection 2.1.3).

on temporal constancy of the heater properties. The response time defines the time to acquire the intended temperature. It relates to the power dissipation density, thermal mass and thermal resistance of the Microheater.

Although the characteristics are posed as separate aspects, they are interdependent through the physics, design parameters they depend on. Many of the performance parameters depend on material properties and thus on the materials chosen for the heater and membrane. Therefore, the materials should be well considered as they impose constraints that greatly influence the optimal Microheater design.

Fabrication and material properties
Standard CMOS compatible microfabrication procedures greatly reduce the number of materials that can be selected. As many performance parameters depend on material properties, the cleanroom's constraints (in terms of materials and process steps) directly influence the design and performance. Salient Microheater fabrication steps can be found in [10], or more specific for metal Microheaters in [67, 86] or polysilicon in [83].

Material properties for bulk Material properties of often used Microheater materials are presented in Table 2.1. It lists the bulk material properties at room temperature. This is a useful tool for comparing and picking the right material. However, a few things are important to realize when interpreting bulk material properties. Different academic sources can provide diverse values—even for bulk properties. The reasons relate to the material's purity and processing steps. Next to that, material properties can differ significantly when going to small dimensions (like in thin films) and high temperatures (like Microheaters typically do). Care has to be taken if material properties from literature are used in design and modeling as these cannot be expected to be valid, unless the same composition and fabrication procedure is followed.

Two normally relevant material properties have been left out of the table. These are Poisson's ratio and emissivity. Although Poisson's ratio can be important for bulk mechanics and pressure load cases in thin films [87, 88], it is not meaningful to thin film out-of-plane deflection which is caused by in-plane thermal expansion. Emissivity varies largely with different wavelengths, surface finishes, film thicknesses and temperatures. Therefore, the emissivity value used in modeling and design should not be assumed from literature.

Material properties for thin films As the dimensions of a material go down, surface properties and effects become more dominant. As a result, elastic properties tend to become stiffer as size reduces [105]. More importantly, bulk material properties for thermal conductivity, emissivity and resistivity are not valid anymore for designing and modeling, which will be discussed in more detail in the next paragraphs. Furthermore, the microfabrication procedure has a significant effect on the crystal structure, grain size and density, and thus on the material properties. Because of the process dependency, limited availability of microscale inspection techniques, and the difficulty to measure small scale material properties accurately, they are not always characterized for every new Microheater design or microfabrication procedure. It should be considered that assumptions on material properties may lead to modeling uncertainties.

Since nearly all Microheaters—and MEMS in general—use silicon nitride and silicon oxide as thin-film insulation layers and membranes, these are reasonably well reported in literature. Distinctions are made between stoichiometric Si_3N_4, non-stoichiometric Si_xN_y (also known as silicon-rich or low-stress nitride) and SiO_2. A very tunable property of these layers is the residual stress. For low pressure chemical vapor deposition (LPCVD) silicon nitride, the values can vary from compressive stresses of 90 MPa [106] to tensile stresses of 1300 MPa [107]. With plasma enhanced chemical vapor deposition (PECVD) much higher compressive residual stresses are reported of up to 850 MPa [108]. For silicon oxide, a larger variety of growth and deposition procedures exist. However, the residual stress range is much smaller than for silicon nitride and is typically compressive around 150 MPa [109]. A MEMS Handbook [110] can be consulted for an overview and details on LPCVD and PECVD recipes and materials commonly deposited using these processes.

Other properties which usually cannot be controlled that easily, but are important to take into account for thermal purposes, are thermal conductivity and emissivity. In electrical insulators heat transport is governed by phonons (elementary particles describing lattice vibrations) [111]. Mesoscopic phenomena occur when the thickness of a material layer is in the same order of magnitude as the phonon mean free path (depending on the material, typically a few micrometer) [65]. The scattering of phonons on the layer boundaries becomes

Table 2.1: Material properties for bulk at room temperature. The material properties are obtained from academic textbooks. In some cases books provided a property within a range, if this range was negligibly narrow for a Microheater purpose (i.e. 5 % or less), the average is used. Otherwise, the range is given.

Material	Electrical resistivity Ωm	Temperature coefficient of resistance $10^{-3}K^{-1}$	Melting point °C	Thermal conductivity $Wm^{-1}K^{-1}$	Specific heat $Jkg^{-1}K^{-1}$	Coefficient of thermal expansion $10^{-6}K^{-1}$	Tensile strength[a] MPa	Young's modulus GPa
Heater materials								
Pt	$10.6{\cdot}10^{-8}$ [89]	3.9 [90]	1772 [91]	71.6 [92]	134 [92]	8.9 [92]	145 [93]	171 [93]
Al	$2.65{\cdot}10^{-8}$ [89]	3.9 [90]	660 [91]	237 [92]	922 [92]	24 [92]	45 [93]	62 [93]
Cr	$12.5{\cdot}10^{-8}$ [10]	2.9 [93]	1845 [91]	94 [92]	448 [92]	7 [92]	83 [93]	248 [93]
Au	$2.35{\cdot}10^{-8}$ [89]	3.4 [94]	1063 [91]	318 [92]	130 [92]	14.2 [92]	103 [93]	78 [93]
Mo	$5.2{\cdot}10^{-8}$ [89]	5.1 [93]	2621 [91]	138 [91]	251 [91]	6.5 [93]	450 [93]	325 [93]
Ta	$12.45{\cdot}10^{-8}$ [89]	3.8 [93]	2996 [91]	54 [92]	143 [92]	6.5 [92]	220 [93]	186 [93]
Ti	$54.3{\cdot}10^{-8}$ [95]	3.8 [93]	1680 [91]	21.9 [91]	524 [92]	8.5 [92]	235 [93]	111 [96]
TiN[b]	$2.0{\cdot}10^{-5}$ [97]	1.4 [47]	2950 [47]	30 [98]	599 [99]	7.4 [99]	92 [89]	79–250 [93]
SiC[b]	$1\text{-}2{\cdot}10^{-6}$ [89]	(–3.3) [100]–(–0.5) [59]	2827 [91]	42 [89]	675 [91]	4.6 [89]	186 [89]	302 [89]
Poly-Si[c]	$322{\cdot}10^{-8}$ [10]	(–120)–0.84 [101]	1412 [10]	16–34 [10]	753 [10]	2.8 [10]	1050 [10]	169 [10]
Membrane materials								
Si_3N_4[d]	10^{12}–10^{13} [102]	n/a	1900 [91]–2496 [102]	16 [91]–30 [102]	691 [91]	2.1 [89]–3.6 [102]	690–800 [102]	280–310 [102]
SiO_2[e]	10^{16} [89]	n/a	1610 [91]	1.38 [91]	745 [91]	0.834 [91]	364 [103]	60 [103]
Substrate materials								
Si[c]	10^{-2}–10^{4} [102]	–75 [90]	1412 [91]	145 [102]	712 [91]	2.5 [102]	170 [102]	148 [102]

[a] For ceramics, note that compressive strength is much higher.
[b] As used in nonmetallic heating element materials (some properties differ from standard bulk) [47, 89].
[c] Properties highly depend on type and concentration of doping (or purity). The resistivity and its temperature coefficient are tunable through doping [101, 104].
[d] Polycrystalline.
[e] Mechanical properties are obtained from microspecimens.

significant, resulting in lower thermal conductivity in thin films [112–114]. For silicon nitride, values down to 3 and 1.35 $\mathrm{W\,m^{-1}\,K^{-1}}$ are reported [56, 115], greatly deviating from the 16–30 $\mathrm{W\,m^{-1}\,K^{-1}}$ bulk values reported in Table 2.1.

Emissivity is a dimensionless number between 0 and 1 which states how effectively thermal radiation is emitted from a surface. It only plays a large role in heat transfer at high temperatures because it scales to the fourth power with temperature according to the Stefan–Boltzmann law. Thermal radiation is usually considered a surface property, but actually radiation leaving the surface originates from a small volume just below. If the film is too thin, the bulk emissivity value does not hold [116]. This is what happens in dielectrics; emissivity decreases upon decreasing film thickness due to a loss of source volume. For metals the opposite is true; as the film thickness decreases the emissivity of metals increases because of large contributions from internal reflections. These effects should be taken into account when the film thickness goes below 1 mm for dielectrics or 100 nm for commonly used metals [116].

The last property of interest that can vary greatly with thickness is electrical resistivity. For decreasing thickness, the smaller domain size results in electrons scattering on domain boundaries, giving a higher resistivity [117]. Additionally, a similar phenomenon occurs to electrons as to phonons; the mean free path (typically 10–40 nm [118]) is reduced due to scattering effects on the material layer boundaries. Typically, this effect becomes significant when the thickness of a conductor goes below 200 nm [119]. As an example, Mele *et al.* [29] show that the sheet resistance of a 200 nm thick sputtered molybdenum film is 1.58 $\Omega/\square$, corresponding to a resistivity of $3.16 \cdot 10^{-7}\,\Omega\,\mathrm{m}$, which is over a factor 6 higher than the bulk value given in Table 2.1.

Material properties for high temperature Material properties are temperature dependent. For some material properties, like electrical resistivity, this is usually taken into account in Microheater design. For thermal conductivity and emissivity this is less common.

In conductors, electrical resistivity increases with temperature. This is caused by the increased number of phonons that scatter electrons and reduce their mean free path [120]. This is often referred to as conductors having a positive temperature coefficient of resistance (PTC). The more positive the TCR, the larger the increase of resistance with temperature. Because in thin film materials electrons scatter on boundaries of the small domains, the effect temperature normally has on resistivity is reduced by a factor 2–3 [57, 115]. Therefore, TCR values are typically smaller in thin films [68]. Negative temperature coefficient (NTC) materials, like semiconductors, experience a dominating increase in charge carriers with increasing temperature in addition to PTC phenomena [120].

As explained in the previous subsection, phonons govern thermal conduction in insulators. The temperature dependence varies for different insulators. On the one hand, with increasing temperature more phonons will be present to transfer heat. On the other hand they will start scattering each other. Depending on the temperature and material, one mechanism can be dominant over the other [111]. For conductors there is an additional phenomenon; heat transfer is not dominated by phonons, but by electrons instead. The same situation occurs as just described for electrical resistivity. With a few exceptions, thermal conductivity decreases with increasing temperature [121]. The temperature dependence is relevant for modeling Microheaters, because material properties change significantly over the large operating range [40, 100]. Comprehensive books listing temperature dependent thermal properties are available [91, 98, 99, 122–127].

Emissivity depends on temperature, because optical properties of materials vary with temperature. Wavelengths can have different temperature dependencies [128]. Next to that, in thin films, the temperature dependence of emissivity depends on the structure; it matters if there is a substrate, another layer or stack of layers below the surface layer [129]. The exact behavior is complex and is often not considered by Microheater designers. However, the emissivity becomes crucial when going to high temperatures.

2.1.3. State of the Art

Depending on the foreseen application, designers try to optimize their Microheater for one or a few of the performance parameters listed in the first column of Table 2.2 and 2.3. The methods and results reported in literature are sorted and presented according to the parameter which they thrive to optimize.

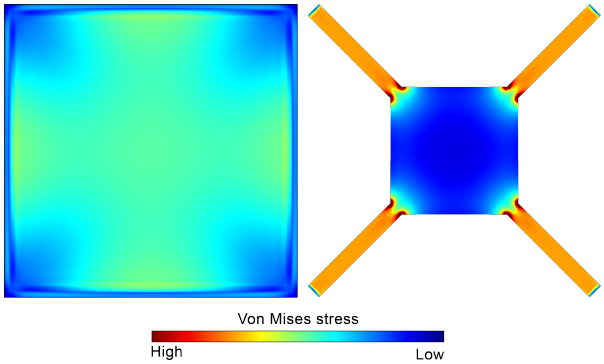

Figure 2.4: Typical stress distributions in thin-film suspended membranes of (left) closed and (right) open designs. Overall, the closed membrane experiences lower stress levels. Important to note are the stress concentrations in the support beams of the open membrane design.

Mechanical robustness and stability
For a robust Microheater, stress levels should not get close to the tensile strength of the membrane. Especially not at room temperature, as robustness here is key for reliable device handling and sample preparation (i.e. drop casting, dry transferring or lamella preparation). Once the sample carrier is in operation it has to be mechanically stable. The sample has to stay in place in order to be inspected properly, especially when using high magnification.

Mechanical stress The mechanical stress present in the Microheater membrane largely depends on the deposition techniques, as described in section 2.1.2. For robustness and fabrication yield, the residual stress should be minimized [61]. In general, this is either done by carefully tuning the microfabrication parameters [59, 67, 104], or by stacking different layers to obtain the desired net stress [29, 51, 54, 55, 83, 130]. Stresses of sequential layers may not be too different to prevent adhesion problems. These occur for example when 270 MPa compressive silicon dioxide and 1200 MPa tensile stoichiometric silicon nitride are put together [131]. Briand *et al.* [115] found non-stoichiometric silicon nitride membranes to perform best in terms of mechanical robustness and fabrication yield. The critical stress level depends on the overall MEMS design. Closed membrane designs are much more robust than open membrane designs. As is illustrated in Fig. 2.4, stress concentrations occur in the support beams, which have a high chance of breaking when a sample is deposited [63]. Residual stress and boundary-layer stresses lead to out-of-plane membrane deflections of up to 1 µm typically. As is the case of Lee *et al.* [55], for a silicon oxide/non-stoichiometric-nitride/oxide closed membrane having a width of 500 µm and a thickness of 1 µm.

Existing alternative designs have their own pros and cons. Cantilevers with the Microheater at the tip are unconstrained and therefore release their residual stress by larger deflections [63]. Lee *et al.* [11] improved robustness relative to silicon nitride membranes through making a free standing Microheater design supported by posts. However, its deformation of 6 µm is relatively large. The best robustness without deflection is achieved when the Microheater is placed on the substrate directly, but this impairs thermal behavior. Porous silicon substrates have been suggested, as the pores greatly reduce the phonon mean free path. This drastically reduces thermal conductivity down to 1–5 $\mathrm{W\,m^{-1}\,K^{-1}}$ while maintaining good mechanical behavior [35, 81]. Polyimide substrates or membranes bring the advantages of increased robustness and flexibility, but lack mechanical stability as they allow for large deformations [43].

Reducing the residual stress to zero is not trivial. The heating and passivation layers also have residual stress and, next to that, the stress can change over time due to high temperature exposure. As compressive stress will cause the suspended membrane to deflect, usually low tensile stress is preferred.

Thermal stress Thermal stress is caused by thermal expansion of the heater and membrane. As one would expect from thermal expansion and Hooke's law, stress increases approximately linear with membrane temperature [67]. Next to thermal expansion of the membrane as a whole, the heater and membrane layers form a composite of different materials with different coefficients of thermal expansion (CTE). Large CTE mismatches cause high stresses to develop at boundary layers which can already cause problems during high-

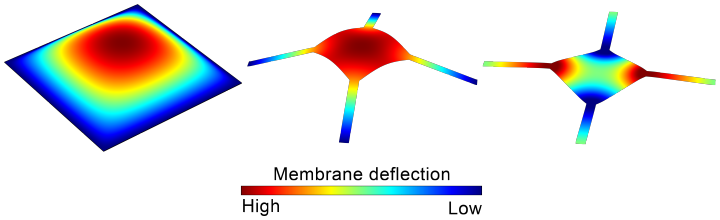

Figure 2.5: Typical membrane deflection patterns for thin-film closed and open suspended membrane designs. The closed membrane typically shows either (left) upward or downward deflection, whereas the open membrane can show (middle) upward or downward deflection, or (right) more complicated patterns.

temperature post-metalization steps in the microfabrication [73]. In operation, a large mismatch results in failure through delamination, if adhesion is not strong enough. Puigcorb *et al.* [60] found that delamination and hillocks are formed to relieve compressive stress of 470 MPa that arises due to the mismatch in CTE between platinum and silicon oxide thin films.

Both thermal expansion itself and the mismatch in CTE cause the membrane to deflect out-of-plane. Where deflections due to mechanical stress are usually confined to about a micrometer, thermal stress causes much higher deflections. This can be a major problem on high magnification inspection techniques as when the sample moves it can go out of focus (for vertical deflections) or move out of the field of view (for lateral deflections). A few commonly encountered deflection patterns are shown in Fig. 2.5. Examples of closed membrane Microheaters show deflections of 15 µm at 622 °C [12] or 10 µm at 450 °C [60]. Open membranes show a larger variety which can be assigned to their more complicated deflection patterns. Simulations of two comparable designs by Prasad *et al.* [67] and Ahmed *et al.* [62] show this difference; the first one shows the more complicated pattern of Fig. 2.5 with a deflection magnitude of only 0.7 µm at 1100 °C, whereas the second deflects up with a magnitude of 5.8 µm at 717 °C. The deflection might as well be downwards, when the layers are stacked in a different order or the stress levels are different [63]. As a way to minimize out-of-plane deflection Hohlfeld *et al.* [20] use rotational symmetry; in this design the region of interest rotates in-plane with increasing thermal expansion.

Just as with mechanical stress, the layer thicknesses and their ratios influence the magnitude of deflection in a way which is not necessarily trivial. Wisitsoraat *et al.* [132] demonstrated that for their design the deflection initially increases when incrementing the nickel-chromium layer thickness up to 500 nm. Upon thicker layers, the deflection starts decreasing again. This can be related to the trade-off between increasing stiffness and increasing the layer that is responsible for the biggest thermal expansion. Contrary to what would be expected from the former case, Ahmed *et al.* [62] showed that varying the membrane thickness over 0.3–3.0 µm at constant temperature does not result in different deflections. In fact the displacement of 5.8 µm remains unchanged, illustrating the complexity of membrane deflections.

In which shape and to what extent the Microheater deflects highly depends on its size, design and layer composition, as these determine how the stress distributes and is released. When optimizing for thermal stresses one should ideally combine materials that show similar and low CTE to minimize boundary-layer and overall compressive stresses. Furthermore, minimizing the heater area minimizes the area that is experiencing thermal expansion and thus the deflections.

Stress distribution When raising the temperature, thermal stress develops in addition to mechanical stress. Depending on how well the stress is distributed over the device, the superposition of these can be a major cause of failure, but can also give opportunities for improvement. Therefore, the stress distribution is something to take into account in the geometry as these determine where the stress originates, how it distributes and how (or if) it releases.

As indicated in Fig. 2.4, closed membrane designs usually have a more homogeneous stress distribution [60] than open membrane designs which experience high stress concentrations in their narrow support beams [63]. However, open membranes do not always fail at lower temperatures than closed membranes [62], presumably, because open membranes are more compliant which allow them to release stress through deflection.

The importance of stress distribution is highlighted by the plastic deformations that Lai *et al.* [54] found for

their closed membrane design. They reported a permanent 450 nm out-of-plane deformation in areas where an additional layer is present (platinum top electrode on silicon oxide/nitride membrane). They attributed this to membrane buckling due to thermal stress and relaxation of mechanical stress. The flexible polyimide membrane design of Briand *et al.* [43] has the advantage that it will not break due to stresses, making it very robust. However, the platinum heating element is not as flexible, causing high stress concentrations in the wires defining their main failure mechanism. The robust free standing Microheater discussed in subsection 2.1.3 actually flattens upon heating and reduces its deflection by 2 µm [11]. This shows that opportunity lays in anticipating on the thermal stress that will occur upon heating. No report was found on deliberate stress compensation though.

Spatial sample drift This parameter is specifically important to sample carrier Microheaters. Most inspection techniques focus on a certain spot in space. If the sample drifts, it might move out of the field of view. This is particularly valid in techniques involving long accumulation times, like Raman spectroscopy and thermometry [78], or high magnification imaging, like atomic resolution TEM [27]. Although some progress has been made on drift correctors for electron microscopes, it is still considered one of the main challenges for *in-situ* electron microscopy, especially when heating [2].

Sample drift originates from two factors. The first one is thermal and mechanical stabilization of the experimental setup as the tiniest temperature changes result in nanometers of drift due to thermal expansion. This can usually be minimized by giving the setup a few minutes to reach equilibrium with its surrounding environment. Creemer *et al.* [45] reported stabilized room temperature drift to be 0.0125 nm s^{-1}. The second factor is more persistent; the drift caused by thermal expansion of the sample carrier substrate and the MEMS holder, originating from heat losses of the heater to the substrate, and from there to the holder [6]. For the design of Belmonte *et al.* [63] the silicon substrate close to the heater experiences an increase in temperature of 20 °C when the Microheater is at 400 °C with a fairly high power consumption of 90 mW. Since generally Microheaters have to go to very high temperatures, proper insulation should be present to minimize the heat losses. This can be done by using thinner and larger membranes made out of materials with a low thermal conductivity. Apart from that, the heater itself can be designed such that it requires less power to reach higher temperatures, for example, by reducing its size. Both insulation and an improved heater design reduce the heat losses to the substrate and thus the required power to heat the sample. Therefore, drift optimization is highly correlated with power consumption (subsection 2.1.3). Lastly, the sample should be placed in the thermal center of the sample carrier to minimize the effect of thermal expansion (as is common practice in the design of optomechanical instruments [133]). The requirement of having a thermal center can be fulfilled by having a symmetrical design, as is the case for open and closed membranes.

Although sample carrier designs often claim to have low drift to properly do *in-situ* experiments, it is not often quantified. Drift rates of 0.1 nm s^{-1} at 500 °C [45] and, more recently, down to 0.025 nm s^{-1} at 650 °C [8] are reported for closed membrane designs.

Temperature and heat
Achieving high temperatures with good accuracy and homogeneity in the region of interest relies on heat transfer mechanisms and their ratios and thus on the geometrical design and the materials chosen. Improving a thermal characteristic can be done through choosing a better material. However, this often comes with trade-offs. Therefore, smart designs have to be invented and optimized using proper thermal modeling and heat transfer analysis.

Range and lifetime The temperature range a Microheater can achieve is determined by the temperature at which it fails or degrades too fast to reach the desired lifetime. This statement is rather broad as for sample carriers the Microheater only has to last for a few *in-situ* experiments of a few hours at most, whereas gas sensors should work for several years [67]. On the other hand, gas sensors do not have to provide and endure temperatures as high as sample carriers; in gas sensors 300–500 °C is usually high enough to activate the desired surface reactions [39, 40, 61], while *in-situ* sample carriers are required to go above 1000 °C for types of experiments especially related to material sciences [2, 134]. Spannhake *et al.* [70] found that lifetime drops rapidly with higher operation temperatures; their platinum heater lasts over 10 years at 500 °C, but only two days at 800 °C.

To reach high temperatures at low power consumption the heated area should be sufficiently thermally insulated from the substrate to minimize power consumption (subsection 2.1.3). If not, the substrate heats up, causing drift (subsection 2.1.3). The maximum temperature is always limited to that at which the temperature dependent yield stress meets the rising thermal stress at which hillocks, delamination or even cracks occur [60]. At temperatures below that, diffusion and creep can become significant to slowly destroy the Microheater. For bulk, the critical point is roughly at two-thirds of the melting temperature of the chosen materials [102]. In addition, materials with high melting temperatures that do not go through phase transitions (changes in crystal structure) should be chosen, as that will abruptly change material properties.

Typical high-temperature failure modes with a non-mechanical nature are related to current density. High current density intensifies heater degradation through electromigration [70], which is the gradual movement of conductor ions due to electrons scattering on them. A way to minimize this is either by choosing a material in which electromigration is less predominant, or by using a discontinuous heating mode [33]. Sharp corners in the heater geometry cause local current density peaks of two to three times the mean value, as can be observed from simulations by Sidek *et al.* [69]. These places experience more Joule heating resulting in local hotspots, with much faster degradation as a consequence [70]. In addition, the heater material can amplify or attenuate the effect of hotspots depending on its TCR value [50]. In PTC materials the resistivity increases with temperature. Since power dissipation scales with resistivity, hotspots get even hotter. Therefore, the combination of sharp corners, narrow heating wires and large positive TCR values should be avoided such that current crowding and hotspots will not occur.

The highest temperatures (1000–1500 °C) are reported for closed membranes with metal heaters [8, 29, 30, 54], which indicates that mechanical robustness and stability are the most important requirements to meet. Few occurrences of deviating Microheater designs reach over 1000 °C: a ceramic heater [38], an open membrane [70], a free standing metal heater [11] and a doped silicon cantilever [76].

Homogeneity Homogeneity is the uniformity of temperature over the region of interest. However, what the region of interest is, varies amongst application fields. For example, for gas sensors, the region of interest is the area which senses the presence of gases. For sample carriers it depends on the sample location and spread. Only few types of samples, like lamellas, allow accurate placing [135]. Samples are usually spread over a large portion of the sample carrier when they are deposited through dropcasting [25], dry dispersion [136] or sputtering [137]. To be able to inspect as many of the samples as possible, the larger the homogeneous area the better. The size of the homogeneous area depends on the heat transfer mechanisms involved (subsection 2.1.3). Important factors are the spatial heat generation, loss and transport in the Microheater, and therefore, the heater size and design.

A lot of research has been done on the shape of the metal heater wire [10]. The designs most commonly used are the double spiral and meander (Fig. 2.3). The double spiral shows the best performance regarding homogeneity [40]. Likely because of how the metal wires—whose thermal conductivity is much higher than that of the membrane—spreads the heat. The metal in the double spiral guides the heat outwards, spiraling from the hottest area in the center, whereas the meander facilitates heat conduction to the sides, along the heating lines. Fig. 2.6 illustrates the effect on the homogeneous region. Lee *et al.* [55] exploited this feature by connecting a platinum heat spreading structure to its Microheater. From simulations it becomes clear that homogeneity can be further improved by combining a parallel heater with a spiral or meander heater to compensate for areas with lower temperature [69]. Hwang *et al.* [53] produced individually optimized parallel polysilicon heaters reaching 90 % homogeneity in a relatively large area. Another promising design choice is the use of gradually varying heater linewidth, with the largest linewidth in the center and smallest at the edges to generate minimal and maximal heat dissipation, respectively. For the double spiral, this improved homogeneity from 83 to 96 % [56]. Alternatively, the same result can be achieved by varying the pitch between heater lines [40].

Next to optimizing the heater design, a heat spreading layer can be incorporated to enhance homogeneity in the region of interest. Briand *et al.* [44, 115] left a 10 µm thin silicon island just underneath the heater by etch timing. Due to the high thermal conductivity of silicon, the heat spreads over the region of interest, reaching 99 % homogeneity. The downside is that these Microheaters were found to be more brittle and have higher thermal mass (see subsection 2.1.3) than conventional open and closed membranes [83]. As an alternative, Ahmed *et al.* [62] managed to improve homogeneity from 98 to 99.5 % by depositing a 200 nm thick layer of

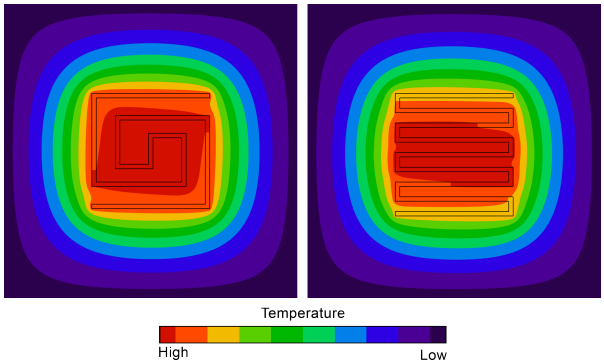

Figure 2.6: Typical isothermal contours plots of (left) double spiral and (right) meander Microheater designs on thin-film suspended membranes. Even though the spatial heat dissipations are comparable, the isotherms have different shapes within the heater area; the double spiral has a much more circular homogeneous area than the meander design, indicated by the orange and red regions.

silicon carbide in the region of interest. Cantilever designs are able to achieve homogeneity values of 96–98 % without using complicated strategies [80]. Its advantage is that heat losses through conduction only happen in one direction, resulting in a gentle temperature gradient. As a result, the tip of the cantilever becomes a relatively large homogeneous area.

In high-temperature sample carriers, the best performances are obtained by expanding the metal heater wire locally to use it as a heat spreader structure reaching 99 % homogeneity at 1000 °C [30], or by confining the region of interest to within the homogeneous area with the double spiral design reaching 98.5 % homogeneity at 1250 °C [8].

Accuracy At first sight, accuracy may seem a control issue mostly. However, the proximity between the intended and actual temperature in the homogeneous area gets impaired by the TCR, limitations coming from the microscale calibration and material degradation over time.

In order to measure and control temperature, many Microheaters are equipped with a built-in thermocouple [104] or a four-point-probe [40] (as shown in Fig. 2.3). Using the TCR of the Microheater, the four-point-probe is able to monitor resistance variations over the heater wire. A larger TCR allows for more accurate temperature measurements, because of higher sensitivity to temperature changes [104]. However, due to thermal gradients in the Microheater, the measured resistance change is an average. Therefore, the material TCR—which can easily be obtained by calibrations on bulky hotplates [46] or ovens [67]—cannot simply be used. The four-point-probe on itself is a very accurate temperature controlling feature, but calibration is required [40].

Calibration can be done using various thermometry methods; no adequate method to map temperature on the microscale has been found yet [40]. Because of the Microheater's small thermal mass, ideally non-contact methods are used to prevent interference of probes [41, 42]. Temperature measurement methods with high accuracy and sufficient spatial resolution are Raman thermometry [138], electron energy loss spectroscopy (EELS) [84], parallel beam electron diffraction (PBED) [137] and reference materials with a very well known transition temperature [29]. Unfortunately, not all of these technologies are available in every lab or with the required accuracy, and they can be rather time consuming. That limits their use to characterizing sample carriers during the development phase, and makes them very impractical for accurate calibration of large numbers of individual Microheaters that are to be used in subsequent *in-situ* experiments. Therefore, calibration of Microheaters usually relies on optical methods with all their consequences. Often used tools are infrared cameras or pyrometers. Errors are introduced due to wavelength, film thickness and temperature dependence of emissivity [139] (subsection 2.1.2 and 2.1.2). Infrared images by Lee *et al.* [11] demonstrate that reflections of other surfaces can impair the results such that surroundings of the objects can appear hotter than the heater itself. These type of effects can be minimized by covering the heater with a thin layer of black paint to approach a black body [29] and accuracy can be improved by fitting the Planck distribution [104] and modeling sources of error [74]. Wiche *et al.* [72] provides a quantitative comparison of methods using TCR, infrared camera, thermocouple probe and melting crayons. They bump into the same issues as discussed before, resulting in temperature accuracy errors up to 25 % for temperatures over a 20–900 °C range, illustrat-

ing the need for calibration of these methods before they can be considered reliable. In high-temperature sample carriers produced in larger numbers, the TCR is calibrated using pyrometry [31], using a heated oven achieving 96 % accuracy [30] and using pyrometry correlated to Raman achieving 99 % accuracy [8].

Once calibrated, the heater properties have to remain constant. Degradation will reduce the accuracy of the calibration over time. Mele *et al.* [29] analysed the change in temperature reading when operating platinum and molybdenum Microheaters at high temperatures for multiple hours. After only 3 hours of usage at 600 °C platinum and molybdenum had 1 % and ~0 % error, respectively. The molybdenum was pushed further to 1000 °C at which the error became 6 % after 3 hours. Degradation can be minimized by annealing the Microheaters prior to calibration. Alternatively, if the degradation is reproducible, it can be anticipated on; corrections can be implemented in the control software to make the temperature error smaller.

Stability Temperature stability is greatly depending on degradation of the heater, as described in subsection 2.1.3. If somehow the resistivity or the TCR of the heater changes, this changes the power dissipation and thus the temperature. A way to solve this problem is by keeping the power input constant instead of either voltage or current. However, this method will not work in a changing environment in which heat losses are different. Due to the nature of the experiment, it may be in vacuum (e.g. TEM/SEM), at low gas pressures (e.g. environmetal TEM/SEM) or in ambient air (e.g. optical microscope). The way to solve for all cases is to provide feedback to constantly correct for changes, which is what the four-point-probe allows for [40].

A different approach is to prevent the degradation to happen, by choosing materials that endure high temperatures better. Spannhake *et al.* [71] propose semiconductor heater elements. However, these materials introduce other issues and have much higher resistivity, which means they require about 100 V to operate, while metal heaters suffice with a few volts. The other issue is that nonlinearity of the TCR—as is typically the case for ceramic or semiconductor heaters [77]—hampers the ease of control and thus the temperature stability. A large difference can be made by choosing a proper material with a linear TCR value within the operating range [104], or by increasing doping concentrations to obtain a more linear TCR [64].

Power consumption For many Microheater applications it is necessary to have a device with small heat losses to its surroundings to obtain low power consumption. In integrated circuits this is important to avoid heat cross-talk with other devices, to avoid heating of electronic components and to enable battery powered portable devices (like portable gas sensors) [63]. More specific to sample carriers, the main reason for minimizing power consumption is its direct connection to sample drift through thermal expansion (subsection 2.1.3).

The power consumption of the Microheater fully depends on the heat loss mechanisms and, therefore, on how well the Microheater is thermally insulated [61]. These heat loss mechanisms (illustrated in Fig. 2.7) are: conduction through membrane, conduction through the electric contacts, conduction through air, convection through air and emission of thermal radiation. In literature, many efforts have been made on analytical models to understand and predict the thermal behavior of the Microheater. Despite the importance, as pointed out by Samaeifar *et al.* [68], thermal models and heat transfer analyses throughout literature lack consistency and completeness in terms of which assumptions are made and which heat loss mechanisms are included.

Conduction through membrane is one of the major heat loss mechanisms which is significant for all temperatures as it scales linearly with the temperature gradient. Since this is quite straightforward to model, little ambiguity is found in the models, but large variety is found in the thermal conductivity values of silicon nitride as pointed out before in section 2.1.2. Attempts have been made to determine thermal conductivity values using AC heating in which the phase shift between applying heat and sensing heat provides information on the thermal diffusivity [139]. However, to obtain thermal conductivity therefrom, the heat capacity has to be known, which shifts the problem to determining heat capacity. Contrary to the membrane, heat losses through the electric contacts are usually not considered, but are not negligible considering their much higher thermal conductivity. As to be expected, open membranes provide better thermal insulation than closed membranes as there is less matter to conduct heat through [68]. Typical approaches taken to decrease heat losses are increasing the size of the membrane [115] and reducing the size of the heater [61]. Cantilever designs excel in this aspect, since the matter to conduct heat through is even less [81]. Alternative designs exist in which no membrane is used at all; the heater is made on a porous silicon foundation resulting in

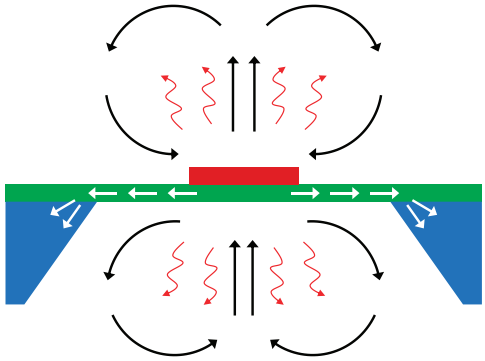

Figure 2.7: Cross-sectional schematic of the heat loss mechanisms in a Microheater. The substrate is shown in blue, insulating layer(s) in green and the Microheater area or the region of interest in dark red. Conduction through the membrane and electric contacts is indicated by white arrows, conduction and convection through air by black arrows and emission of thermal radiation by curly red arrows.

increased robustness, but at the cost of a more complicated microfabrication procedure. The thermal conductivity of porous silicon is so low ($\sim 1\,\mathrm{W\,m^{-1}\,K^{-1}}$) that the power consumption can become comparable to membrane designs [35].

Where some authors assume that convection is negligible compared to conduction in air on the microscale [33], some assign large part of the heat loss to convection [29]. Not to choose one above the other, at least experiments show that the combination of the two is responsible for a very large portion, that is two-thirds, of the total power consumption [130]. However, these are not relevant for sample carriers meant for inspection techniques in vacuum.

Heat losses due to emission of thermal radiation are correctly neglected in much of the literature, as many of the Microheaters do not reach temperatures high enough to make it significant. However, the influence of radiation heat losses increases with temperature to the fourth power and should not be neglected when a significant portion of the Microheater reaches above 500 °C [71, 130].

The better performing Microheaters typically show total power consumption values of 10–65 mW in vacuum or 100–250 mW in air at 1000 °C [8, 11, 29–31].

Response time One of the strengths of MEMS Microheaters is the fast response time. The time it takes to reach the intended temperature improves with higher current densities and lower thermal mass [8]. This results in the general trend that smaller Microheaters have faster responses [140]. Depending on the purpose of the Microheater, this allows for pulsed operation instead of continuous, greatly improving lifetime and energy usage [104]. From a sample carrier perspective fast response time allows for new types of material research, for example by doing reliability experiments with temperature cycling or by much better crystallization of samples [36].

Typical open-loop time responses are around 10 ms for open and closed membrane designs [63]. Zhou *et al.* [104] reduced the size of their Microheater to optimize for power consumption and response time, resulting in time constants in the range of 33–76 µs to reach 300 °C with only 2.5 mW power consumption. Samaeifar *et al.* [68] did the same thing for the more regular open membrane design, achieving time constants of a few milliseconds.

2.1.4. Discussion

The overview aims to provide a comprehensive report on the methods that have been explored and the results that have been obtained in the process of optimizing Microheaters. However, in the studied literature, optimizations were always done with a larger goal in mind; improving the performance of the device, which could for example be sensitivity in gas sensors, thermal radiation emission in IR emitters or selectivity in protein traps. Such an overall goal usually imposes certain constraints on the design, which prevents the designer from exploring options that could be interesting for other applications. The same applies to sample carriers, especially when these should operate in a TEM. In this specific case, the sample carrier design can

be optimized to perform in vacuum, which influences the design process as heat loss through convection is not present. This means it requires less power and thus less current, making related failure mechanisms as electromigration of less concern. Moreover, the modeling of heat losses through convection, on which little consistency is found in literature, is not required. However, if the Microheater is to be used in an ETEM, or should be compatible with both TEM and ETEM, extra attention should be given to temperature accuracy, stability and inertness (see subsection 2.1.2). The presence of a gas creates additional heat losses that affect the temperature distribution. To account for that, the thermocouple or the four-point-probe connections should be as close to the center of the membrane as possible, such that the temperature accuracy is not affected by the slightly varying temperature gradient over the membrane.

Not all of the four sample carrier designs from Fig. 2.2 are equally beneficial for transmission based studies. For TEM, electron transparent windows must be included. In the design with the heater directly on the substrate, holes will have to be drilled through the substrate to allow the electron to pass, whereas in the other designs the thin membrane (especially if very thin windows are included) would already allow imaging. The mechanical stability at elevated temperatures is the most important characteristic to microscopists. Large sample drift will defeat the purpose of the Microheater, as in the end, the study of the sample dynamics over time has to be enabled. This directly imposes constraints to the design; the power consumption has to be minimized, eliminating the concept of placing the heater directly on the substrates. Even the relatively well performing porous silicon substrates will not meet the requirement. As mentioned before in subsubsection 2.1.3 the sample should be placed in the thermal center of the sample carrier. This means non-symmetrical designs, like cantilevers, are no option due to the absence of a thermal center, even though they have the prospect of best performance in terms of power consumption.

This leaves open and closed membranes to be discussed. As mentioned in subsubsection 2.1.3, currently the highest temperatures are achieved for closed membrane designs due to their superior mechanical robustness. However, exploring extreme temperatures of over 1000 °C is not necessarily always interesting and open membranes have the potential to perform better regarding sample drift and homogeneity because of their lower power consumption and superior thermal isolation. Still, no open membrane sample carrier has been proposed for *in-situ* TEM experiments. The robustness plays a role here, as the weaker open membrane has an increased chance of getting damaged when samples are deposited. One common sample deposition method, drop casting, will suffer from the additional topography the open membrane brings. Upon evaporation of the liquid, capillary forces will attract the liquid—and thus the dissolved sample—away from the electron transparent windows. This effect will be relatively large in open membrane designs where the holes even allow the sample to flow to the other side of the membrane. Overall, the sample compatibility of a closed membrane is better, making it the most suitable design currently available in literature.

A more general issue is the proper thermal contact between the sample and Microheater [137]. Especially at the nanoscale, adhesion between the specimen and the surface area of the sample carrier depends heavily on the surface energy and thus the roughness of material. Therefore, it is important that the Microheater's surface is clean and as (atomically) smooth as possible in order to promote sample-to-surface adhesion. This should always be considered as a potential source of error in effective temperature accuracy, especially when the sample is a poor thermal conductor, or at high temperatures if the sample dissipates a lot of heat through thermal radiation. If the sample is a large emitter (large particle size and emissivity of 1), the potential temperature error could be estimated from a power balance; the inflow is governed by thermal conduction through the window and the emission is governed by thermal radiation. Equating Fourier's law and the Stefan-Boltzmann law using silicon nitride material properties for particles of 1 µm in diameter will result in an estimated temperature error of 1 % at ~1500 °C. The error will be smaller when the particle is smaller or the temperature is lower, indicating that this effect should be considered in these limiting cases.

A TEM-related concern could come from magnetic fields caused by current in the metal wire. Although the magnetic field of the TEM lenses will typically be orders of magnitude higher than the one caused by the Microheater, still it can be worth to put it to a minimum. The interference of the magnetic field with the lenses may otherwise reduce the achievable resolution. According to Maxwell's equations of electrodynamics, this means making the current loop as small as possible and using superposition of opposing magnetic fields, to minimize magnetic fields as a result of time-varying and constant current respectively. The double winded spiral is the most suitable design to meet both requirements [45].

The final design will largely depend on the materials chosen in the early stage of the design. Therefore, it is important to make a well-considered choice on the materials to use, which is the reason why attention is

Table 2.2: Design guidelines to develop and optimize Microheaters regarding mechanical robustness and stability. For each performance parameter, the set of influential factors result in a set of design guidelines. Influential factors have multiple design guidelines or share them due to the physics they depend on.

Mechanical robustness and stability		
Performance parameter	**Influential factors**	**Design guidelines**
Mechanical stress (2.1.3)	• Residual stress • Boundary-layer stress • Flexibility (Young's modulus) and stability • Membrane stiffness	• Reducing combined stress level of stack. • Annealing the stack of layers. • Slight tensile stress (for suspended membrane) • Tune thickness-size ratio to obtain desired stiffness
Thermal stress (2.1.3)	• Magnitude of the CTE • CTE mismatch between different layers • Thermal expansion in hot area • Geometrical heater design • Membrane stiffness	• Use materials with low CTE values • Stack layers with similar CTE values • Minimize the hot area; reduce heater size • Avoid sharp corners • Tune thickness-size ratio to obtain desired stiffness
Stress distribution (2.1.3)	• Superposition of thermo-mechanical stress • Geometrical constraints on deflection • Microheater geometry • Membrane geometry type	• Use deliberate stress compensation • Geometry that allow for stress release (e.g. rotational symmetry) • Avoid sharp geometrical transitions between layers • Use closed membranes for a more homogeneous stress distribution
Spatial sample drift (2.1.3)	• Thermal and mechanical stabilization • Thermal expansion of the substrate, due to heat losses from the Microheater • Thermal expansion of the holder, due to heat conduction from the substrate	• The sample region should be the thermal center of the Microheater • Insulate the substrate from the heater by making membranes thinner and larger, and use materials with low thermal conductivity • Use low thermal conductivity membrane materials • Reduce heater size such that it requires less power

given to material properties in section 2.1.2. The designer will typically consider which materials are available in the cleanroom prior to determining which ones allow for going to the desired temperature. If the cleanroom's repertoire leaves multiple options, the pros and cons should be considered based on the material properties. Ideally, one would select the material with minimal CTE and TCR to prevent high thermal stresses and minimize risks with delamination and hotspots. Although low TCR is better for the mechanical purposes, it comes with a trade-off: on the one hand a large TCR causes hotspots, limiting temperature range and lifetime, but on the other hand a large TCR provides easier temperature control and thus higher temperature accuracy and stability. A small CTE minimizes thermal stress and thus membrane deflections. Deliberate stress (pre)compensation (subsubsection 2.1.3) seems promising, but requires more extensive research with regards to its implementation in Microheaters. Opportunity is left in the optimization of membrane deflection as plenty of observations have been done on the subject, but little effort has been made to actually optimize for it.

Deciding between a metal or ceramic heater might depend on the application in mind. However, it is important to highlight that metal has a higher current density and therefore allows for extremely fast and linear responses. The combination of a metal heater with a four-point-probe—meaning very fast responses and measurements of resistance—allows for fast closed-loop feedback control to keep the temperature stable upon changing environments. This is especially relevant when the Microheater is used in combination with, for example, different gases and pressures in an environmental TEM. Feedback will also keep temperature discrepancies to a minimum when the heater is used with both vacuum and ambient inspection techniques. The main advantage of the ceramic heater is that it has a higher inertness. Therefore, it does not necessarily require an additional dielectric layer, but instead the sample can be placed directly on top of the heater. In

Table 2.3: Design guidelines to develop and optimize Microheaters regarding temperature and heat. For each performance parameter, the set of influential factors result in a set of design guidelines. Influential factors have multiple design guidelines or share them due to the physics they depend on.

Temperature and heat		
Performance parameter	**Influential factors**	**Design guidelines**
Range and lifetime (2.1.3)	• Melting temperature of membrane and heater materials • Diffusion and creep rates • Morphological and crystal structure changes • Current density • TCR of heater material	• Choose materials with high melting temperature • Design heater such that current crowding is unlikely to happen; avoid sharp corners • Choose material in which electromigration is less predominant • Use a discontinuous heating mode • Choose materials with small and negative TCR to avoid amplification of hotspots
Homogeneity (2.1.3)	• Spatial distribution of power dissipation • Heater size • Heater design • Thermal conductivity of different membrane layers	• Use gradually varying heater linewidth • Use varying heater pitch • Use a meander or double spiral design • Design a heat spreading structure • Confine the region of interest to within the homogeneous area
Accuracy (2.1.3)	• Microscale calibration limitations • Errors introduced during calibrations • Heater degradation over time • Value of the TCR • Temperature control	• Calibration using varying thermometry methods • Use non-contact methods to prevent interference • Anneal at high temperature prior to calibration • Use high-TCR materials to increase sensitivity to temperature • Use an integrated thermocouple or four-point-probe in closed-loop
Stability (2.1.3)	• Heater degradation over time • Consistency of power dissipation • Change of surroundings • Temperature control	• Keep the power input constant when desired temperature is obtained • Closed-loop feedback control • Include a thermocouple or four-point-probe close to center • Choose material with linear TCR
Power consumption (2.1.3)	• Heat loss mechanisms; conduction, convection and radiation • Temperature dependent material properties • Explored temperature range	• Use low thermal conductivity membrane materials • Reduce size of the heater • Account for heat loss mechanism changes as function of temperature • Make the membrane larger and thinner
Response time (2.1.3)	• Current density • Thermal mass and resistance	• Use heater materials that allow for high current density • Decrease thermal mass and thermal resistance in heater area

that case, care has to be taken that direct contact between the heater and the sample can allow current to pass through the sample causing local Joule heating (especially if the resistivity of the sample is comparable or lower than that of the ceramic heater). From a design point of view, the metal heater allows for larger flexibility (because the metal has a lower resistivity): the heating wire can be patterned in all sorts of shapes and with varying linewidth and pitch, giving a lot of design freedom over the spatial power dissipation. This allows metal heaters to dissipate more heat locally where it is desired, which potentially minimizes heat losses to the substrate and therefore minimizes drift. Furthermore, it allows for optimization of the temperature distribution resulting in better homogeneity. Such flexibility is much less for ceramic heaters which require a wide heater to flow the same current. In this way, an optimized metal heater can perform much better in terms of temperature homogeneity.

It has become clear that many aspects should be taken into account in the design of a Microheater. Changing the design to improve for a certain parameter can have a large impact on another. To provide the reader with a

tool to keep the overview of the major things to take into account, Table 2.2 and 2.3 provide design guidelines based on the most successful methods from literature. They summarize what has been learnt from the state of the art and the discussion. Details on the influential factors and design guidelines are given in the corresponding parts of section 2.1.3. Keep in mind that, depending on the application, not every single guideline will always apply to every design. As the performance parameters are interdependent, it is impossible to provide a fixed set of guidelines. The application determines which performance parameters are most relevant. The table gives an overview of the potential solutions and design guidelines, which compatibility should be verified with the application. In the subsequent optimization steps, the interdependence of the influential factors should be carefully considered to refine the design.

The so far discussed optimizations are all attainable, or likely to become so, within an overseeable amount of time. Looking into the future, it can be observed that recent advancements have been made in producing reduced graphene oxide (rGO) Microheaters. Yao *et al.* [141] showed extraordinary high-temperature performance with their rGO Microheater; the sustainable carbon material is able to endure temperatures up to 2700 °C. The power consumption of these type of Microheaters are currently in the single watt regime, too high for sample carrier purposes. In addition, feature sizes are still too big as well. High-temperature rGO heaters are produced using 3D printing, resulting in feature sizes of ~200 µm. However, other methods are being explored. Sinar *et al.* [142] used laser microfabrication to locally reduce non-electrically conducting graphene oxide (GO) into conducting rGO with dimensions in the order of 2–3 µm. More methods should be possible as GO has been micropatterned with feature sizes in the 2–50 µm range for biological purposes before [143]. Eventually, when the research community succeeds in shrinking these type of Microheaters down further and if there is demand for exploring these high temperatures, these types of materials might take over because of their superior temperature performance.

2.1.5. Conclusion

Microheaters are broadly used in MEMS. The research field was originally dominated by Microheater development for gas sensors that typically use metal heater materials. However, the use has extended to different fields with numerous applications and therefore many different designs. This review considered Microheaters of all types. An overview of the existing design approaches and optimization methods was presented. The state of the art was categorized in the defined Microheater characteristics through which their performance is typically expressed. This review combined acquired knowledge from various application fields, which resulted in a guide with Microheater design guidelines. Although this review and the guide are applicable to many application fields that require design and development of a Microheater, emphasis is laid on design parameters most relevant to the Microheater as a high-temperature sample carrier for *in-situ* experiments.

Closed membrane designs are most practiced for sample carrier purposes, both with ceramic and metal heaters. The reason is that these perform best with regards to robustness and mechanical stability and, therefore, have a higher fabrication yield and allow harsher sample preparation methods. Currently, ceramic and metal heaters show comparable performance, but the prospects for metal heaters look more promising as they allow for larger freedom in the design and thus for more ways to improve. The majority of research and development has been focused on metal Microheaters through which significant improvements were made for, typically, one or two of the many characteristics. The remaining task is for the research community to develop an optimized Microheater that combines the previously and separately attained improvements. This review aimed at providing the means to achieve an optimal Microheater with the desired specifications. Table 2.1 helps to choose the right heater and membrane materials and Table 2.2 and 2.3 guide and help decide on the design choices.

2.2. The Nanoreactor

2.2.1. Introduction

Before the introduction of the Nanoreactor, two existing methods enabled the confinement of gas inside the TEM. Those are the earlier mentioned ETEM, attained through differential pumps, and the windowed gas cell, in which the gas is prevented to enter the TEM column by an electron transparent amorphous carbon film of ~10 nm thick. In both cases the maximum achievable gas pressure is ~10 mbar. As described by Giorgio

et al. [144], both have their pros and cons. The resolution was found to be slightly better in the ETEM case (0.14–0.18 nm compared to 0.21 nm). However, this was not limited directly by the cell itself, but rather by the large gap pole piece that is required to fit the cell in. In fact, the cell concept can potentially allow for higher resolutions as the thickness of the gas layer is only 1 mm, whereas this is typically 10 mm in the column of an ETEM [6]. Advantages of the cell are its (potential) compatibility with a large portion of TEM's out in the field, as only the holder has to be adjusted to make it fit in between the pole pieces. Moreover, due to the small gas volume of the cell, the outgoing gas can be analyzed by mass spectrometry, potentially allowing to measure reaction products of the processes visualized using the TEM [144]. A disadvantage is the need for electron transparent materials to serve as windows. In this case amorphous carbon has been used, which is prone to oxidation when used in combination with gases containing oxygen. Therefore, this configuration does not enable the study of redox reactions. Alternatively, more inert materials are suggested such as silicon nitride [145].

The development of the Nanoreactor commenced at the Delft University of Technology in 2001 [6], where it emerged from progressing research on *in-situ* TEM Microheater technology and the desire to enable atomic-resolution studies on chemical processes at gas-solid interfaces at high pressure. To the author's best knowledge, the earliest reports on the Delft Nanoreactor date back to 2008, when Creemer *et al.* [49] introduced it. The principles behind the design of the Nanoreactor come close to those of the windowed gas cell with major improvements on further reducing the thickness to a few tens of micrometers. The advantage comes in two ways: the same resolution can be obtained with a much higher gas pressure, and the large gap pole piece requirement drops, allowing to use better pole pieces resulting in a higher resolution than what could be obtained with the ETEM or windowed gas cell.

The reduced gas layer thickness has been made possible by MEMS technology. The first published design of Creemer *et al.* [45, 48, 49] consists of two facing MEMS devices that are aligned and glued together to form a closed cell. The bottom chip consists of a silicon substrate covered with a 1.2 µm thin silicon nitride film that has an embedded platinum double spiral Microheater, similar to those described in section 2.1. The substrate material underneath the Microheater has been etched away to release a suspended membrane of 1 mm^2. To facilitate the transmission of electrons, the central part of the suspended membrane contains a number of ellipsoidal electron transparent windows as thin as 10 nm. The top chip has a simpler design, including just the suspended membrane and electron transparent windows. To enable gas flow, the bottom chip has a gas inlet and outlet and one of the membranes has disc-shaped spacers that make up a 4 µm thick gas channel from inlet to Microheater to outlet. To bring it into the TEM, the MEMS device is mounted in a custom TEM holder that has gas lines as well as four electrical probe needles to connect both the gas channel and the Microheater. In this configuration a resolution better than 0.18 nm was obtained in a 1.2 bar hydrogen environment at 500 °C. In comparison, even with a gas pressure that is 100 times higher, a similar resolution was obtained as with the ETEM and windowed gas cell.

In the years after, a few different paths were explored, but the overall Microheater and gas chamber design stayed roughly the same. The different paths mostly concerned: different fabrication methods, designs and assembly methods, to prevent carbon contamination, to improve ease of use, and to improve fabrication yield. According to Erdamar *et al.* [6] those paths were:

- testing different types of glue, both organic and inorganic, as the carbon contamination was caused by outgassing of the epoxy used in the initial design. However, with the organic ones, no glue was found that resolved the issue completely, and with the inorganic ones, achieving airtightness has been challenging. Eventually, the problem was not solved with the chip. Instead, the holder was modified such that gas leaking through the glue would not end up in the TEM column.
- using a Viton O-ring in between the bottom and top chip instead of gluing them together. This method greatly improved ease of use. Whereas the monolithic designs only allowed for flushing in the sample through the inlet by using capillary forces, the dual chip design has a very high sample compatibility as it allows for direct sample preparation and transfer onto the electron transparent windows. This allows for local dropcasting instead of contaminating the complete chip, dry transfer of powders and nanowires, and accurate placement of lamellas in the focused ion beam (FIB) [8]. Moreover, the chips can be taken apart after the TEM experiment, enabling post-analysis using other characterization techniques such as atomic force microscopy (AFM). A disadvantage, however, was that tolerances on these small O-rings are usually on similar scale as the required compression to obtain vacuum in conditions like these. Therefore, obtaining a leak-tight assembly may require multiple attempts.

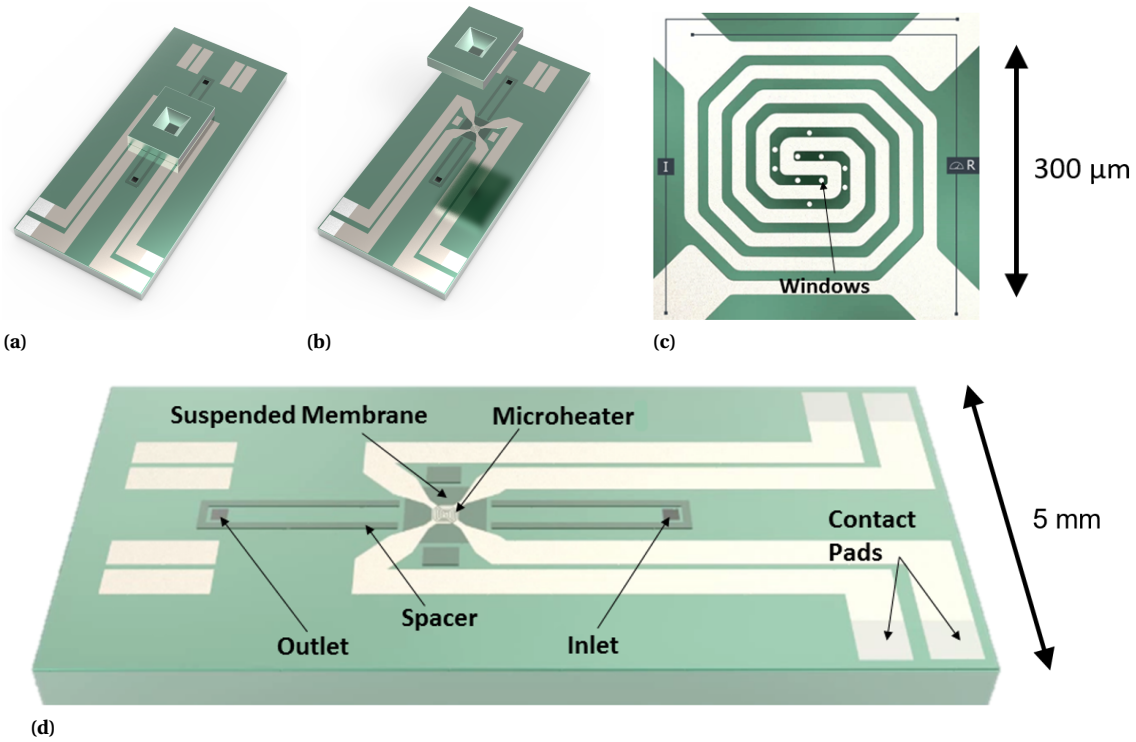

Figure 2.8: The Nanoreactor as presented by Pérez Garza *et al.* [8, 9]. **(a)** The Nanoreactor with stacked bottom and top chip. **(b)** The Nanoreactor with lifted top chip, revealing the Microheater embedded in the bottom chip. **(c)** Close-up of the encapsulated double spiral Microheater. As indicated by *I* and *R* the outer two electrical contacts are used to supply the current and the inner two to measure the resistance. Together they form the four-point-probe that allows for local closed-loop feedback temperature control ensuring temperature accuracy and stability even in changing gas environments (2.1.3, accuracy and stability). The electron transparent windows are located in the center of the Microheater, within the area of homogeneous temperature. The silicon nitride windows have a diameter of 6 µm and thickness of 22 nm. **(d)** Schematic overview of the bottom chip, indicating the suspended membrane with the Microheater in its center, the metal wires that go from the Microheater to the contact pads that provide the electrical interface to the holder, the gas inlet and outlet, and finally the 5 µm thick spacers that guide the gas past the Microheater and define the spacing in between the bottom and top chip and, therefore, the gas layer thickness.

- making both the bottom and top membrane in one chip, completely omitting the need to seal two chips. Next to being carbon contamination free, this monolithic design was able to go to a much higher pressure—up to 14 bar—by connecting the top and bottom membrane by an array of pillars [46]. Although this design surpasses all its predecessors in terms of pressure performance, the microfabrication is rather complicated and, compared to the dual chip design, samples can only be flushed in through the gas inlet or outlet. The consequence is a low success rate on sample deposition and a significant chance of clogging of the flow channel.

In addition to this list, Mele *et al.* [58] optimized the fabrication flow chart of the initial monolithic design by Creemer *et al.* The new wafer level fabrication technique uses wafer bonding to significantly improve fabrication speed, reproducibility, cleanliness and yield.

It turned out that the dual chip design had the largest potential; the much better sample compatibility was the decisive factor to serve a large scientific community. DENSsolutions B.V. used the dual chip design as the basis for the development of the Nanoreactor for the "Climate System". Pérez Garza *et al.* [8, 9] presented the Nanoreactor as a micro-sized laboratory enabling *in-situ* TEM studies from room temperature up to 1300 °C and gas pressures of up to 1.5 bar. The Nanoreactor is shown in figure 2.8. The major changes in this design are the heater material, which is now molybdenum, allowing to go to higher temperatures than platinum, circular design of the electron transparent windows to improve their robustness, and careful positioning of the windows inside a homogeneous temperature zone.

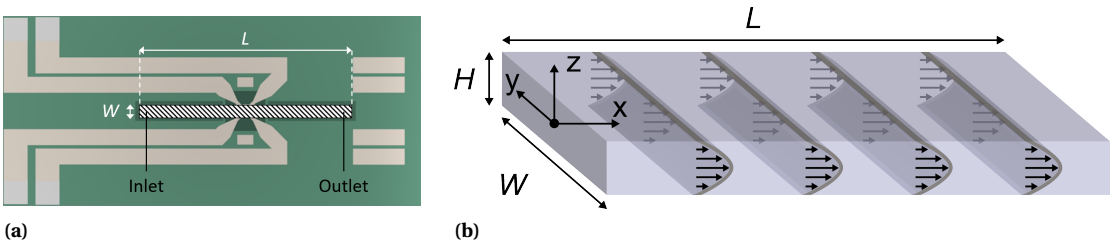

Figure 2.9: Gas flow in the Nanoreactor. **(a)** Schematic top view of the Nanoreactor bottom chip. The shaded region in between the spacers indicates the simplified gas channel volume that is used for analytical derivations and estimates. The remaining volume has relatively low flow speeds and will not be considered for now. **(b)** The dimensions and gas flow profile in the shaded region of figure (a). Assuming laminar flow, the gas speed profile is given by Poiseuille flow.

2.2.2. Gas flow: speed and turbulence

Analyzing gas flow in the Nanoreactor geometry (see figure 2.8d) starts with the Navier-Stokes equation. It relates pressure difference to flow rate and gas channel geometry by

$$\rho\frac{\partial\vec{u}}{\partial t}+\rho\vec{u}\cdot\nabla\vec{u}=-\nabla P+\eta\nabla^2\vec{u}, \tag{2.1}$$

in which ρ is density in $\mathrm{kg\,m^{-3}}$, $\vec{u}$ the flow speed in $\mathrm{m\,s^{-1}}$, t the time in s, and η the dynamic viscosity in Pa s. To simplify and enable analytical derivations and estimates, only the shaded region of the gas channel in figure 2.9a is being considered. The flow regime can be identified using Reynolds number,

$$\mathrm{Re}=\frac{\rho u H}{\eta}. \tag{2.2}$$

Gas flow is turbulent for Re > 4000 and laminar for Re < 2300 [146]. However, in comparable microchannel geometries, laminar flow was only obtained at Re < 400 due to surface roughness [147]. To make an estimate of the relevant regime, the typical numbers $H = 5\,\mu\mathrm{m}$ for the height of the gas channel [8], $\rho_{\mathrm{air}} = 1.2\,\mathrm{kg\,m^{-3}}$, $\eta_{\mathrm{air}} = 1.8\cdot10^{-5}\,\mathrm{Pa\,s}$ and $u = 1\,\mathrm{m\,s^{-1}}$ (based on gas flow speeds Harley *et al.* [147] found in comparable microchannel geometries at representative conditions), result in Re = 0.4. So assuming laminar (Poiseuille) flow, steady-state, and a one dimensional flow profile (because $W >> H$), equation 2.1 reduces to

$$\frac{\partial P}{\partial x}=\eta\frac{\partial^2 u_x}{\partial z^2}. \tag{2.3}$$

Integrating twice over z, using boundary conditions $u_x = 0$ at $y = H/2$ (or at $y = -H/2$) and $\partial u_x/\partial y = 0$ at $y = 0$ gives the flow speed over z:

$$u_x=\frac{1}{2\eta}\frac{\partial P}{\partial x}\left(z^2-\left(\frac{H}{2}\right)^2\right), \tag{2.4}$$

which is plotted in figure 2.9b. By spatial integration of the flow speed, the volumetric flow rate is found to be

$$Q=\int_{y=-W/2}^{W/2}\int_{z=-H/2}^{H/2}u_x\,dz\,dy=\frac{-1}{3\eta}\frac{\partial P}{\partial x}H^3W. \tag{2.5}$$

Note that, to simplify the math, density and dynamic viscosity are considered independent of pressure throughout this derivation. This means that incompressible flow has implicitly been assumed. On the contrary, gas is very compressible which expresses itself mostly in an increasing volumetric flow rate upon decreasing pressure, due to conservation of mass. Also, it will result in a slightly nonlinear pressure gradient. However, as long as the pressure drop is small relative to the average pressure, the assumptions are valid. Most important is that equation 2.5 makes it very clear that gas flow is very sensitive to variations in the height of the gas channel. Although the flow speed can be tuned by adjusting the applied pressure, this hinders reproducing the exact same gas flow conditions. It also explains the large differences in flow speed that Mele *et al.* [58] report on. They attribute the differences they found to dust particles that can end up on the spacers and increase the space between the top and bottom chip. Therefore, it is important to assemble the Nanoreactor in a clean environment.

Very high flow speeds can be obtained in microchannels as the low volumetric flowrates make it rather easy to apply large pressure differences on the inlet and outlet. Care has to be taken that isothermal flow cannot simply be assumed at very high flow speeds due to friction and rapid gas expansion. The temperature in the center of the gas channel, where the flow speed is highest, will be lower than the temperature at the gas channel walls. To stay within differences of 1 %, the flow speed should not exceed $u_{x,max} = 69\,m\,s^{-1}$ for air [147].

2.2.3. Mechanical properties: membrane deflection and spatial sample drift

So far, the spacing between the bottom and top chip was considered to be defined by the spacers. However, due to the large pressure difference between the in- and outside the Nanoreactor, and because of the high aspect ratio between the thickness and lateral dimensions of the membrane, it has nearly no bending stiffness, resulting in significant deflections. Figure 2.10a schematically shows how the Nanoreactor membranes deflect at high pressures. The relation between pressure and deflection at the center of the membrane [148] is given by:

$$P = C_1 \frac{t\sigma_0}{a^2} w + C_2 \frac{t f(\nu) E}{a^4 (1-\nu)} w^3, \tag{2.6}$$

in which P is the pressure inside the Nanoreactor in Pa, t is the membrane thickness in m, σ_0 is the residual stress in Pa, a half the edge length in m, w is the deflection in m, E is the Young's modulus in Pa, ν is the Poisson's ratio, and C_1, C_2 and $f(\nu)$ are geometry and model dependent parameters. Although the latter parameters vary from source to source, equation 2.6 is widely accepted [45, 87, 88, 107, 149–152] and experimentally verified for silicon nitride membranes [150]. Typical values for the parameters are $C_1 = 3.0$–3.5 , $C_2 = 1.3$–2.0 and $f(\nu) \approx 1 - 0.27\nu$.

Creemer *et al.* [45] found the deflection of the membrane to be ~17 µm for a gas pressure of 1 bar. This increases the gas layer thickness in the Microheater region from 4 µm (defined by the spacer thickness) up to 38 µm (maximum gap between deflected membranes). The gas layer thickness varies significantly with pressure, as shown in figure 2.10b. In an attempt to reduce the thickness of the gas layer, Yokosawa *et al.* [153] made the membrane of similar size as the heater (~300 µm). This means that, for similar conditions, the membrane deflection is only ~5 µm, resulting in a gas layer thickness of ~14 µm. As shown in figure 2.10b, this not only reduces the total gas layer thickness, but also reduces the variation as function of pressure significantly. This means that the effect of pressure fluctuations will be less pronounced in fluctuations of membrane deflection, which means less defocussing and therefore better TEM imaging quality. The downside of this design is an increase in power consumption because of the proximity of the heater and the substrate (heat sink).

As has been discussed with regards to Microheaters in subsection 2.1.3, power consumption leads to spatial sample drift. In a vacuum environment, the only heat losses are through thermal radiation and conduction

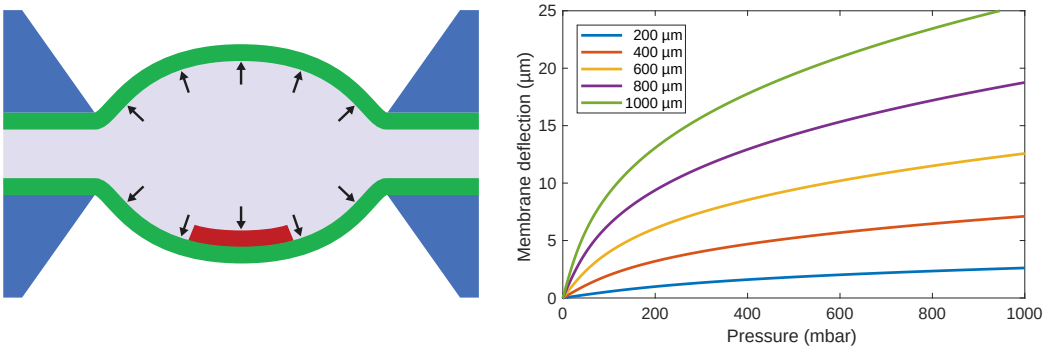

(a) **(b)**

Figure 2.10: Membrane deflection. **(a)** Schematic illustration of membrane deflection (not to scale). The gas exerts a pressure on the membrane, indicated by the arrows, due to the gas pressure difference inside (1 bar) and outside (vacuum) the Nanoreactor. **(b)** Membrane deflection as function of pressure for different membrane sizes using equation 2.6. The chosen parameters are the mean value of the range as presented in the text. The material properties are taken from Creemer *et al.* [45].

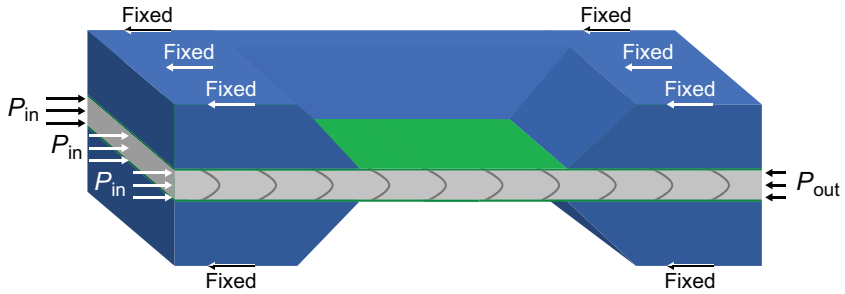

Figure 2.11: Three-dimensional schematic of a Nanoreactor with the substrate in blue, membrane in green and the gas layer in gray (a detailed version of the gas layer can be found in figure 2.9b). As the gas pressure at the inlet (P_{in}) is higher than the gas pressure at the outlet (P_{out}), the flowing gas exerts a force on the Nanoreactor through friction between the gas and the surfaces of the bottom and top chip. This force is balanced to keep the chip in place. Both the top and bottom chips are mechanically fixed to the metal holder by compressed O-rings that provide vacuum sealing (not shown). The exerted forces may cause a few nanometers of mechanical drift upon changing pressure differences.

through the membrane. The Nanoreactor requires about three times as much power to reach the same temperature because the thin gas layer conducts heat through the gas channel as well as to the membrane of the top chip. The initial drift that Mele *et al.* [29] measured just after a 500 °C temperature ramp was 3.3 nm s^{-1}, exponentially decaying with a time constant of 137 s. Although drift values are hard to compare as not everyone mentions the settling time they used, these values are higher than what has been reported before for Microheaters.

Another factor contributing to spatial sample drift could be the lateral force exerted on the chip through friction between the gas and the chip. As flow in the Nanoreactor is typically laminar (see subsection 2.2.2), an estimate can be made of how this force relates to flow rate and the dimensions of the gas channel. The force balance shown in Fig. 2.11 shows that,

$$F = \Delta P H W, \tag{2.7}$$

in which ΔP ($= P_{in} - P_{out}$) is pressure difference in Pa, H is the channel height in m and W is width in m. Together H and W make up the area on which the gas applies pressure. Integrating over the length of the gas channel (i.e. $\partial P/\partial x = \Delta P/L$) allows substitution of equation 2.5 in 2.7, leading to

$$F = -3\eta \frac{L}{H^2} Q, \tag{2.8}$$

which shows how the exerted force depends on parameters like gas channel length, height and volumetric flow rate. This equation gives insight into what the potential drift sources are and how these can be minimized. Because of the quadratic dependence on the gas channel height, increasing it looks like the most efficient approach. This, however, influences imaging conditions, as the additional gas scatters electrons.

The gas channel in figure 2.9 is approximately 300 µm wide and 5 µm high [8]. Using equation 2.7, pressure gradients of 1, 10 and 100 mbar result in exerted forces of 0.15, 1.5 and 15 µN, respectively. The latter case is getting close to the lower regime in which MEMS mechanical actuators are used, which means that the effect of these forces may be significant [154]. If so, this type of drift is expected to have lower settling times, because once the gas flow has settled, the forces equilibrate. Instead, there will be drift while changing pressure and flow rate settings as then the forces change.

2.2.4. Thermal properties: gas expansion and thermal conductivity

As the Microheater allows to go to high temperatures, the effect of temperature on the gas properties cannot be neglected. The relation between the mechanical properties of a gas and the temperature is given by the ideal gas law,

$$PV = N k_B T, \tag{2.9}$$

with V the volume in m^3, N the number of gas molecules, k_B the Boltzmann constant in JK^{-1} and T the temperature in K. If the temperature increases while pressure and volume are kept constant, the number of gas molecules (and thus the density) has to go down. The density of an ideal (monatomic) gas is given by

$$\rho = m\frac{N}{V} = m\frac{P}{k_B T}, \tag{2.10}$$

with m the molecular mass in kg.

The thermal conductivity of gases can be derived from the kinetic theory of gases and equipartition theorem,

$$\lambda = \frac{1}{2}\rho c_V \langle u \rangle l = \eta c_V \tag{2.11}$$

in which c_V is the specific heat capacity for constant volume in $\mathrm{J\,kg^{-1}\,K^{-1}}$, $\langle u \rangle$ the mean particle velocity

$$\langle u \rangle = \sqrt{\frac{3k_B T}{m}} \tag{2.12}$$

in $\mathrm{m\,s^{-1}}$ and l the mean free path

$$l = \frac{k_B T}{\sqrt{2}\pi P \sigma^2} \tag{2.13}$$

in m, with σ the molecular diameter in m [155, 156]. Note that $\rho \propto PT^{-1}$, $l \propto TP^{-1}$ and $\langle u \rangle \propto \sqrt{T}$, such that thermal conductivity is independent of pressure and increases with the square root of temperature. These equations have been derived based on various simplifications such as modeling gas particles as elastically colliding spheres (neglecting intermolecular forces as described by the Lennard-Jones potential) and only taking into account binary collisions [157]. Additionally, depending on how the derivation is done, a different constant can be found for equation 2.11 (i.e. 1/3 instead of 1/2) [121]. So it is better to use widely available experimental data [157–161].

Equation 2.11 predicts that the thermal conductivity is proportional to the mean free path of the gas molecules. However, if the pressure goes down far enough, the mean free path is not limited anymore by collisions between gas molecules, but by the boundaries of the gas channel instead. At room temperature and atmospheric pressure, the mean free path in air is ~65 nm [162]. That is almost a factor 100 smaller than the gas channel height, which means still ~99 % of the collisions are intermolecular. However, when the pressure goes down to 100 mbar (factor 10) and the temperature goes up to 1000 °C (factor 4.3), the mean free path increases by a factor 43 to 2.8 µm. In this case only ~50 % of the collisions are intermolecular. Therefore, if the mean free path is in the same order of magnitude as the gas channel height, large deviations can be expected from thermal properties in the laminar flow regime and equations 2.11 and 2.13 no longer hold.

The thermal conductivity of gases on the microscale as function of pressure can be calculated from

$$\lambda_P = \frac{\lambda_{atm}}{1 + B\left(\frac{P_{atm}}{P}\right)\mathrm{Kn}}, \tag{2.14}$$

in which B is a gas and surface roughness dependent constant of approximately 1–3 and Kn is the Knudsen number,

$$\mathrm{Kn} = \frac{l}{H}, \tag{2.15}$$

which differentiates laminar flow (Kn < 0.01), molecular flow (Kn > 1.0) and the transition regime from each other [147, 163, 164]. Based on the numbers for air, and including membrane deflection, the Nanoreactor can be operated in conditions that result in 0.002 < Kn < 0.56. Figure 2.12 shows how the thermal conductivity of air depends on the gas pressure for different pore sizes in porous media. It confirms that the Nanoreactor operates in the transition between laminar and molecular flow regimes, but closer to the laminar-side.

As later on gas mixtures will be discussed, the extended version of equation 2.11 for mixtures of gas A and B is given by

$$\lambda_{AB} = \frac{\lambda_A}{1 + \Phi_{AB}(N_B/N_A)} + \frac{\lambda_B}{1 + \Phi_{BA}(N_A/N_B)} \qquad \text{with} \qquad \Phi_{AB} = \left(\frac{\sigma_A + \sigma_B}{2\sigma_A}\right)^2 \sqrt{\frac{m_A + m_B}{2m_B}} \tag{2.16}$$

[156, 157]. The gas conducts heat in all directions as well as carries heat away with the flow. Which one is most significant will depend on the flow speed. The Péclet number for heat transfer is given by,

$$\mathrm{Pe_{heat}} = \frac{\xi u}{\kappa}, \tag{2.17}$$

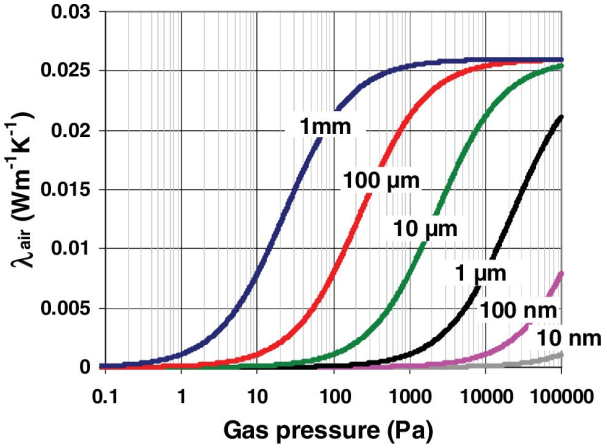

Figure 2.12: Thermal conductivity of the air as a function of pressure for different values of the pore size at 300 K, as presented by Félix *et al.* [165]. The Nanoreactor typically operates in the region between 100–1000 mbar (10 000–100 000 Pa) with gas layer thickness between 5–40 µm due to membrane deflection.

with ξ the characteristic length over which the heat transport takes place m and $\kappa\left(=\lambda/(\rho c_P)\right)$ the thermal diffusivity in $m^2\,s^{-1}$. It differentiates the dominance of heat transfer through motion ($Pe_{heat} > 10$), thermal conduction ($Pe_{heat} < 0.1$) and the transition regime in between, in which both play a significant role [166]. The typical numbers $\xi = H = 5\mu m$, $u_x = 1\,m\,s^{-1}$ and $\kappa = 22\cdot10^{-6}m^2s^{-1}$ [167] result in $Pe_{heat} = 0.23$, so it appears that the Nanoreactor operates in the transition regime. Note that H can increase up to 40 µm, increasing the Péclet number, and that a higher temperature will result in higher thermal diffusivity and, therefore, a lower Péclet number.

2.2.5. Gas switching: advection and diffusion

Convection takes place through advection (transport by bulk motion) and diffusion (transport by random molecular motion). However, depending on the situation, one can be dominant over the other. To analyze the time delay in gas switching, the dominance of either of them should be determined. The Péclet number for mass transfer is given by,

$$Pe_{mass} = \frac{\delta u}{D}, \tag{2.18}$$

with δ the characteristic length over which the mass transport takes place in m and D the diffusion coefficient in $m^2\,s^{-1}$. It differentiates advective flow ($Pe_{mass} > 10$), diffusive flow ($Pe_{mass} < 0.1$) and the transition regime in between [166]. Two different characteristic lengths are present; diffusion over the height over the channel $\delta = \frac{H}{2}$ and lateral diffusion $\delta = \frac{W}{2}$ (both divided by two because the highest flow speeds occur in the center, so the relevant distance is from the center to the edge). Using $D = 2.1\cdot10^{-5}m^2s^{-1}$ for oxygen in air [91] and $u = 1\,m\,s^{-1}$, the results are $Pe_{mass} = 0.12$ and $Pe_{mass} = 48$, respectively. This means the concentration profile is very homogeneous in height, while laterally advection dominates. As flow speed will differ from one region to another because of the high aspect ratios of the gas layer, large concentration gradients can occur in lateral directions.

If advection dominates, the incoming gas simply pushes out the gas that was initially present in the Nanoreactor. In this case, the mathematics are straightforward; integration over the flow path in the channel divided by the local gas flow speed (see subsection 2.2.2) gives the gas switching time. If diffusion dominates, the diffusive flux of gases is given by Fick's first law,

$$\vec{J} = -D\nabla c, \tag{2.19}$$

with c the concentration in $mol\,L^{-1}$. The diffusion coefficient is proportional to the mean particle velocity and mean free path length. These can be obtained by minor adjustments to equation 2.12 and 2.13, which are

$$\sqrt{\frac{1}{m}} = \sqrt{\frac{1}{m_A} + \frac{1}{m_B}} \qquad \text{and} \qquad \sigma = \sigma_{AB} = \frac{1}{2}(\sigma_A + \sigma_B). \tag{2.20}$$

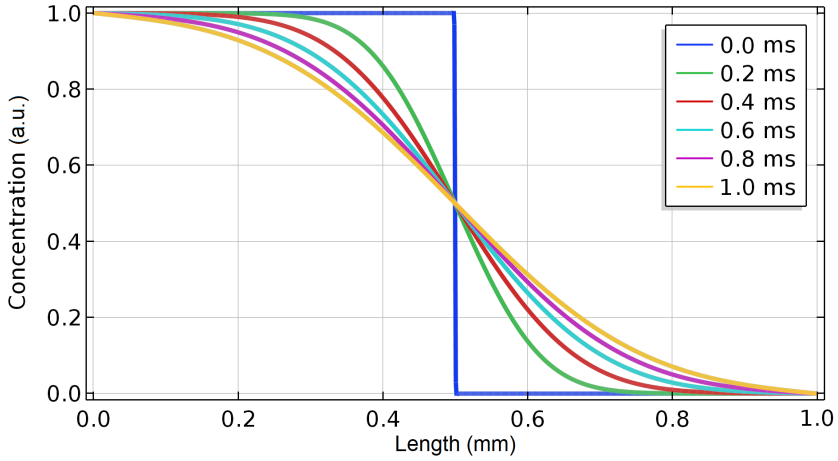

Figure 2.13: Temporal progression of the concentration profile when two initially pure gases meet, for a binary diffusion coefficient of $D = 2.1 \cdot 10^{-5} \mathrm{ms}^{-1}$. Equation 2.19 states that diffusive flux is proportional to the steepness of the concentration gradient. As a result, diffusion always smoothens curves as time progresses. The random movement, on which the diffusion process relies, causes some particles to move further than others in the same time frame. Therefore some particles are found further from their starting point than others.

Using these relations, the dependencies of the diffusion coefficient are found [168]. The binary diffusion coefficient is given by

$$D \propto ul = \frac{\sqrt{3}(k_\mathrm{B}T)^{\frac{3}{2}}\sqrt{\frac{1}{m_\mathrm{A}}+\frac{1}{m_\mathrm{B}}}}{\sqrt{2}P\sigma_{\mathrm{AB}}^2}. \tag{2.21}$$

As temperature and pressure can vary over large ranges during experiments, the most important result from this equation is that $D \propto T^{\frac{3}{2}}P^{-1}$. It tells that diffusive flow is slowest at high pressure and low temperature, for the Nanoreactor that would mean atmospheric pressure and room temperature.

Equation 2.19 states that the diffusive flux is governed by the diffusion coefficient and the concentration gradient. The latter changes over time; when the gas particles move, the spatial concentration smoothens as shown in figure 2.13. Because of the gradual spatial change of the profile (except for $t = 0$), it is hard to define how far gas A has penetrated in gas B and the other way around. The standard measure for this is the diffusive penetration depth,

$$\zeta_{\mathrm{pen}} = 2\sqrt{Dt}, \tag{2.22}$$

in which t is the elapsed time in s [167]. Using $D = 2.1 \cdot 10^{-5} \mathrm{m}^2\mathrm{s}^{-1}$ for oxygen in air [91], it is found that $\zeta_{\mathrm{pen}} = 0.13\,\mathrm{mm}$ on $t = 0.2\,\mathrm{ms}$ and $\zeta_{\mathrm{pen}} = 0.29\,\mathrm{mm}$ on $t = 1.0\,\mathrm{ms}$. If imaginary tangent lines would be drawn to the concentration profiles in figure 2.13, it follows that these values are quite well in agreement with how far gas A has moved into gas B.

Another way to look at it is from the perspective of the gas particle rather than from the continuum approach that equation 2.19 suggests. Using a statistical approach, the expectation value of the root mean square (rms) position of the particle can be calculated. The rms distance a gas particle has traveled is given by

$$\zeta_{\mathrm{rms}} = \sqrt{2nDt}, \tag{2.23}$$

in which n is the number of considered dimensions [169]. These definitions have a fundamentally different interpretation: ζ_{pen} is a measure of how far gas A has penetrated in gas B assuming that at $t = 0$ there was a infinitely sharp gradient between them, ζ_{rms} is more general and does not necessarily involve a concentration gradient; it merely provides the average distance a particle has traveled from its original starting point. Note that $\zeta_{\mathrm{pen}} \propto \zeta_{\mathrm{rms}} \propto \sqrt{t}$. The reason that they do not increase linearly with time relates to the random motion; the gas particle is as likely to take a step forward as it is to take a step backward. In fact, the mean expectation value where to find the particle back again, is its starting position. An equal amount of particles moves in positive and negative directions, so statistically the average movement of zero.

Contrary to the gas flow speed analysis (subsection 2.2.2) in which only the gas flow speed in the channel and Microheater region are relevant, the whole gas volume needs to be considered for gas switching. Judging

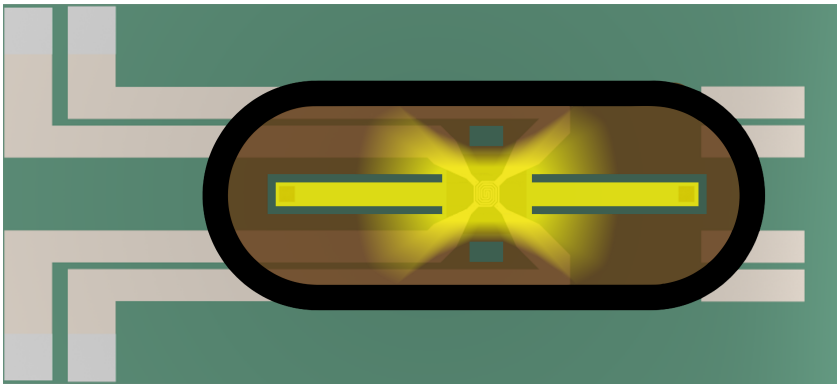

Figure 2.14: Hypothesis on which gas switching process is dominant under typical operation conditions; a pressure gradient of 50 mbar between the inlet and outlet at a Nanoreactor gas pressure of ~1000 mbar. Yellow indicates the region where gas flow speed is high and, therefore, where gas switching is likely to be dominated by advection. Brown indicates where gas flow speed is low which means diffusion is likely to contribute significantly to the gas switching speed. The gradient from yellow to brown indicates the transition in importance of advective and diffusive gas switching.

on the design of the Nanoreactor (figure 2.8) and knowing that the gas flow will be laminar, the chip can be split up in different regions in which potentially different regimes are dominant. When a pressure gradient is applied between the gas inlet and outlet, gas will start flowing at relatively high speeds in between the gas guiding spacers. On the other hand, much lower gas flow speeds are expected in the regions further away from the Microheater and outside the spacers. These dead volumes do not contribute to the experiment, but have to be flushed as well to ensure high gas purity and experimental accuracy. Figure 2.14 indicates which flow regime (advective or diffusive) is speculated to be found where.

2.3. Transmission electron microscopy and application specific aspects

2.3.1. Sample preparation

Next to the thermo-electro-mechanical and gas flow performance, some requirements will come from the methods that are typically used to transfer samples to the Nanoreactor. The sample transfer methods were mentioned before in the homogeneity paragraph of subsection 2.1.3. The Nanoreactor is not very well suited for preparing FIB lamellas, as this may damage the electron transparent windows. These have to stay intact to withstand the gas pressure and high temperature. Therefore, the most common method is dropcasting. Dry dispersion and sputtering are used only sometimes.

With dropcasting, the sample particles are generally in a suspension of a volatile liquid to facilitate quick evaporation. When the liquid is evaporating, capillary forces determine where the decreasing amount of liquid situates itself; usually at corners and places with more topography [170]. Figure 2.15 illustrates the result of this effect. In the bottom chip, these spots are usually where the metal wire of the Microheater is. The extra layer gives some topography. As a result, most of the sample tends to accumulate in these regions rather than in the center of the electron transparent windows. To maximize the dropcast success rate, topography close to the electron transparent windows should be avoided or minimized if possible. There is a trade-off, as moving the heater wire further away from the electron transparent window may worsen the heat transfer rate to the sample. Alternatively, increasing the window surface area by increasing the number of windows would overcome both. Using the design guidelines provided in subsection 2.1.4, homogeneity should improve far enough to include more windows and, therefore, to enable optimization of both the dropcasting success rate as well as thermal properties.

In dry dispersion, transfer happens through on electrostatic forces. Sputtering cannot really go wrong from the chip perspective. Both of them will benefit from increasing the electron transparent window area.

2.3.2. *In-situ* experiments

To achieve atomic resolution, a TEM operates in ultra high vacuum and makes use of finely tuned electromagnetic lenses to focus the electron beam. Furthermore, the sample should be thin enough to let the electrons

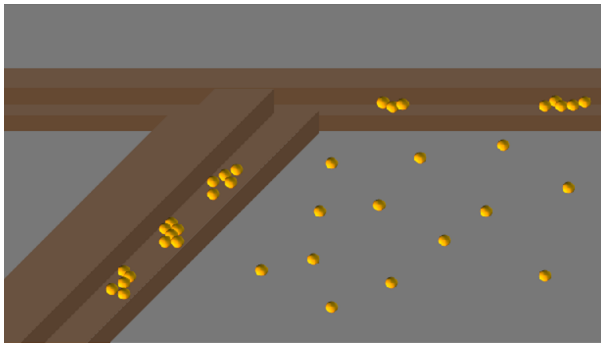

Figure 2.15: Illustration by Michen *et al.* [170] (from the supplementary information) of a TEM copper grid with a profile similar to an inverted T. Nanoparticles tend to accumulate near the corners and edges of this profile due to capillary forces that pull in the evaporating suspension.

pass through. Ideally, the electrons do not need to pass through any other materials than the sample as they distort and scatter some of the electrons, leading to image blurring and, therefore, lower maximum resolution.

To maintain ultra high vacuum, the Nanoreactor should be sealed properly to bring gas leakage into the TEM column to an absolute minimum. The Nanoreactor is sealed using a compressed O-ring, shown in figure 2.16. The smoother the surface, the better the seal. Therefore, it should be avoided to have (dust) particles on the chip. Additionally, it is important that the Nanoreactor is robust enough to withstand high pressure and temperature for a long duration. Although the volume in the Nanoreactor is very small, only ~75 nL, failure should be avoided to prevent that gas will leak into the TEM column. To ensure robustness of the Nanoreactor, the electron transparent windows should be circular, as this shape avoids stress concentrations and therefore provides the best stress distribution. In comparison, stress levels in squares of the same size are up to a factor two higher [149]. Figure 2.17a shows the differences in stress levels of simulations on circular and square windows of similar size. However, comparing diameter to edge length is not completely fair; what matters to the application of the Nanoreactor is the surface area of the window. Figure 2.17b and 2.17c show the maximum stress in the circular and square windows as function of surface area. The stress levels increase for larger windows. Therefore, it is better to include more windows instead of making them larger.

The electron transparent windows should be thick enough to withstand the pressure and thin enough to let electrons pass through (nearly) unaffected. As shown by Pérez Garza *et al.* [8], the Nanoreactor allows to image at 1 Å resolution at 1 bar pressure at 650 °C, which is considerably better than what has been achieved before by ETEM and windowed gas cells (see subsec 2.2.1). This shows that the top and bottom windows of 22 nm thick silicon nitride barely affect the attainable resolution.

As a TEM uses electrons to image, care must be taken with introducing electromagnetic components near the electron beam, as they may affect the path of the electrons and thus the resolution limit. Introducing a current in between the pole pieces, as the Microheater does, can therefore interfere with the magnetic field of the TEM, which can be as high as 2 T [171]. The magnetic field generated by the Microheater is described

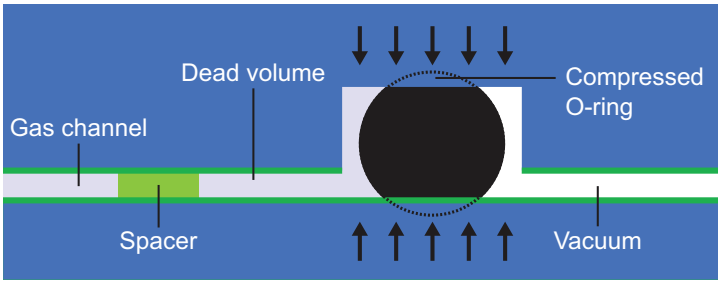

Figure 2.16: Proper vacuum sealing is ensured by a compressed O-ring. Spacers define the distance between the top and bottom chip and ensure the thickness of the gas channel is accurately defined regardless of the exerted compressive force.

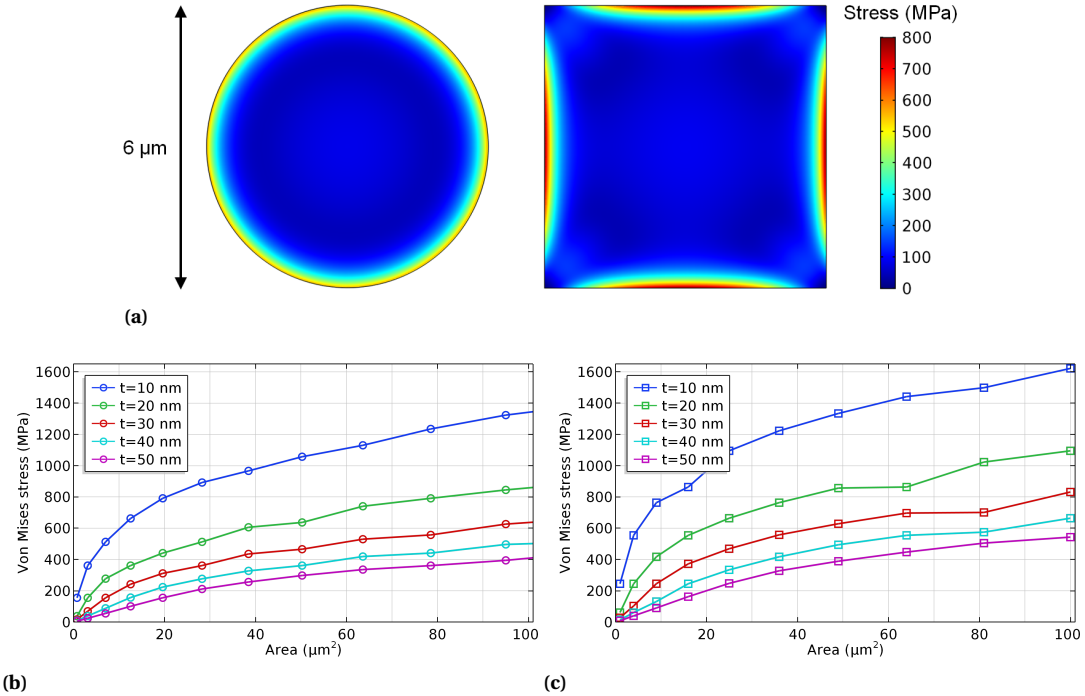

Figure 2.17: Finite element analysis on stress in silicon nitride electron transparent windows at a gas pressure of 1 bar. **(a)** The stress distribution (in MPa) in respectively circular and square windows of comparable size; the diameter and edge length are 6 µm and the thickness is 20 nm. The circular shape experiences lower stress and would therefore be more robust. **(b)** The maximum stress level in circular windows is shown to increase as function of window area for different thicknesses. The markers on the line indicate window diameters of 1, 2, 3, 4, ... from left to right. According to table 2.1, silicon nitride has a yield strength of ~750 MPa. If bulk material properties still apply, the maximum feasible window size would be 65 µm^2 (diameter of 9 µm) for a thickness of 20 nm. **(c)** Analogue to figure (b), but for square windows. The markers on the line indicate edge length.

by the Maxwell-Ampère law,

$$\oint_C \vec{B} \cdot d\vec{l} = \iint_S \left(\mu_0 \vec{J} + \mu_0 \epsilon_0 \frac{\partial \vec{E}}{\partial t} \right) \cdot d\vec{S}, \tag{2.24}$$

with $\vec{B}$ the magnetic field in T, $\vec{l}$ the closed loop over which is integrated in m, μ_0 the permeability of vacuum in H m^{-1}, $\vec{J}$ the current density in A m^{-2}, ϵ_0 the permittivity of vacuum in F m^{-1}, $\vec{E}$ the electric field in V m^{-1}, and $\vec{S}$ the area that is integrated over in m^2. Typical high-temperature Nanoreactor experiments require a stationary current of 10 mA. It follows that a single wire generates a magnetic field of 2 mT at a distance of 1 µm from the center of the wire. It could be claimed that 0.1 % is not a significant interference, but because high resolution is such an important quality of the TEM, any compromise should be kept to a minimum. Equation 2.24 has current as a vector, which means that the superposition principle can be used to lower the total magnetic field. The double spiral design includes this principle in both lateral dimensions, contrary to other designs like the meander which only has opposing currents in one direction (see figure 2.3). Therefore, the double spiral is a well suitable design for *in-situ* TEM purposes [45].

Yokosawa *et al.* [153] studied the effect of electron beam intensities on the Nanoreactor. The intensities vary from 10–1000 electrons nm^{-2}s^{-1}, at hydrogen gas pressures of 0.8 and 3.2 bar. They found no significant differences in Nanoreactor behavior and in the (de)hydrogenation temperatures. However, some sample types can be sensitive to charging through accumulation of the electrons from the electron beam. To enable high resolution imaging of these samples, it should be avoided that charge could build up that lets static electricity forces deflect the electron beam. The best way to ground the sample is by sputtering a thin electrically conducting layer before depositing the sample. However, if this is undesired due to the nature of the experiment, charging can be minimized by having the sample as close to one of the metal heater wires as possible.

2.4. Conclusion and challenges

2.4.1. Key takeaways from literature and theory

Until now, research has been focused on enabling the *in-situ* gas technology in a reliable way. The production flow charts have been optimized and a lot of attention has been given to improving and upscaling fabrication yield as well as obtaining high resolution in the TEM. Now that these things have gotten much better and are implemented, the focus can be shifted towards the optimization of the design and the specifications of the Nanoreactor. If the specifications can be improved, the Nanoreactor can provide more accurate experimental conditions. Obtaining higher accuracy and precision in experimental conditions will provide more accurate experimental results. This will enable researchers to obtain more accurate results and potentially perform types of research that could not be done before, pushing science to a higher level.

Literature contains numerous examples and attempts of improving the performance of Microheaters for various purposes, but only a limited amount of literature is available on Microheaters in combination with microchannels for gas flow. It is evident that this is because of the higher complexity that combining these systems brings and because of the (so far) more specific and narrower application field for this technology. Regarding the Microheater, the key takeaways had already been summarized in table 2.2 and 2.3. As the principles behind the Microheater have stayed the same, the design guidelines provided by these tables apply to the Nanoreactor as well. The Nanoreactor brings additional design guidelines that are extensions of the existing ones and also introduces new performance parameters. The existing lists of design guidelines are supplemented with those given in table 2.4. Performance parameters regarding *in-situ* TEM applications have also been included.

In addition to the design rules, it can be concluded that a lot of performance parameters are interdependent, so many optimization routes will encounter trade-offs between specifications. Moreover, it has become clear that the Nanoreactor operates in various transition regimes regarding thermal convection, laminar or molecular flow, and gas advection or diffusion.

2.4.2. Research questions

To achieve the goal that was set in the problem statement (section 1.2), the main research question for this project has been defined as:

Through which mechanisms is real-time TEM imaging limited and how can their influence be minimized?

Intermediate questions that require an answer to advance towards the main question are:

- What are the relevant parameters in causing interventions while applying and changing stimuli?
- How can the relations between parameters and stimuli be characterized?
- How and to what extent can the performance of the Nanoreactor be improved to pursue the goal?

In anticipation of the answer to the first intermediate question, the latter two break down to:

- What limits the current performance on:
  - membrane deflection
  - spatial sample drift
  - temperature homogeneity
  - temperature stability
  - gas flow speed
  - gas switching time?
- How can limitations be overcome to improve:
  - membrane deflection
  - spatial sample drift
  - temperature homogeneity
  - temperature stability
  - gas flow speed
  - gas switching time?

Table 2.4: Additional design guidelines to table 2.2 and 2.3 to develop and optimize Nanoreactors regarding thermo-electro-mechanical, gas flow and gas switching, and TEM application aspects.

Thermo-electro-mechanical		
Performance parameter	**Influential factors**	**Design guidelines**
Membrane deflection	• Gas pressure • Membrane dimensions • Young's modulus • Residual stress	• Reduce the size of the membrane • Increase the thickness of the membrane • Choose membrane materials with high Young's moduli • Increase tensile residual stress
Mechanical Stress	• Membrane deflection • Shape and size of the electron transparent windows	• Reduce membrane deflection • Make the windows circular • Increase the thickness of the windows • Reduce the diameter of the windows
Spatial sample drift	• Pressure drop over gas channel • Heat losses to the gas • Heat losses to the top chip	• Increase the gas channel height • Decrease the volume of the heated gas • Insulate the top chip substrate from the heater by making membranes thinner and larger
Temperature homogeneity	• Péclet number for heat transfer	• Prevent that heat advection dominates over heat conduction
Temperature stability	• Changes in gas flow speed • Changes in gas type	• Use fast closed-loop feedback • Bring the four-point-probe as close as possible to the center of the Microheater
Power consumption	• Bottom membrane size • Top membrane size • Thermal conductivity of the gas	• Increase bottom membrane size • Match top membrane size to bottom membrane size • Choose carrier gases with poor thermal conductivity
Response time	• Thermal mass of the gas	• Reduce the gas volume
Gas flow and gas switching		
Performance parameter	**Influential factors**	**Design guidelines**
Gas flow speed	• Gas channel dimensions • Gas viscosity • Applied pressure difference • Spacer design	• Confirm that flow is laminar through Reynolds number • Flow speed below Mach 0.2 to preserve isothermal flow • Check Knudsen number for molecular flow effects • Increase gas channel height (scales to third power) • Let spacers guide gas towards the sample
Gas switching time	• Péclet number for mass transport • Dead volume • Gas chamber dimensions	• Increase the gas flow speed • Make sure advection dominates over diffusion • Avoid redundant volume
TEM application		
Performance parameter	**Influential factors**	**Design guidelines**
Sample compatibility	• Detachable sample carrier • Sample accumulation during dropcasting	• Have a dual chip design • Reduce capillary forces by minimizing topography • Increase the distance between heater lines and windows
Resolution	• Gas layer thickness • Electron transparent window thickness	• Reduce membrane deflection • Reduce the gas channel height • Reduce the electron transparent window thickness
Ultra high vacuum	• Gas leakage • Gas volume (in case of failure)	• Make sure the membrane and windows are robust • Ensure sealing through compressed O-rings or glue • Reduce the gas volume
Magnetic field interference	• Electric current in between the polepieces	• Compensate using close currents in opposing directions • Use a double spiral
Charging	• Electron beam intensity • Grounding of the sample	• Deposit a thin conductive layer on top of the membrane • Decrease distance between heater lines and windows

3

Methods for experimental characterization and finite element modeling

3.1. Approach and conceptual solutions

3.1.1. Optimization approach and target setting

The literature and theory study has defined how the Nanoreactor performance is expressed and which factors are of influence. Design guidelines have been suggested to bring the state of the art of different technologies together into one device. A lot of performance parameters have been introduced, but not all of them are equally relevant for the Nanoreactor. Some are rather independent of the MEMS design, and some translate to soft (design) constraints which are already met by the current design. The design constraints are defined in subsection 3.1.3. This project will limit itself to the design of the Nanoreactor. The intention is not to change the fabrication procedure as it has already been thoroughly optimized in the past (see subsection 2.2.1). Materials, layer thicknesses and the interface towards the chip holder will be taken as hard constraints. This ensures the new design will be able to withstand the imposed mechanical and thermal stresses, and maintains the current operating range and lifetime regarding pressure and temperature.

The focus of this project is on membrane deflection, spatial sample drift, temperature homogeneity, temperature stability, gas flow speed, and gas switching time. The relevance of these performance parameters has been described before in the problem statement (section 1.2). Some rely partially on material or fabrication related aspects, which will not be considered. The optimization approach will consist of the following steps:

1. Characterize the performance parameters and specifications of the current Nanoreactor design. Use literature and theory (chapter 2) to reflect on the characterization results. Ensure that results can be explained and understood using the underlying physics.
2. Obtain a reliable and accurate finite element model using COMSOL Multiphysics, to understand the underlying physics which govern the behavior of the Nanoreactor. The simulations should match the results of the characterization using substantiated physics settings, parameters and properties. These may be obtained through appropriate literature or characterization. If discrepancies occur between simulations and experiments, the causes should be identified and the model adjusted. A general error and reliability analysis of the finite element model is performed in appendix E.
3. Determine optimization steps based on the understanding and knowledge acquired from characterization and simulations of the current design, and the design guidelines of table 2.2, 2.3 and 2.4. Either the causes that limit the performance should be eliminated, or their symptoms should be minimized.
4. Simulate optimization steps using the physics settings, parameters and properties that were obtained during modeling the current Nanoreactor. Iterations between this and the previous step will occur until either satisfactory results are obtained or the optimal result is found within the given constraints. The goal of this step—and the goal of this project—is to propose an optimized version of the Nanoreactor based on analytical models and finite element analysis.

The optimization steps have to apply to the operation range at which the Nanoreactor is used. These ranges are temperatures of 20–1000 °C, pressures of 100–1000 mbar, and gas flow rates of 0–1 mL min^{-1}. The optimization emphasis will be on high-pressure scenarios, for two reasons: it simplifies the models as the effect of molecular flow is smaller at high pressure and, more important, the Nanoreactor was developed for enabling high-pressure operation. In a typical gas experiment, a mixture of gases will be used; an inert carrier gas composing the most of the mixture and one or two reactive gases. The carrier gas is usually either nitrogen or helium, which differ significantly in thermal properties and cover a large part of the possible range. Therefore, characterization and simulations will be performed based solely on these two gases. Furthermore, optimization will generally be aimed at (realistic) worst case scenarios because these define the specifications of the Nanoreactor.

Based on the state of the art in Microheaters, Nanoreactors and other comparable MEMS devices, and the theory on relevant physics, the goals and optimization targets can be set:

- **Membrane deflection: less than 10 μm**
  Deflection should be less than 10 μm at 1 bar and, more importantly, the sample should stay in focus with pressure fluctuations of 5 mbar. This pressure stability should be attainable by the gas supply system in stationary conditions.
- **Spatial sample drift: reduce power consumption by 10%**
  As this parameter is hard to quantify beforehand, a target will be set for its main influential factor: power consumption may not be higher than in the current Nanoreactor design. To keep a safety margin: the power consumption of the optimized design should be 10 % less than in the current design.
- **Temperature homogeneity: improve to 97.5%**
  Literature reports homogeneity as high as 99 % for vacuum conditions, but the Nanoreactor should be compatible with multiple gases with different thermal properties. Heat loss mechanisms differ with the operating conditions, resulting in a homogeneity that cannot be expected to get as good as for an optimized heater solely for vacuum conditions. The target is set to 97.5 %.
- **Temperature stability: better than 1% while changing gas**
  Fluctuations should not exceed 0.01 °C in stationary conditions, which has already been achieved. The temperature can fluctuate by 1 % during changes of environment. This would be the maximum acceptable difference considering an overall 95 % temperature accuracy is desired.
- **Gas flow speed: 90% should pass sample region**
  At least 90 % of the gas should pass the sample region, which will be defined as the membrane. Theoretically 100 % should be possible. However, microfabrication tolerances require that features leave some open space in between, and some gas will always find its way through the O-ring groove.
- **Gas switching time: $\mathbf{Pe_{mass} \geq 1}$**
  The time it takes to switch gases depends on gas viscosity, diffusivity and the gas flow speed. Therefore, no direct number can be put. However, there should be no dead volume. This demands that gas switching is governed by advection; the Péclet number for mass transfer should be larger than one.

3.1.2. Conceptual solutions

The concepts to obtain the desired optimizations have already been introduced as the design guidelines. However, the most important performance parameters have now been identified and, moreover, the scope of this project has been delineated. A few solutions that had seemed interesting from the theoretical perspective, will not be considered because of practical irrelevancies. For example, compressive stress due to thermal expansion (table 2.3) is a lot less relevant to the Nanoreactor, where the gas pressure causes tensile stress all over the membrane. In subsection 2.2.3 it has been predicted that changing gas flow speeds may cause significant drift. However, in practice, changing gas flow speeds goes hand in hand with pressure fluctuations causing a temporary loss of focus, which means the drift cannot be measured and quantified. Therefore, it would not be useful to optimize for this cause of drift. Instead, the focal loss problem should be solved, which therefore is one of the goals. Temperature accuracy largely relates to microscale calibration techniques, not to the Microheater design. However, how temperature accuracy may change when switching gas type and pressure, may be of concern to the design. The most relevant design guidelines will be considered for the conceptual solutions:

- **Reducing membrane size**. As materials will not be changed, the only tweakable variable is the membrane size, which also is the most influential factor on absolute membrane deflection and fluctuations due to gas pressure stability. Care has to be taken for the trade-off with power consumption. To prevent a power consumption increase, the heater should be decreased in size accordingly.
- **Reducing the heater size** may not be sufficient to further reduce power consumption and thus spatial sample drift. It should be determined how power consumption depends on the thickness of the gas layer, and the **ratio between bottom and top membrane size**. Depending on the Péclet number for heat transfer, it may be best to have both the membranes of equal size, or it may be beneficial to have a different membrane size in the top chip than in the bottom chip instead.
- Homogeneity will be improved through using **varying heater linewidth and pitch** within the tolerances prescribed by microfabrication. Care has to be taken not to increase current density dramatically when reducing heater linewidth. To prevent hotspots, **sharp corners should be omitted** completely.
- To ensure both temperature stability as well as accuracy, the **connections of the four-point-probe** should be reconsidered. The gas type influences the temperature distribution, which affects the temperature-resistance relation. To which extent this effect is relevant has to be identified. If it is considerable, the sensing probes should be moved closer to the core of the heater.
- The spacers guide the gas from the inlet in the general direction of the heater. However, the channel is not closed, so a significant gas portion passes the sample untouched. To maximize interactions, the **spacer design** should be optimized to guide as much gas as possible towards the Microheater. To enhance gas switching times, **dead volume should be minimized**. This also requires a different spacer design that either minimizes dead volume by filling up the space or allows the full gas chamber to be flushed faster. Moreover, there should be enough spacer area present to support the top chip.

3.1.3. Design constraints

As mentioned in subsection 3.1.1, not every performance parameter is equally important or requires improvement. These will be referred to as soft constraints; the current design already meets the requirements. It is important to identify these constraints and their dependencies such that it is understood beforehand how design changes may affect specifications that are not being considered part of the optimization goal. No compromise should be made on these specifications, but with proper substantiation some deviation is acceptable. The soft constraints will be discussed using the design guidelines in table 2.2, 2.3 and 2.4. A conclusive summary is provided in table 3.1.

Table 3.1: Performance parameters and their corresponding design constraint. Concluded from subsection 3.1.3.

Performance parameter	Design constraint
Mechanical stress	Membrane and circular windows of same or reduced size
Thermal stress	Do not increase heater size
Stress distribution	No sharp geometrical transitions and sharp corners
Range and lifetime	Do not increase current density and no sharp corners in the heater spiral
Temperature accuracy	Do not increase current density in hottest area
Response time	Do not increase thermal mass and thermal resistance
Sample compatibility	Do not decrease electron transparent window area
Resolution	Do not increase gas layer thickness
Ultra high vacuum	Do not change vacuum sealing method
Magnetic field interference	Keep the double spiral and do not increase the total current
Charging	Leave space nearby heater lines for windows

Mechanical stress is caused by the gas pressure difference inside and outside the membrane. Suspended membranes allow for absolute stress measurements [172], but since knowing relative stress levels between the current and an optimized design are sufficient, finite element analysis can be used. Since the microfabrication procedure and the layer thicknesses are considered hard constraints, the only variable is the lateral size. Figure 2.17 has already shown that an increasing size results in higher stress levels, because the total force on the membrane scales with its area. As long as the membranes and windows will not increase in size

and diameter, the mechanical stress can be expected not to increase. As the membrane size will be reduced (subsection 3.1.2), stress levels will only become less.

Thermal stress occurs at material boundary layers. However, the stack of layers will not be changed. Therefore, stress levels will generally not increase. Because the heater size will be reduced (subsection 3.1.2), the hot area will be smaller, which reduces the thermal stress.

Stress distributions are more evenly in circular shapes than squares (figure 2.17a). However, if the fabrication procedure remains fixed, the membrane will keep the same square shape and stress distribution. Circular shapes are used for the electron transparent windows, which are much thinner and fragile. Furthermore sharp geometrical transitions and sharp corners must be avoided as stress concentrations may occur [173].

Range and lifetime depend mostly on the materials used and temperature ranges explored. Since both do not change, and stress levels are expected to decrease, the remaining lifetime limitation could come from electromigration and current crowding. To prevent hotspots, sharp corners in the heater spiral should be avoided. Electromigration can be minimized by reducing the current density or by using a discontinuous heating mode. The latter is not an option; equation 2.24 shows that this will result in varying magnetic fields, which should be avoided inside TEM resolution.

Temperature accuracy depends on heater degradation, calibration and control. The latter two are not directly related to the MEMS design. During high-temperature operation, annealing and electromigration occur faster. Degradation can be prevented by annealing the chip prior to calibration, but this interferes with the fabrication procedure, which is considered a hard constraint. For electromigration, large increases in current density should be avoided. A more interesting design aspect is to analyze whether the calibration holds in different gas environments. The different gas environment will influence the temperature distribution and will therefore affect the temperature readout. Depending on the significance, this may be included in the design through a change in the four-point-probe. This aspect of accuracy will be considered in subsection 3.2.3.

Response time is currently not limited by the Nanoreactor itself, but by the controller. Therefore, this is not something that needs to be optimized regarding the MEMS device. However, the time constant of the Nanoreactor is a measure for the internal settling of the heater and thus a measure of the accuracy of the temperature stimulus. For these type of Microheaters, time constants are usually a few tens of milliseconds at most [10]. In the design, it should be taken into account that the thermal mass and the thermal resistance between the heater lines and the sample location are not impaired.

Sample compatibility can be enhanced by minimizing topography and, mostly, by increasing the windows' area as this increases the sample deposition success rate. Window area is considered an important constraint; it should stay the same or, preferably, increase within an area with high temperature homogeneity.

Resolution is limited by the thickness of the gas layer and the electron transparent windows. The latter is something that will not be changed. The gas layer will be thinner as one of the optimization targets is to reduce membrane deflection.

Ultra high vacuum can currently be maintained by the Nanoreactor [6, 8]. Therefore, as long as nothing on the vacuum sealing is changed, the leak tightness will be unchanged. The gas volume of the Nanoreactor will not change a lot as the dimensions of the chip and the interface are considered a given.

Magnetic field interference depends on the geometry of the heating spiral and the total current. The double spiral geometry should remain and the total current should not increase. As the heater size and the power consumption will be reduced (subsection 3.1.2), less current is required if the resistance stays the same.

Charging of the membrane happens due to the electron irradiation. Nearby metal wires from the heating spiral can discharge these floating charges. That means space for electron transparent windows should be assigned nearby metal heating lines, in the homogeneous area.

Other things to take into account are the microfabrication tolerances. Due to the etching process, the sides of the heater wires will have a certain roughness. This has not been a problem in the current design, but the narrower the lines, the more significant the tolerances. This will result in locally higher current densities, and in the worst case hotspots and worse temperature homogeneity. Next to that, there will be minimal feature sizes and spacings between features to have features well defined. And last, wafer thickness can vary by a few micrometers. If the suspended membrane is made through KOH-etching the silicon substrate, this directly translates to a few micron difference in membrane size, varying from wafer to wafer.

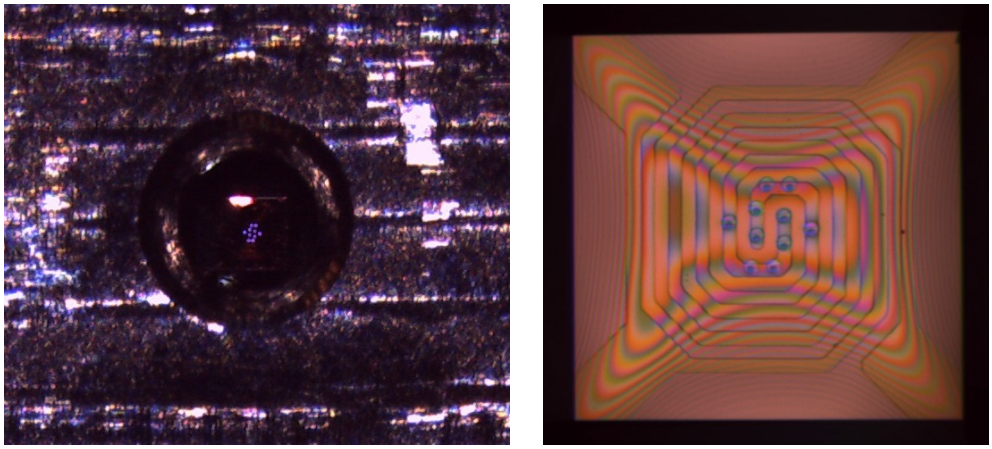

(a) TEM holder tip with Nanoreactor inside **(b)** Zoom-in on Nanoreactor in TEM holder

Figure 3.1: Optical microscopy images of the assembled Nanoreactor. **(a)** Top view of the TEM holder tip. The metal is the lid with a hole in the center to let the electron beam reach the Nanoreactor. The electron transparent windows appear as small bright spots. **(b)** The Nanoreactor inside the TEM holder at 100× magnification. It can be seen that the electron transparent windows of the bottom and top chip are aligned. The optical fringes are caused by interference due to membrane deflection.

3.2. Characterization

3.2.1. Mechanical stability

Two performance parameters are part of the mechanical stability category: membrane deflection and spatial sample drift. Both will be characterized independently as they manifest themselves on different length scales; micrometers and nanometers respectively.

Membrane deflection

The characterization of membrane deflection will be done for both the bottom and top membrane. They have a different size and layer composition because the heater is only present in the bottom chip. As became clear from equation 2.6 and figure 2.10b, deflection depends highly on membrane size. Due to microfabrication tolerances (subsection 3.1.3), membrane size can vary slightly. A Phenom Pro tabletop SEM will be used to accurately measure the size of the membrane.

The membrane deflection depends on the pressure difference between inside and outside the Nanoreactor. The ambient air pressure varies tens of millibars depending on the weather, so it must be monitored as well. The assembled Nanoreactor (shown in figure 3.1) will be placed in the TEM holder to connect it to the gas supply system. Characterization of membrane deflection as function of pressure will be done using white light interferometry (WLI), for 100–1000 mbar.

WLI is a suitable non-contact and fast technique to map height profiles. It is an often used method to measure step heights and surface roughness down to the nanometer scale [174]. Depending on the magnification, the typical field of view varies from 300×300 µm to 1×1 mm, which will fit the suspended membranes of the Nanoreactor. The technology uses the optical path differences between the sample and a reference to measure height based on interference of light. By scanning a range of heights, the surface profile is acquired with a CCD sensor. A schematic of a Mirau WLI is shown in figure 3.2a and 3.2b. Constructive interference occurs when the light reflected from the sample and the reference are coherent. White light contains a broad range of superposed wavelengths, resulting in a very short coherence length at which all wavelengths experience constructive interference [175]. This working principle is illustrated in figure 3.2c. It shows the addition of constructively interfering wavelengths, and the resulting superposition. The final intensity profile has a very sharp central peak which allows for height profile measurements with much higher accuracy than the wavelength of light.

The obtained results, dimensions of the membranes and deflection as function of pressure, will be used to make a finite element model. The purpose of the model is to understand the underlying physics to enable

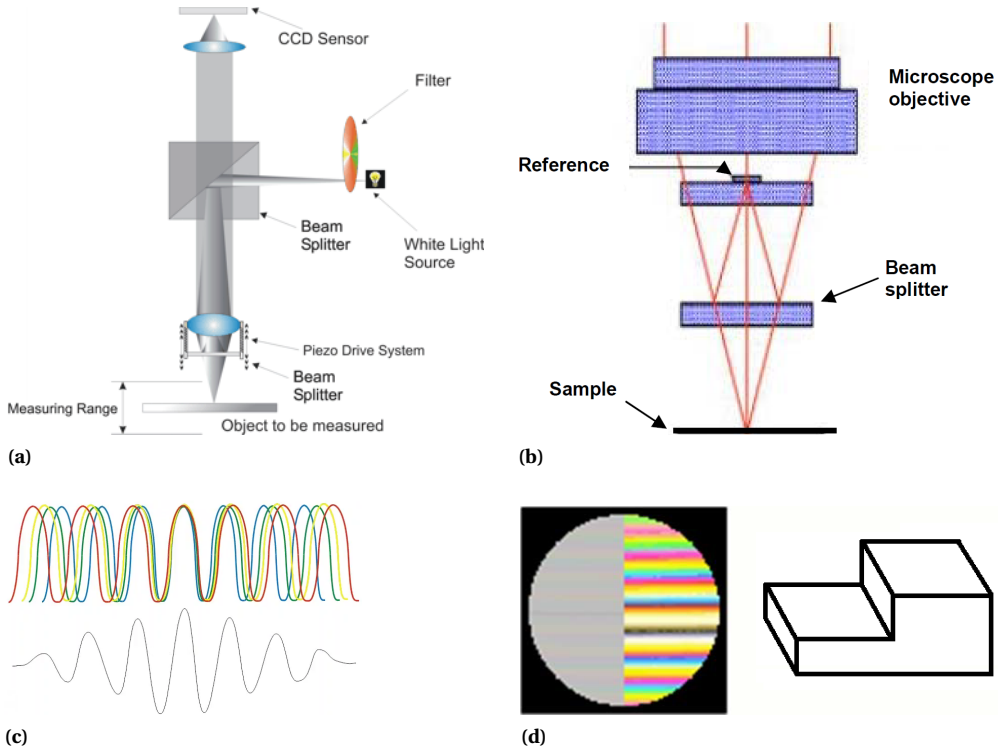

Figure 3.2: **(a)** Schematic illustration of a Mirau WLI by Blunt [174]. The white light is redirected by a beam splitter; half the light towards the reference and half towards the sample. Subsequently, the reflections from both are redirected towards the CCD sensor. By scanning a range of heights, a surface profile of the sample is acquired. **(b)** Schematic close-up of a Mirau WLI, by Blunt [174]. It shows how the beam splitter divides the light between the reference and the sample. **(c)** Illustration by Bruker Nano Surfaces [176]. The addition of interference patterns of red, yellow, green and blue light results in an interference pattern with short coherence length. **(d)** Illustration based on [177], showing how the interference pattern looks when the WLI is focused on the high part of a step.

making reliable predictions on how the membrane deflection will change if the membrane size and heater geometry are changed.

Spatial sample drift

Spatial sample drift depends on many circumstantial factors such as the inherent drift of the TEM, the design and materials of the MEMS holder, the interface to the MEMS device, and the power consumption of the Microheater. Only the last is directly related to the MEMS device and only a part of it will result in drift; the heat that is transferred to the substrate of the MEMS and the MEMS holder through conduction (illustrated in figure 3.3) causes thermal expansion of these components. Therefore, characterization of how sample drift depends on power consumption is hard to determine and would require a large number of *in-situ* experiments to obtain reliable statistics. However, the correlation between drift and power consumption is evident (see subsection 2.1.3). Their relation will not be determined in this project. Instead, because the correlation is there, the focus will be on power consumption.

The heating setup logs the electric current, applied voltage and resistance over the four-point-probe. To characterize how power consumption (and thus the related drift) depends on the applied stimuli, the Nanoreactor will be assembled in the TEM holder, inserted in a ultra high vacuum pump, and connected to the gas supply system.

To make an accurate model in which the power consumption matches with the set temperature and gas type, many parameters are involved: thermal material properties of the different membrane layers, thermal properties of the gases, thickness of the gas layer (due to membrane deflection), and electrical properties of the Microheater. Because the Nanoreactor operates in a large temperature range (20–1000 °C), the temperature dependence of all these properties needs to be identified. Subsection 3.2.3 has been devoted to building a thermal model.

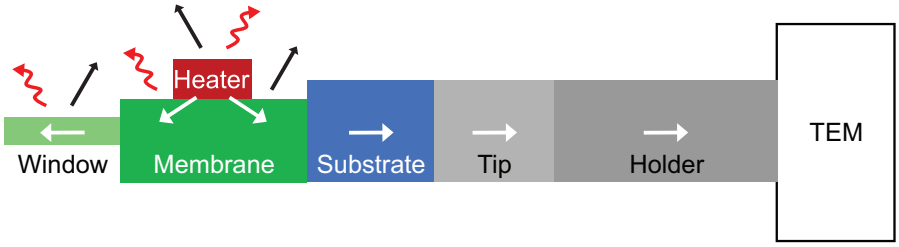

Figure 3.3: Illustration based on the work of Erdamar *et al.* [6]. Schematic figure of the components which the conducted heat passes from the Microheater to the frame of the TEM. The components are associated with thermal resistances. Spatial sample drift is caused by thermal expansion due to the slow thermal settling of the substrate, tip and holder.

3.2.2. Gas flow speed

The experimental setup that complements the Nanoreactor (the gas supply system, MEMS holder and the tubings in between, shown before in figure 1.1) allows for accurate pressure control at the the ends of the tubing. By symmetry, it allows for accurate pressure control at the center of the Nanoreactor, but it does not allow to define the pressure at the inlet and outlet of the chip itself. As a result, various corrections would be required to account for the flow resistance of tubings and valves. Moreover, the current geometry of the holder tip allows for some gas to pass through a few sidetracks. Therefore, the relation between pressure gradient and flowrate cannot be measured. However, there is little necessity for determining this relationship because of two reasons: it does not really matter what the exact pressure drop is as long as the pressure at the sample is defined, and the experimental results of nearly identical microchannels have already been reported by Harley *et al.* [147]. Their results can be used as a benchmark for finite element analysis on the geometry of the Nanoreactor. Moreover, equation 2.4 and 2.5 can be used to verify the order of magnitude for flow speed and flowrate.

The model will be used to simulate the gas flow inside the Nanoreactor. It follows from subsection 2.2.2 that the Nanoreactor operates in the laminar flow regime, which determines the types of physics that have to be implemented. The model should provide the gas velocity profile and the flowrate, which allow to determine the gas refreshing rate and the amount of gas that passes the region in which the sample is located. In addition to stationary flow, time dependent simulations will be done to determine gas flow settling time, and whether it is of any significance compared to overall system time scales. For reasons stated earlier in subsection 3.1.1, the gas flow model will be limited to nitrogen and helium at 1 bar (inlet a bit higher, outlet a bit lower).

In subsection 2.2.4 it has been shown that gas properties highly depend on the temperature. Therefore, it can be expected that temperature will affect the gas flow and visa versa. The interdependence will be included in the thermal model of subsection 3.2.3.

3.2.3. Temperature and heat

To make a proper electro-thermal model, temperature dependent material and gas properties need to be taken into account. Characterization of thermal conductivity and thermal radiation are very important for the accuracy of the model, but do not directly contribute to the analysis methods. Therefore, they can be found in appendix A and C. Mechanics, gas flow and heat will come together in this subsection, and they are all interdependent. That means the model should also include these.

Homogeneity over the heater

Analyzing the thermal aspects of the Nanoreactor starts by having an accurate method to measure temperature on the microscale. The accuracy paragraph of subsection 2.1.3 mentions a few suitable temperature measurement methods with high accuracy and sufficient spatial resolution. As has been done before for the Nanoreactor [6, 8], Raman thermometry will be used. A schematic of the experimental setup is shown in figure 3.4a. To ensure accurate calibration, the Nanoreactor is placed in an ultra high vacuum chamber to mimic the TEM conditions. A sapphire window allows the Raman laser to pass. The technique is based on measuring the energy shift of inelastically scattered photons, shown in figure 3.4b. To what extent the energy shifts happen, depends on the energy gap between the energy levels which is characteristic for a material type, and also for its temperature. Both Stokes and anti-Stokes scattering can be used for thermometry purposes.

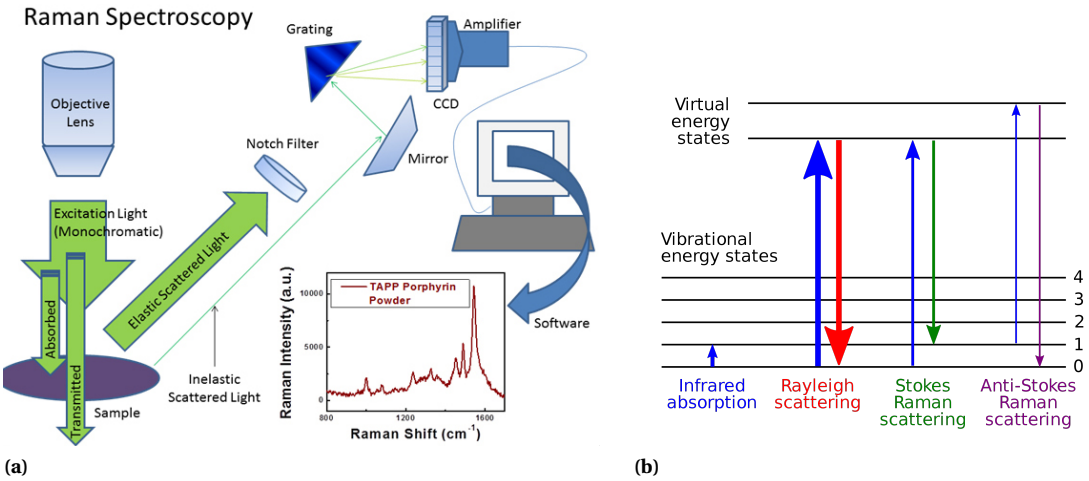

Figure 3.4: **(a)** Illustration by The Prashant Kamat Laboratory [184]. Schematic of a Raman spectroscopy/thermometry setup. The monochromatic laser light scatters, mostly elastically (Rayleigh scattering) and occasionally inelastically (Stokes or anti-Stokes scattering). The inelastically scattered light is red or blue shifted. The shifts determine the Raman fingerprint which is characteristic for the material type (in the case of spectroscopy) or the temperature (in the case of thermometry). **(b)** Illustration by Moxfyre [185]. The different scattering types are depicted in a phonon energy state diagram. In elastic scattering the incoming photon is emitted again with the same energy. In inelastic scattering the emitted photon has less (red shift) or more (blue shift) energy than the incoming photon

In Stokes scattering, some of the photon's energy is transfered to the material and some is emitted as a lower energy photon. The energy transfered to the material manifests itself as a lattice vibration. In elementary particle physics, a lattice vibration is described by a phonon occupying a certain vibrational energy state. The energy distribution of phonons in a material is described by Bose-Einstein statistics [120, 155]. Figure 3.4b shows how the phonon distribution is temperature dependent; a phonon can be promoted to a higher energy state by infrared absorption. Alternatively, as is the case in Stokes scattering, the phonon is created from part of the energy of the photon. As the bonds between atoms weaken due to thermal expansion at elevated temperature, the energy gap between energy states becomes smaller [120]. As a results, the energy (and thus the frequency) of the Stokes-scattered photons increase such that the red shift becomes less. This change in red shift is a commonly used method to measure temperature [178]. Silicon is a very suitable material because the intensity of the Raman Stokes peak is relatively high, and because the red shift is very linear with temperature, above room temperature [75, 179–181]. The temperature can be calculated from the Raman peak shift using

$$T = T_{\text{ambient}} - \frac{\omega_{\text{ambient}} - \omega}{C_{\text{Stokes}}} \tag{3.1}$$

in which T is the temperature, ω is the peak position in cm^{-1}, and C_{Stokes} is the material dependent relation between peak shift and temperature in $\text{cm}^{-1}\,^{\circ}\text{C}^{-1}$ [181].

Anti-Stokes scattering is based on the same principle, but it requires a phonon in the higher energy state. The occupancy of this state depends directly on the temperature [182]. The ratio between Stokes and anti-Stokes scattering is a direct measure for the temperature [183], but the anti-Stokes signal is very weak at low temperatures which causes inaccuracy due to poor signal to noise ratio [178]. Therefore, the peak shift of Stokes scattering is the more commonly used method, which will also be used in this study. The Stokes peak will be obtained from dropcasted silicon particles on the Microheater.

Raman thermometry will be used to determine the relation between temperature, electric resistance and power consumption. To isolate variables, an intermediate analysis will be done for the bottom chip only. Without heat losses through gas, only conduction through the membrane and thermal radiation are present, and the model simplifies in dimensionality. Radiation will be modeled by the Stefan-Boltzmann law. The emissivity will be determined using an infrared camera (see appendix A). The remaining heat losses happen through conduction. The thermal conductivity material properties of the model are based on literature and carefully scaled to find agreement between the finite element model and the experimental relation between temperature and power consumption. The temperature and resistance are matched by adjusting the TCR value in the model. The resulting temperature distribution in the finite element model should agree with the experimental results from Raman thermometry.

The thermal model on the bottom chip in vacuum is extended by adding a gas layer and top chip, completing the Nanoreactor. As continuum behavior can be assumed according to the theory in subsection 2.2.2 and 2.2.4, the gas properties can be obtained reliably from literature. The finite element model should provide the temperature distribution on the bottom chip in the Nanoreactor.

Homogeneity over the gas layer and top chip
As the gas layer and top chip have already been included in the thermal model, it will allow to extract the temperature distribution in the gas layer. To confirm the results of the model, Raman thermometry will be used on silicon particles dropcasted on top of an assembled Nanoreactor to measure the temperature distribution of the top chip membrane. To study the effect of gas flow on the temperature distribution, both the model and the Raman experiment will need to be performed for static gas conditions and high flow rates.

Although the experimental conditions used in the characterization are intended to mimic the TEM conditions, an experiment will be done inside the TEM to verify the obtained model. A sample is needed with a well-observable transition at a consistent temperature, preferably in the middle of the operating range of the Nanoreactor; between 300–700 °C. For this purpose Au-Ge nanowires will be deposited on both the bottom and top chip. Depending on their diameter, these have an eutectic melting point around 350 °C, as reported by Adhikari *et al.* [186]. To account for potential inaccuracies in absolute temperature a relative measurement will be done. First, the TEM will be focused on a nanowire on the bottom chip to record the transition temperature. Second, the TEM will be focused on a nanowire on the top chip. If the transition happens, the temperature of the top chip is known. The temperature difference between the bottom and top chip should be in agreement with the thermal model. If so, it confirms that the developed model is applicable to *in-situ* TEM experiments. (The results of this experiment can be found in appendix B.)

Membrane deflection as function of temperature
As temperature induces thermal expansion, it can be expected that membrane deflection will also depend on temperature. WLI will be used to measure membrane deflection as function of temperature for different gas pressures. Unfortunately the WLI cannot be used in combination with the ultra high vacuum chamber. The sapphire window influences the optical path, which impairs the interference of light. For the bottom chip, the temperature error should not be too large, because the four-point-probe will regulate the power to achieve the set temperature. The deflection of the top chip cannot be considered reliable as no closed-loop feedback will compensate for the additional heat losses to the ambient air. Although these experiments will not provide accurate results, it will provide an order of magnitude estimate on the effect of temperature, which will be sufficient to identify to what extent minimizing the hot area helps to reduce deflection.

Temperature settling and stability
The static electro-thermo-mechanical finite element model can easily be extended to include time dependency by defining initial conditions and setting a voltage that will lead to a certain temperature. The challenge is in measuring these aspects. Settling time and ramping rates can be measured by the Climate heating setup itself. This one, however, has been optimized for high temperature stability. Therefore, it will not be able to extract the maximum performance of the Nanoreactor regarding settling time. To measure the settling time, the experimental setup shown in figure 3.5 will be used. It connects a voltage supply to the heating probes and an oscilloscope to the sensing probes of the heater. The voltage supply has to apply a block wave. The oscilloscope will measure the part of the voltage that falls over the heating spiral, but this voltage will increase and settle over time as the temperature, and thus the resistance, of the heating spiral increases.

Temperature stability is very high for stationary conditions; 0.01 °C at any temperature. To measure the stability under dynamic conditions a gas switching experiment will be done. Switching from nitrogen to helium will greatly influence the required power to maintain the same temperature, so larger fluctuations in temperature can be expected.

Temperature accuracy for different gases
As known from subsection 2.1.3, the four-point-probe enables closed-loop feedback temperature control. It does this by measuring the resistance over the Microheater. This method is very accurate as long as the temperature distribution remains unchanged. However, the temperature distribution is affected by the presence

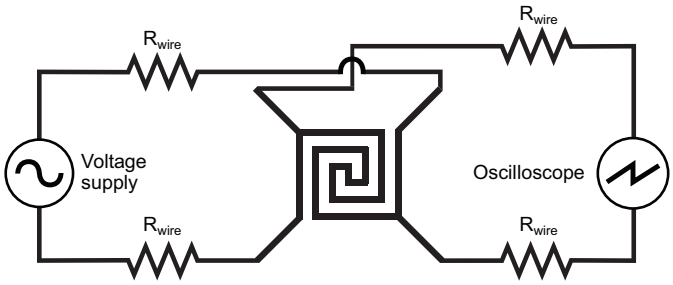

Figure 3.5: Diagram of the electric circuit to measure the settling time of the Nanoreactor. The heating lines are connected to a voltage supply that provides a block wave. The sensing lines are connected to an oscilloscope which reads out the voltage and determines the settling time. For time synchronization, the voltage supply is also connected to the oscilloscope (not shown).

of gas, which means that the resistance to temperature relation will be affected by different gas conditions. The electro-thermal model developed for homogeneity purposes already includes how the resistance changes over the heating wire. Therefore, the model will provide an estimate of the induced error from using different gas environments. Depending on the significance, it can be experimentally verified using Raman thermometry by measuring the temperature of the same silicon particle inside the Nanoreactor with different gas types.

3.2.4. Gas switching time

To measure the gas switching time, the gas composition should be known as function of time. Ideally the gas composition is measured locally inside the Nanoreactor. Alternatively, the composition of the gas leaving the Nanoreactor could be analyzed by a mass spectrometer, a method that is suitable for analyzing small gas volumes [187]. The disadvantage of analyzing the outflowing gas is that it does not provide direct information on the gas composition in the region where the sample is and introduces a time-delay due to the length of the tubing. On the other hand, it was mentioned before in subsection 2.1.1 that Microheaters have been used with regards to gas sensing and mass flow meters [21]. The principle behind it is that power consumption changes as function of gas composition and flow speed. The gas sensor, in this case the Microheater, is already present in the Nanoreactor.

To turn the Nanoreactor into a gas composition sensor it has to be known how the power consumption varies as function of the gas composition, but also as function of other variables to identify interdependencies. These variables include gas composition, temperature, pressure, and flow rate. Ideally, operating conditions are found in which the power consumption is the most sensitive to gas composition changes and the least sensitive to other variables. The first part will be to determine the dependency of power consumption on the aforesaid variables. Then, the optimal conditions will be set and the gas supply system will be programmed to supply 100 % of nitrogen and abruptly switch to supply 100 % helium. Considering the power consumption as function of gas composition is known, the temporal change in power consumption is directly correlated to the temporal change in gas composition inside the Nanoreactor.

The gas switching speed will be limited by the dead volume of the Nanoreactor and the gas supply system itself. Inside the Nanoreactor, the gas switching behavior will follow the theory as explained in subsection 2.2.5. The gas flow profile speed in the Nanoreactor will be known from 3.2.2, binary gas diffusion coefficients can be found in literature (see appendix A) and their dependence on temperature and pressure is given by equation 2.21. This information will be included in the finite element model to determine the gas switching time as well as which gas switching mechanism is dominant in which region.

3.3. Optimization

3.3.1. Mechanical stability

Two of the optimization targets are part of the mechanical stability category; membrane deflection and spatial sample drift. Both should be minimized, especially their dependence on changing stimuli.

Membrane deflection
Based on the theory, characterization through WLI and finite element analysis, it will follow how far the membrane should shrink to meet the target. The developed finite element model will be used to determine the membrane deflection as function of pressure. As nothing changes on the materials or their properties, but only the design, the model will remain accurate. The membrane size will be reduced in steps of 50 µm starting from 600, until the the membrane deflection reaches below the target of 10 µm at 1 bar pressure. Care has to be taken that shrinking the membrane causes higher power consumption. To counteract, the optimized heater should also be smaller and more efficient.

Spatial sample drift
The goal is to decrease power consumption by 10 %, but ideally it should be reduced as far as possible. The heater will be redesigned to be smaller and the electrical probes will be optimized, as the metal is responsible for a significant part of the conductive heat loss. Simulations will be run to identify the significance of heat loss mechanisms and minimize them. In this optimization, the heat loss through radiation is of no concern, as it does not directly affect drift. Moreover, it will be identified how the membrane size and gas layer thickness influence power consumption such that an optimum can be found.

3.3.2. Gas flow speed

From the characterization it will become clear how the spacers affect the local gas flow speed. To ensure that as much gas as possible will pass the sample, the spacers should block the flow paths next to the membrane and guide the gas towards where it matters; in the Microheater region. The finite element model will be used to determine how much gas passes the membrane and how much slips by. Iterations of optimized spacers will be modeled using finite element analysis, until the desired result is obtained or the improvements become too marginal. Then, the effect on time dependent aspects such as temperature and flow speed settling time should be simulated to ensure these are not unintentionally affected.

3.3.3. Temperature and heat

As only the design is being changed, the characterized material properties and developed model still apply. Therefore, any design change can directly be simulated. The thermal optimization of the Nanoreactor will completely go via finite element analysis. The optimization will be performed according to the design guidelines and within the design constraints. No optimization will be dedicated to membrane deflection as function of temperature. Due to the nature of the phenomenon, not much can be done besides reducing the hot area. Moreover, the experimental results obtained during characterization are inaccurate, which means it cannot be assumed that this aspect of the model is entirely correct.

Homogeneity over the heater
The major tool to improve homogeneity will be varying linewidth of the heater. An example is shown in figure 3.6a. The alternative, varying heater pitch, is undesired as this will require relatively large spacing in between the heater lines in the center of the Microheater. These large regions will lose heat through thermal radiation, which causes local temperature variations. Having wider heater lines omits this problem; the metal is a good thermal conductor which facilitates the spread of heat and enhances the homogeneity even further. The finite element model will be used to find where heat losses are largest. The varying heater linewidth will be modified such that Joule heating counteracts heat losses or metal will be added to spread the heat. The most important pitfall is the increase in current density in the thinnest heating wires, which accelerates electromigration. To avoid that, the heater will be reduced in size such that less power and current are required. Furthermore, the structure of the electrical probes will be optimized to reduce the heat conduction, without increasing the power dissipation in them significantly. A large step can be made by minimizing the width of the sensing probe lines, because the current passing through is negligible.

Homogeneity over the gas layer and top chip
Ideally, the temperature remains homogeneous over the thickness of the gas layer. If so, the sample will also have a constant temperature over its thickness. The finite element model will be used to determine which heat loss mechanism is dominating and if the homogeneity can be improved. If the top chip membrane acts

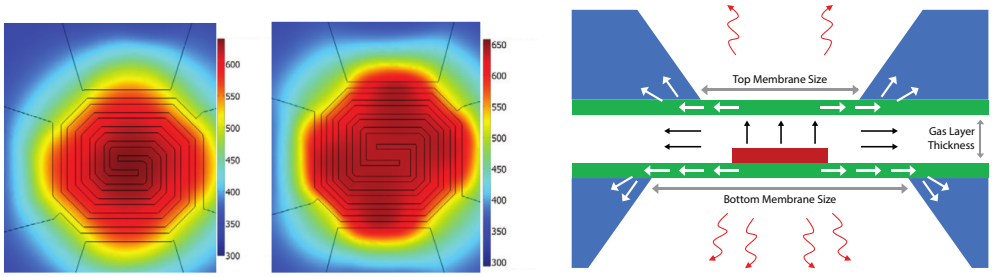

Figure 3.6: (a) Simulation result by Mele *et al.* [56]. The high-temperature region (in red) is much much larger in the design using varying linewidth. **(b)** Simplified cross-sectional schematic of the Nanoreactor showing potential heat loss mechanisms. The substrate is shown in blue, insulating layer(s) in green and the Microheater area in dark red. Conduction through the membrane is indicated by white arrows, conduction through air by black arrows and emission of thermal radiation by curly red arrows.

as a significant heat sink, the gas layer thickness should be larger, but if the thermal conduction through the gas dominates it is beneficial to minimize thickness. If both are significant, it may not matter that much for homogeneity, but it will matter for power consumption. Due to the dimensional aspect ratios, it is expected that both are significant: the gas layer is ~50 times as thick, but its thermal conductivity is ~50 times as low (for nitrogen). That means the lateral thermal conduction of the top membrane and the gas layer are comparable and, moreover, it means that the vertical thermal resistance will be much smaller than the lateral such that the top chip membrane will become nearly as hot as the Microheater. The model will be used to make this trade-off quantitative. A schematic of the relevant heat loss mechanisms is shown in figure 3.6b.

Temperature settling and stability

The settling time of the optimized Nanoreactor can be predicted from the finite element model. Improving temperature stability is more complicated. It depends on the relative change of resistance to temperature,

$$\text{Temperature measurement sensitivity} = \frac{\partial R/\partial T}{R}. \tag{3.2}$$

The sensitivity of the sensing probes to temperature changes should be increased. That would allow the controller to detect and respond faster. A higher sensitivity could be achieved by connecting the sensing probes closer to the center of the heating spiral. Because the probed area is hotter and more homogeneous, the sensitivity does not average with the colder areas in which the resistance changes are less profound. A disadvantage of connecting the sensing probes closer to the center is that an additional heat path is added between the hot and cold region with relatively low thermal resistance. To what extent this will increase power consumption, will follow from the finite element model.

Temperature accuracy for different gases

The necessity of this optimization will be determined by modeling the effect of vacuum, nitrogen and helium on the relation between resistance and temperature. Differences in these relations, due to changes in the temperature distribution, can best be omitted by measuring the temperature as close to the center of the Microheater as possible. The same optimization method should be used as in optimizing the sensitivity to temperature changes.

3.3.4. Gas switching time

To improve gas switching time, the spacers will have to be redesigned to guide the gas from the inlet in the direction of the heater and from there to the outlet. As discussed before in subsection 2.2.2, the current spacers cause that there is nearly no gas flow in the outer regions of the Nanoreactor. To ensure fast gas switching, advection must be present in every domain, which effectively means that $\text{Pe}_{\text{mass}} > 1$ (equation 2.18). To achieve this, the finite element model will be programmed to calculate Péclet from the local gas flow speed using a characteristic length of 1 mm. The spacer design will be modified to guide the gas towards low Péclet areas until the target is reached.

4

Results of experimental characterization and finite element modeling

4.1. Characterization

4.1.1. Mechanical stability

Membrane deflection

The bottom and top chip membranes have been measured using a SEM. The membrane sizes were found to be 830 and 427 µm respectively, as shown in figure 4.1.

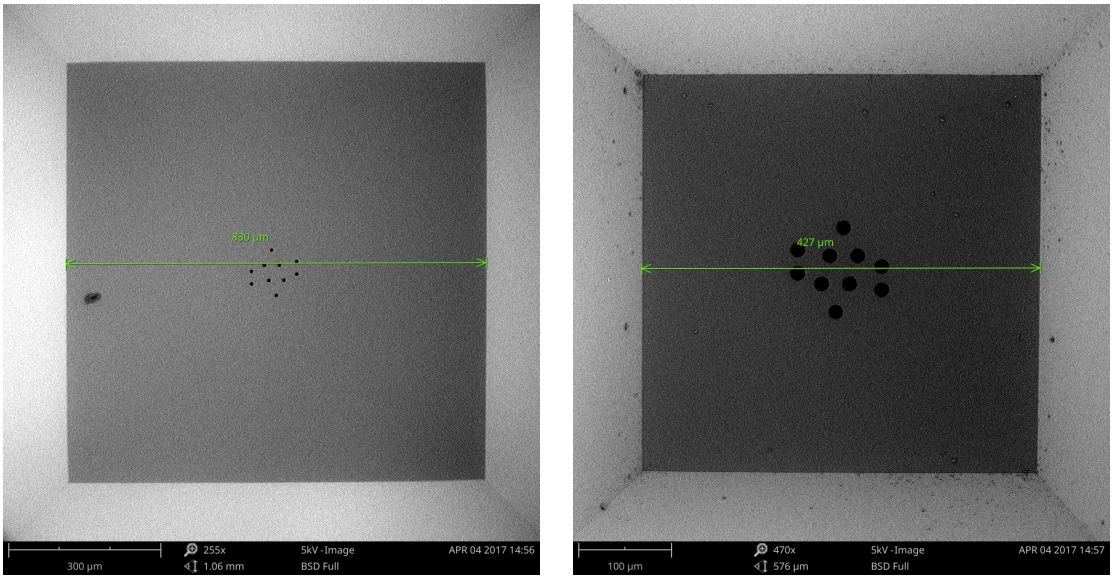

(a) Bottom membrane

(b) Top membrane

Figure 4.1: SEM images of the Nanoreactor. The membrane edge length is **(a)** 830 µm for the bottom, and **(b)** 427 µm for the top.

The same bottom and top chip were used to measure membrane deflection as function of pressure using the WLI setup described in subsection 3.2.1. Examples of the measurement results are shown for the bottom chip at 506 mbar in figure 4.2a and the top chip at 996 mbar in figure 4.2b. To correct for planar tilt, the absolute membrane deflection was found by averaging the height difference between one corner and the center, and the opposite corner and the center. The measurements were repeated in steps of 50 mbar for the bottom chip and 100 mbar for the top chip. The results are plotted in figure 4.2c and 4.2d. The errorbars shown were determined through a statical analysis of which details are provided in appendix D.

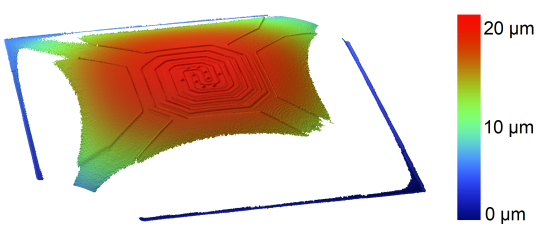

(a) Bottom membrane at 506 mbar

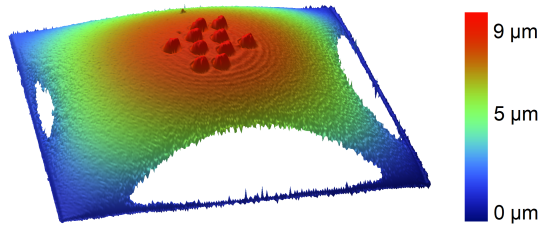

(b) Top membrane at 966 mbar

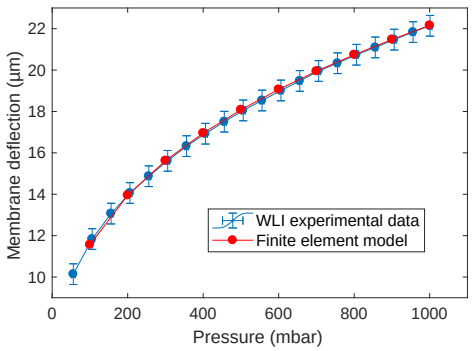

(c) Bottom membrane deflection

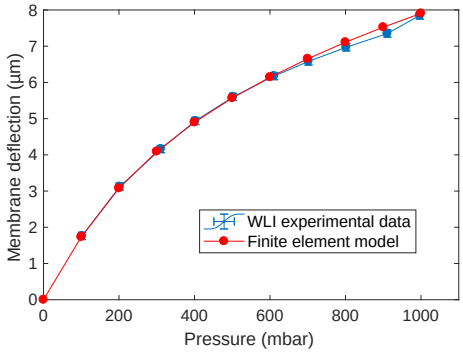

(d) Top membrane deflection

Figure 4.2: WLI result of **(a)** bottom and **(b)** top chip membrane deflection at 506 mbar and 966 mbar overpressure, respectively. If the slope gets too high, the WLI is not able to image them properly anymore, resulting in the missing part of the profile at the edges of the membranes. **(c)** Bottom chip (corrected for 2.4 µm initial deflection) and **(d)** top chip membrane deflection as function of pressure, measured using WLI and simulated with finite element analysis. The error bars are depicting two standard deviations (see appendix D).

The dimensions as measured by the SEM have been implemented in the finite element model. The model was set up to calculate the membrane deflection as function of pressure in steps of 100 mbar. The results are plotted together with the experimental results in figure 4.2c and 4.2d. The most important factors that determine the agreement between the model and experimental data were the mechanical material properties, as predicted by equation 2.6. Very good agreement was found for the top chip, but for the bottom chip an offset of 2.4 µm was found which could not be explained by the elastic properties of the membrane. As the shape of the deflection profile exactly matched the simulations, it appears the offset originates from initial deflection. Calculations on arc length of the deflected membrane showed that an offset as much as 2.4 µm could be explained by an additional arc length of only 18.5 nm. Considering the fact that the membrane does not appear entirely flat upon inspection with the optical microscope (in comparison, the top chip does), the additional arc length explains the offset. Details on the arc length calculation can be found in appendix A.

The deflection curves, as shown in figure 4.2c and 4.2d, show good resemblance to the analytical models that were found in literature. Figure 2.10b predicts about 18 µm deflection for the bottom and 7 µm for the top membrane. Considering that the membranes in the experiment and finite element analysis are a few tens of micrometers larger, and the bottom membrane has an offset, the results agree to within 1 and 0.5 µm for the bottom and top membrane respectively.

Spatial sample drift

Figure 4.3 shows the power consumption as function of pressure for three different experimental conditions; vacuum, nitrogen and helium. The curve for the bottom chip in vacuum has been used, together with the electrical resistance as function of temperature, to determine the thermal material properties which were essential for developing the thermal model. For the other two curves, the assembled Nanoreactor was operated both with 1 bar nitrogen and 1 bar helium, respectively. It becomes clear that the gas layer and the top chip have a major impact on the power consumption, resulting in significantly higher drift when gases are used.

The thermal model of the bottom chip, which is elaborated on in subsection 4.1.3, was extended with the gas layer and top chip. Figure 4.3 shows that the finite element model agrees closely with the experimental power consumption values for vacuum and nitrogen. For helium, a small discrepancy is found that increases with

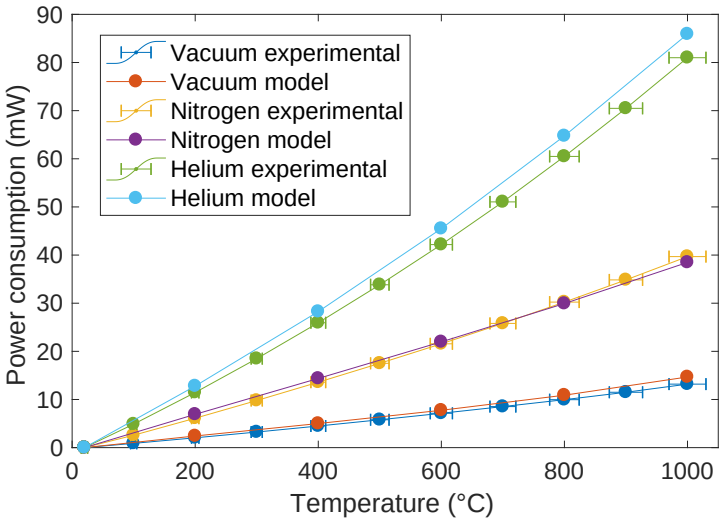

Figure 4.3: Power consumption as function of temperature for the bottom chip in vacuum, and for the assembled Nanoreactor with 1 bar nitrogen or helium inside, measured in a high vacuum conditions and modeled using finite element analysis. The power consumption error bars are not shown as they are too small; less than 0.02 mW.

temperature. The disagreement can be explained by the relatively high mean free path of helium (~193 nm at room temperature and atmospheric pressure), which becomes close to a micrometer at 1000 °C according to subsection 2.2.4. This means that gas flow is not purely laminar anymore (Kn ≈ 0.03), which results in a lower thermal conductivity and thus in lower power consumption. Another source of inaccuracy is the membrane deflection as function of temperature that affects the heat path due to additional membrane deflection (subsection 3.2.3). The large differences in power consumption between nitrogen and helium relate to their factor 10 difference in thermal conductivity.

4.1.2. Gas flow speed

Harley *et al.* have reported gas flow speeds for comparable microchannel geometries (approximate dimensions: width 90 µm, length 10.9 mm, and height 11 µm), but for in- and outlet pressure gradients from 1 bar and higher. For these conditions, the gas flow speed in the center of the channel was approximately 7 $m s^{-1}$ for nitrogen. For the case of the simplified Nanoreactor as shown in figure 2.9a, the pressure difference is 10 times less, the channel height is 2 times less, and the length is 2 times less. Using equation 2.4, a gas flow speed of approximately 20 times less would be expected for the Nanoreactor; 0.35 $m s^{-1}$.

The finite element model shown in figure 4.4a includes the complete gas domain within the O-ring sealing. Through simulations, a gas flow speed of 0.44 $m s^{-1}$ is found, which agrees with the rough estimate based on literature. It could have been expected that the actual gas flow speed was higher than the estimate, as the simplified geometry overestimates the flow resistance of the Nanoreactor in the center where the gas flow channel is higher, due to membrane deflection, and wider, because there are no spacers. Figure 4.4 shows the gas flow of nitrogen in the Nanoreactor at a pressure of 1 bar. The model includes membrane deflection due to pressure and gas property changes as function of temperature. To show the gas flow speed in the inner and outer regions of the Nanoreactor as function of temperature, gas flow cross-sections have been plotted on a linear scale, logarithmic scale, at room temperature, and at 1000 °C. When comparing figures 4.4g and 4.4h it is clear that the temperature causes local gas expansion. As a result, the local gas flow speed is much higher to maintain the same mass flow rate, as shown in figure 4.4f relative to 4.4e.

The effect of another gas type, in this case helium compared to nitrogen, has a minor effect only. A few of the plots from figure 4.4 are duplicated for helium in figure 4.5. The slightly higher viscosity of helium results in minor differences in the flow profile. The effect of the large differences in thermal properties between helium and nitrogen is hardly pronounced in gas flow differences and can be considered negligible for the practical purpose of the Nanoreactor.

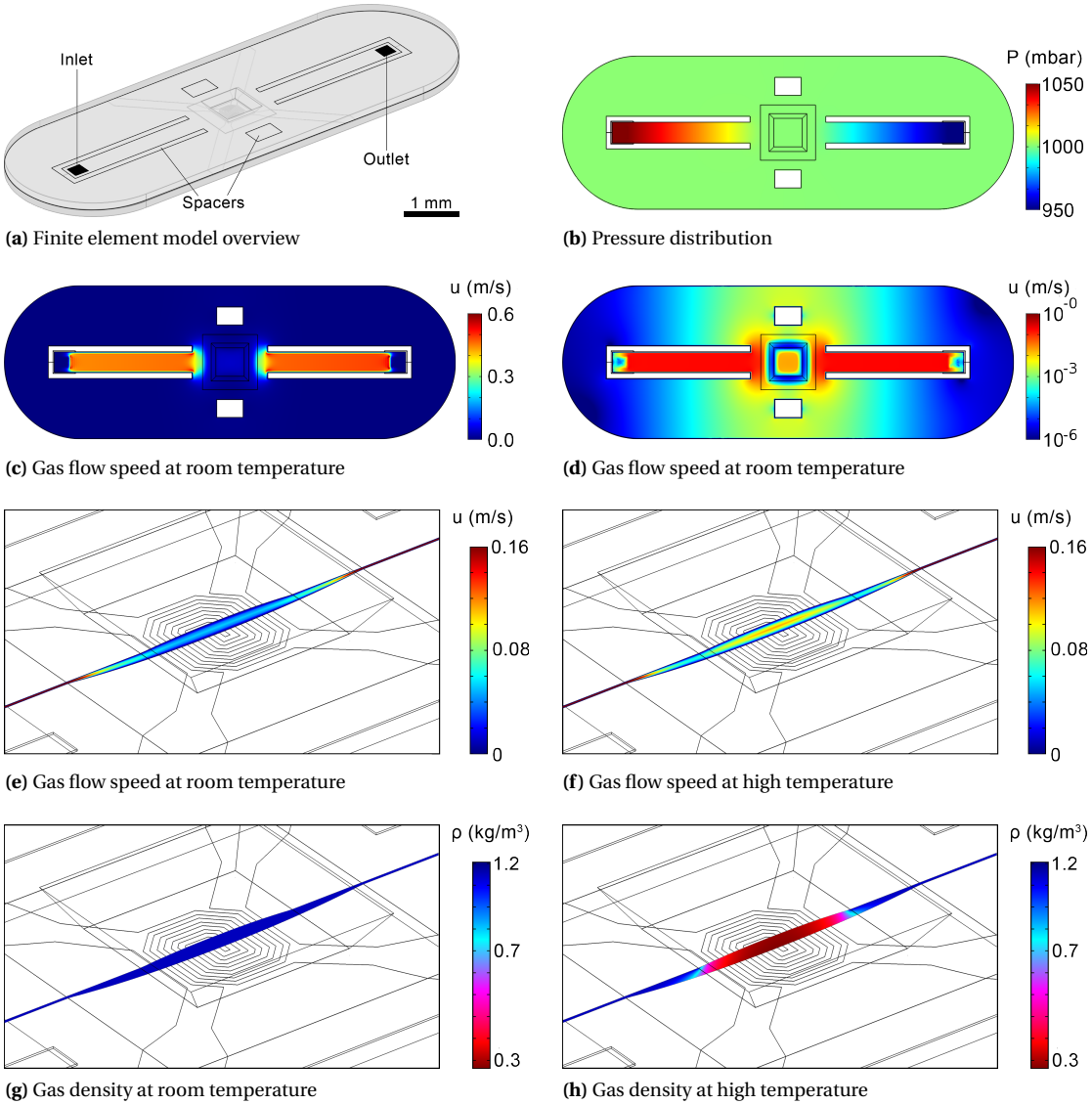

(a) Finite element model overview

(b) Pressure distribution

(c) Gas flow speed at room temperature

(d) Gas flow speed at room temperature

(e) Gas flow speed at room temperature

(f) Gas flow speed at high temperature

(g) Gas density at room temperature

(h) Gas density at high temperature

Figure 4.4: Nanoreactor finite element model with nitrogen gas. The gas flow direction is from left to right. **(a)** A schematic of the model. **(b)** Gas pressure distribution. **(c,d)** Gas flow speed over the gas volume plotted on a linear and logarithmic scale. **(e,f)** Close-up of gas flow in the Microheater region at room temperature and 1000 °C. **(g,f)** Gas density at room temperature and 1000 °C.

A time dependent study has been done to determine gas flow settling time. The gas flow rate at the inlet is a good measure for this, as it directly depends on the pressure distribution and local gas flow speeds. For an in- and outlet pressure of 1050 mbar and 950 mbar, and 1000 mbar as the initial Nanoreactor pressure, the settling time is found to be only 0.11 ms. Details can be found in appendix C.

4.1.3. Temperature and Heat

Homogeneity over the heater

The temperature homogeneity has been measured over the bottom chip in vacuum conditions using Raman thermometry. The results are shown in figure 4.6. The temperature was found by measuring the peak shift as function of temperature on dropcasted silicon particles. As is common practice, the peak position was found by fitting a Lorentzian function through the data spectrum [188], and converted in temperature using equation 3.1. Literature provides C_{Stokes} values ranging from 0.0221–0.0233 $\text{cm}^{-1}\,^{\circ}\text{C}^{-1}$ [75, 181]. As this range would result in a potential 5 % error, a calibration of the silicon particles was done with a hotstage and the Raman setup. This provided $C_{\text{Stokes}} = 0.0227$ with an estimated error of less than 1 %, which fits well within the range reported in literature.

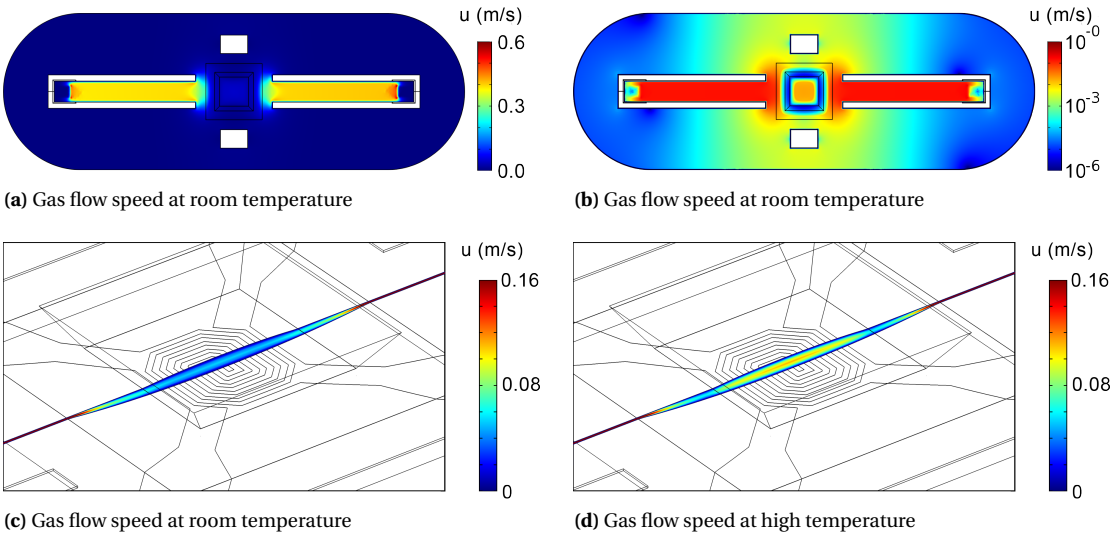

(a) Gas flow speed at room temperature

(b) Gas flow speed at room temperature

(c) Gas flow speed at room temperature

(d) Gas flow speed at high temperature

Figure 4.5: Nanoreactor cross-sections showing helium gas flow speed. The gas flow direction is from left to right. **(a)** Gas flow on a linear scale. To visualize the gas flow speed in the outer regions the same profile is plotted on logarithmic scales in **(b)**. The effect of temperature on the gas flow is shown by comparing **(c)** room temperature and **(d)** 1000 °C.

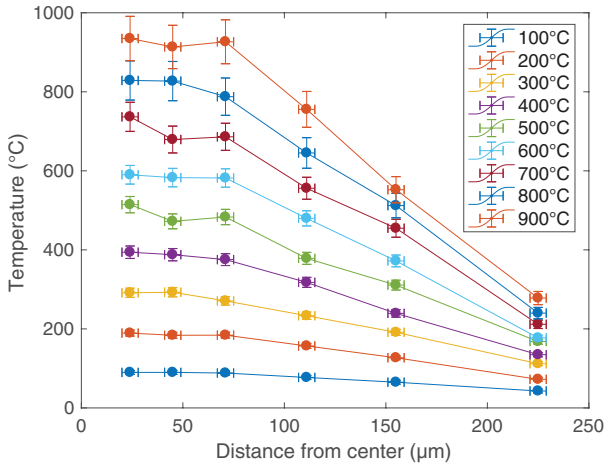

Figure 4.6: Temperature distribution over the bottom chip measured using Raman thermometry in vacuum. Each curve represents the temperature as function of distance from the center of the Microheater for different set temperatures.

Figure 4.6 shows the homogeneous region extends to a circle with a radius of 70 µm. Outside of that, the temperature drops rapidly. The electron transparent windows, shown in figure 2.8c, are positioned within a 55 µm radius from the center of the heater. The experimental uncertainties are low enough to provide clear trends, but are too large to determine the temperature gradients within the homogeneous circle (uncertainty analysis can be found in appendix D). Higher accuracy could be obtained by thorough calibration and more statistics, but the clear trends allow for accurate finite element analysis regarding temperature distributions. As in the end the optimized design will be based on models, the latter option is more favorable.

An example of the temperature distribution at 1000 °C, including a close-up of the temperature distribution in the electron transparent window area, is shown in figure 4.7. It was found that the region in which the electron transparent windows fit, has a 95.5 % homogeneity, which is defined as the ratio between the window at the lowest and highest temperature in °C. The homogeneity was determined for various temperatures, the results are shown in the second column of table 4.1.

The model was extended by including nitrogen and helium. The presence of gas has a significant effect on the temperature distribution as it introduces new heat conduction paths. Because thermal conductivity of helium is 10 times higher than of nitrogen, the type has a large effect on the shape of the profile. The higher

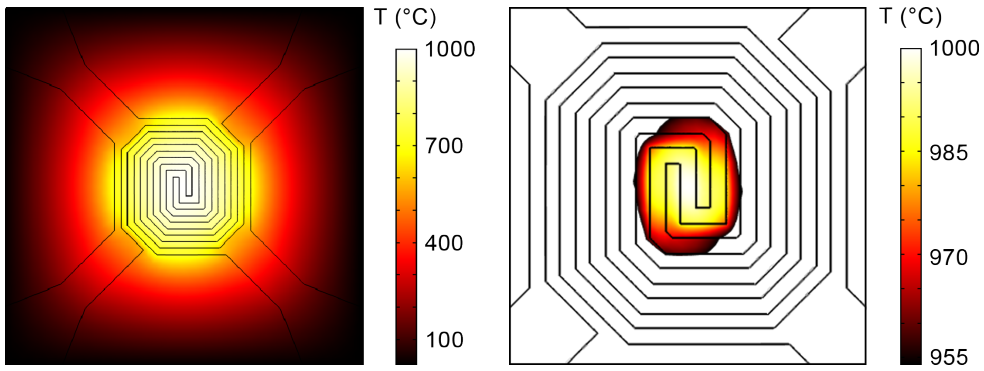

(a) Temperature distribution bottom membrane **(b)** Temperature distribution homogeneous area

Figure 4.7: Temperature homogeneity over the bottom chip at 1000 °C in vacuum, from finite element analysis. **(a)** Temperature distribution over the membrane. **(b)** The 95.5 % homogeneous electron transparent window area (location of windows is shown in figure 2.8c). To emphasize the shape and size, the temperature data outside of the homogeneous area is not shown.

Table 4.1: Temperature homogeneity over the electron transparent windows in vacuum, nitrogen and helium conditions at different temperatures. For the nitrogen and helium cases, homogeneity is provided for static and flow conditions at a pressure of 1 bar. The gas flow conditions were as in figure 4.4 and 4.5. The results are obtained through finite element analysis. Read-out error is below 0.1 %.

Temperature (°C)	**Homogeneity vacuum**	**Homogeneity nitrogen static**	**Homogeneity nitrogen flow**	**Homogeneity helium static**	**Homogeneity helium flow**
20	100 %	100 %	100 %	100 %	100 %
200	96.5 %	94.6 %	94.4 %	94.7 %	94.5 %
400	95.9 %	94.1 %	93.8 %	94.5 %	94.4 %
600	95.7 %	93.9 %	93.7 %	94.5 %	94.4 %
800	95.5 %	93.8 %	93.6 %	94.6 %	94.5 %
1000	95.5 %	93.9 %	93.7 %	94.7 %	94.7 %

thermal conductivity smoothens the temperature profile and effectively makes it more circular. As a result, the electron transparent windows experience a temperature which is closer to the set temperature, meaning a higher homogeneity is obtained with helium than with nitrogen. Examples are shown in figure 4.8 for both gases, static as well as with gas flow. In the gas flow conditions as analyzed in subsection 4.1.2, the homogeneity is slightly lower as the upstream windows get cooled a little by the incoming gas flow. The homogeneity typically goes down with increasing temperature as the gradient becomes steeper until 800 °C. Above that, the temperature dependent thermal conductivity of the gas as well as the radiative heat losses in the hottest regions start becoming significant, resulting in a small increase in homogeneity again. An overview of the results is given in table 4.1 for various temperatures.

Homogeneity over the gas layer and top chip

To ensure accurate temperature of the sample, the temperature of the surrounding gas is as important as the temperature of the bottom chip. Figure 4.9 shows the results that were obtained using the finite element model. The temperature distribution over the gas layer shows a relatively small temperature drop; the temperature 1 µm above the microheater is only 2 °C less. Therefore, the temperature homogeneity ensures a small temperature error of 0.2 % or less, even when large particles are used.

Similar to the analysis for the bottom chip, the temperature distribution is affected by the gas flow to a minor extent. As indicated in figure 4.9c and 4.9d, the temperature difference between the direction where the gas is coming from and going to is 6 °C, in the middle of the gas layer at a distance 100 µm from the center. The sample on the electron transparent windows would experience an even smaller discrepancy, as they are closer to the center and the Microheater. The effect of gas flow on the temperature homogeneity is small compared to the differences already present in static condition, despite the high gas flow speed of ~15 cm s^{-1}. This insignificance was already hypothesized in the theory of subsection 2.2.4; using the actual geometry, flow speed and thermal diffusivity in equation 2.17 gives $\mathrm{Pe}_{\mathrm{heat}} \approx 0.04$. This confirms that heat transfer is dominated by thermal conduction.

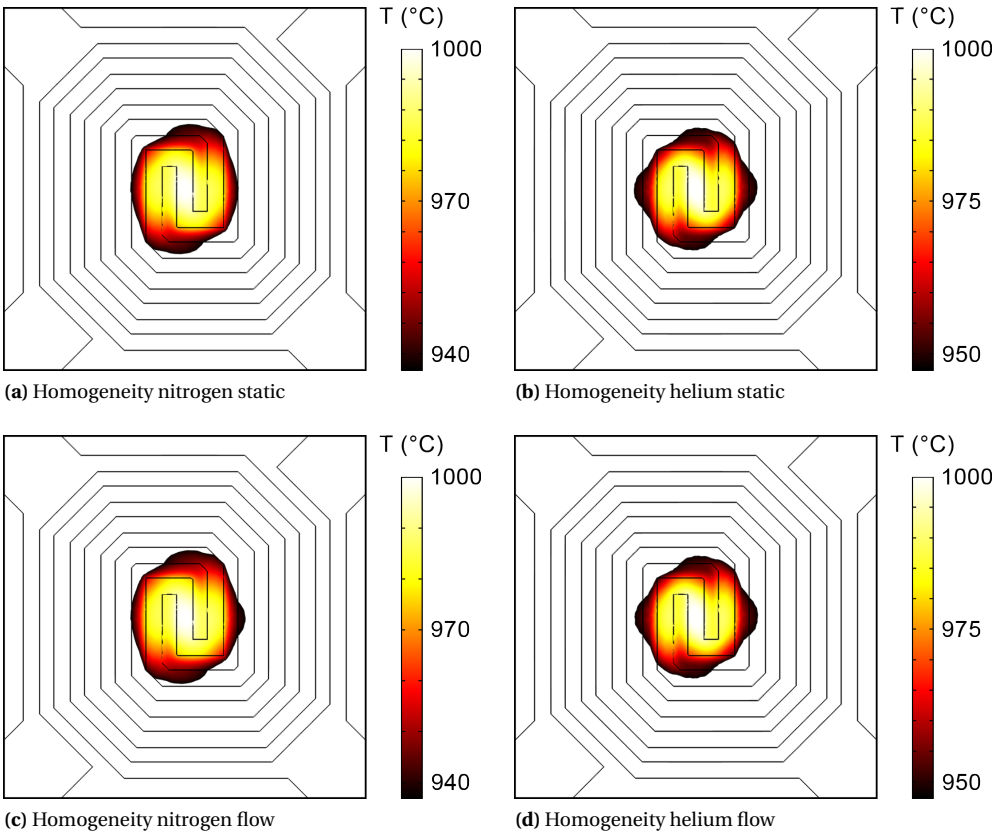

(a) Homogeneity nitrogen static

(b) Homogeneity helium static

(c) Homogeneity nitrogen flow

(d) Homogeneity helium flow

Figure 4.8: Finite element analysis to determine temperature homogeneity over the region with the electron transparent windows (for window location see figure 2.8c) of bottom chip at 1000 °C and 1 bar for **(a)** static nitrogen, **(b)** static helium, **(c)** nitrogen gas flow as shown in figure 4.4, and **(d)** helium gas flow as shown in figure 4.5. The gas flow direction is from left to right. The legends are adjusted to match the temperature distribution in the homogeneous region.

To provide evidence for the validity of the simulations, silicon particles were dropcasted on top of the top chip membrane to confirm the temperature distribution by Raman thermometry. The nanoreactor was assembled with static air inside at atmospheric pressure. Because of the proximity of air and nitrogen in thermal properties, the temperature differences between the experiment and model are expected to be smaller than the measurement accuracy. The top chip with silicon particles as well as the experimental results are shown in figure 4.10. Except for the two datapoints at 700 °C and 800 °C of the particle at a 82 µm distance, the experimental data confirms the distribution as found with simulations. To directly compare, the top chip temperature has been plotted as function of the bottom chip temperature in figure 4.11. The data was fitted by linear curves. The relations were found to be:

$$\begin{aligned} T_{\text{top,air}} &= 0.874\ T_{\text{bottom}} \\ T_{\text{top,nitrogen}} &= 0.911\ T_{\text{bottom}} \\ T_{\text{top,helium}} &= 0.955\ T_{\text{bottom}} \end{aligned} \tag{4.1}$$

The difference between nitrogen and helium directly comes from the higher thermal conductivity of helium, which facilitates a larger heat transport from the bottom to the top chip, resulting in a higher top chip temperature. The difference between the datapoints of air and nitrogen is still within the error margins, but the data fit-curve shows that the error is of a structural character. The most evident reason is that the temperature was not measured at the exact center of the top chip membrane, where it is hottest, but at a distance of 30 µm. According to the nitrogen gas model, this would account for a difference of 1.5 %. The remaining disagreement may be explained by the fact that membrane deflection as function of temperature was not taken into account. As will be shown in the next subsubsection, the membrane actually deflects a few additional micrometers at high temperature, which increases the heat path length resulting in a slightly lower top chip temperature (the effect of this has been discussed before regarding spatial sample drift in subsection 4.1.1).

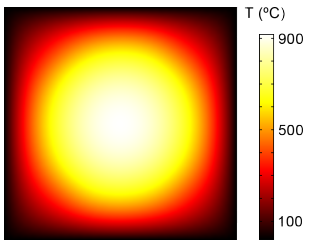

(a) Top membrane, nitrogen static

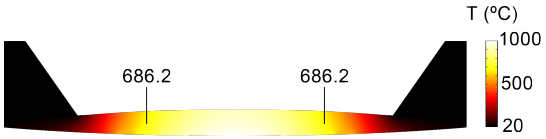

(b) Gas layer, nitrogen static

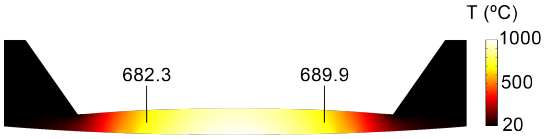

(c) Gas layer, nitrogen flow

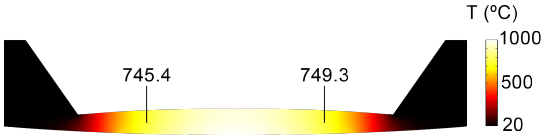

(d) Gas layer, helium flow

Figure 4.9: Finite element analysis on temperature distribution with the Microheater set to 1000 °C and gas pressure of 1 bar for the **(a)** top membrane with static nitrogen, **(b)** static nitrogen layer, **(c)** nitrogen layer with gas flow, and **(d)** helium with gas flow. The gas flow direction is from left to right.

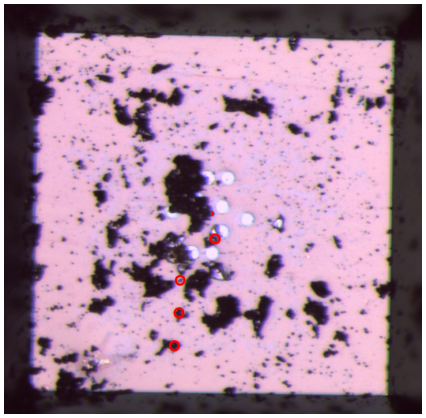

(a) Top chip with silicon particles

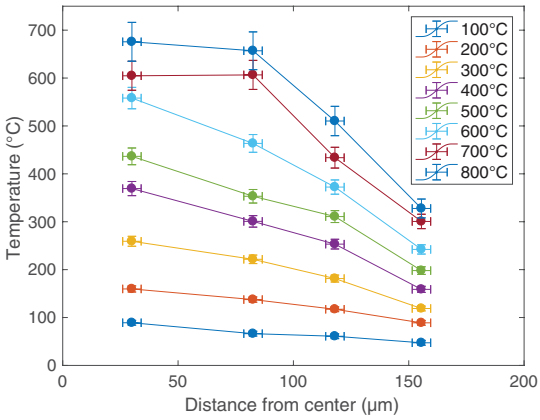

(b) Top membrane Raman thermometry results

Figure 4.10: **(a)** Optical microscope image of the Nanoreactor top chip with dropcasted silicon particles. The probed particles are indicated by a red circle. **(b)** Temperature distribution over the top chip measured using Raman thermometry, with air at atmospheric pressure inside the Nanoreactor.

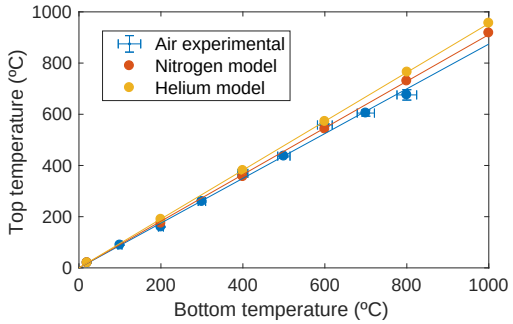

Figure 4.11: Top chip temperature as function of bottom chip temperature. The results for air (obtained with Raman thermometry) show good agreement to the simulation for nitrogen. The results for helium and the linear fit curves of equation 4.1 are also included.

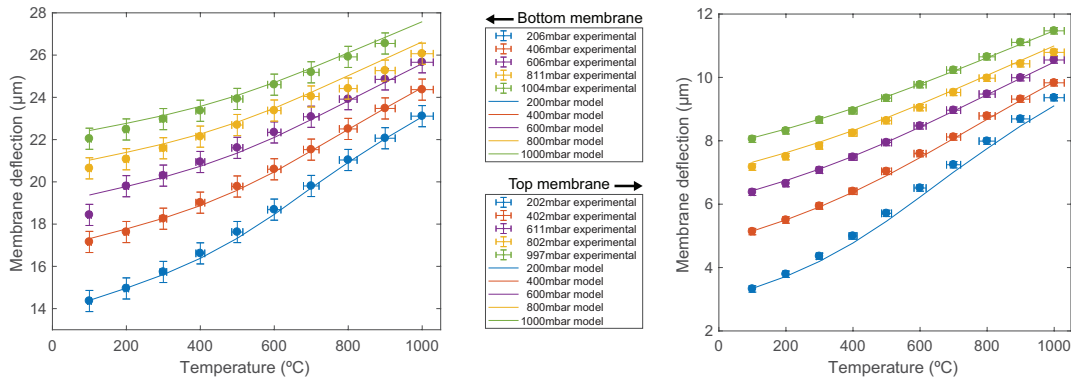

(a) Bottom membrane deflection **(b)** Legend **(c)** Top membrane deflection

Figure 4.12: Membrane deflection as function of temperature for different nitrogen pressures. The error bars are depicting two standard deviations (see appendix D). **(a)** Bottom membrane deflection measured with WLI and simulated using the finite element model. **(c)** Top membrane deflection measured with WLI and simulated using the finite element model.

Membrane deflection as function of temperature

Just as membrane deflection with pressure (subsection 4.1.1), membrane deflection with temperature is measured using WLI. As discussed in subsection 3.2.3, the experimental conditions were not representative for an *in-situ* TEM study. Therefore, these measurements are merely intended to give a good estimate on the order of magnitude of this effect. The agreement between experimental and simulation results is not as good as with the other characterized performance parameters, even with inclusion of temperature dependent coefficient of thermal expansion (obtained and tuned based on literature, see appendix A). The average mismatch is 251 nm for the bottom chip and 113 nm for the top chip. The experimental and simulation results are plotted in figure 4.12 for the bottom and top chip, for a few nitrogen gas pressures. It follows that temperature does have a significant effect on membrane deflection. It is more pronounced at low pressure, where the mechanical stress is relatively low and thermal stress is more significant. The results add reason to minimize the hot area, and thus the heater size.

Additionally, it was measured how gas flow rate affects temperature deflection. No measurable differences were observed over the range of 0–1 mL min^{-1} and beyond, which further verifies that the gas flow speed has a negligible effect on the temperature distribution over the gas layer. The results are shown in appendix B.

Temperature settling and stability

The experimental setup shown in figure 3.5 was used to measure temperature settling time (defined as the time to reach 90 % of the intended value). Settling time was found to be 12 ± 3 ms in vacuum and 4 ± 2 ms for ambient air conditions. The numbers were found relatively independent of the temperature step, or at least within the specified measurement error. The low measurement accuracy was due to the nature of the setup; as the resistance of the heater at room temperature was already much higher than the resistance of the wires, the high-temperature voltage drop was only about 10 % higher. Higher accuracy can be obtained by adding resistances or by measuring electric current settling. However, the result is in agreement with settling times of comparable Microheater designs [10], and it confirms the validity of the finite element model, which predicted 7–15 ms for vacuum and 4–9 ms for nitrogen. Settling goes faster for higher temperatures in which the current density is higher. Temperature settling graphs can be found in appendix C. The significant difference between vacuum and gas conditions are caused by two factors: in the gas case, the voltage and current are much higher for the same target temperature, and more importantly the gas helps spreading the heat. As the heat capacity of the gas is negligible, it reduces the settling time significantly.

In stationary gas conditions, the temperature stability is found to be better than 0.0054 °C. A typical sample is shown in figure 4.13a. For changing gas conditions, the temperature fluctuations become around 10 °C at 500 °C, shown in figure 4.13b. This is twice the 1 %-target that was set in subsection 3.1.1. At 285 s helium is flushed into the Nanoreactor to replace nitrogen, which results in a temperature drop as the heater has to compensate for the higher heat loss due to helium's higher thermal conductivity. At 1090 s nitrogen is flushed again, which results in a temperature peak, because the heat loss through nitrogen is much less.

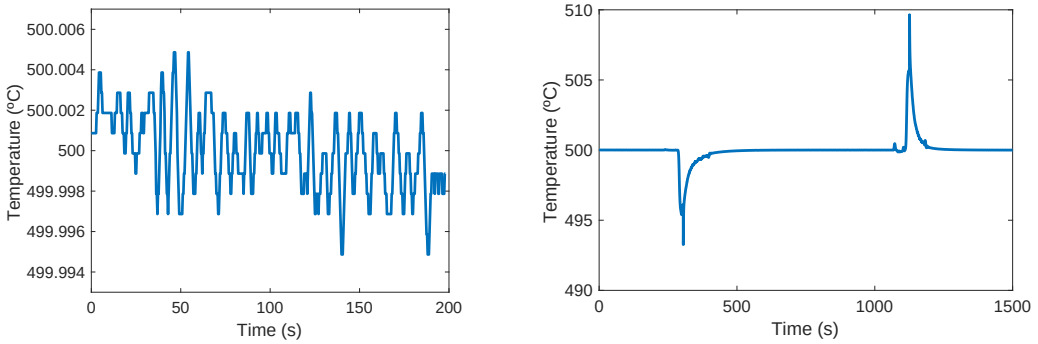

(a) Stability during stationary gas conditions

(b) Stability during changing gas type

Figure 4.13: Temperature fluctuations as function of time in **(a)** stationary conditions, and **(b)** while changing gas type.

Table 4.2: The table on the left provides the temperature-resistance relations for vacuum, nitrogen and helium. As the four-point-probe measures resistance, the relations manifest themselves in a temperature difference. The table on the right shows the simulated deviation for when the Nanoreactor is calibrated in one environment (left column) and used in another (top row).

Environment	$\frac{\Delta R}{\Delta T}$
vacuum	0.3140
nitrogen	0.2844
helium	0.2965

	vacuum	nitrogen	helium
vacuum	0%	-9.4%	-5.6%
nitrogen	+10.4%	0%	+4.3%
helium	+5.9%	-4.1%	0%

Temperature accuracy for different gases

The analysis on the homogeneity over the heater has shown that the temperature distribution varies between vacuum, nitrogen or helium conditions. The four-point-probe corrects for any external factors influencing the temperature accuracy. However, it cannot compensate for temperature gradients on the heating spiral that connects the four probes. To quantify the temperature difference that originates from this effect, the temperature-resistance relation has been simulated for vacuum, nitrogen (1 bar) and helium (1 bar). The relations are very linear; the R-squared value is 0.9999 or better. The results are given in table 4.2. The table also provides how the actual temperature would differ from the intended temperature, when the chip is calibrated for one environment and used in another. The results show that the optimized design should have its sensing probes connected closer to the center of the heating spiral to improve its compensation capability. The analysis further emphasizes the importance of incorporating a thermocouple or four-point-probe, as without it, the temperature discrepancies would be dramatically higher.

4.1.4. Gas switching time

To use the Nanoreactor as a gas sensor, its sensitivity to other variables had to be identified. For this purpose, an extensive characterization was done on power consumption as function of gas composition, gas pressure, gas flow rate, and temperature, over the whole operating range of the Nanoreactor. Graphs with the dependencies can be found in appendix B. It was found that power consumption was most sensitive to gas composition changes at 1000 mbar, where the difference between helium and nitrogen is a factor 2 approximately. Moreover, at high pressure, the power consumption is less sensitive to pressure changes. Just as the temperature homogeneity, power consumption is barely affected by flow rate. The difference between 0–1 $\mathrm{mL\,min^{-1}}$ varies typically between 0.1–3.0 % for low temperature nitrogen and high temperature helium conditions, respectively. Although the absolute power consumption varies more between nitrogen and helium at higher temperatures, this is also when it is most sensitive to the other variables. Next to these considerations, it is most useful to test for typical experimental scenarios. Therefore, the gas switching time was analyzed at 1000 mbar and 500 °C. During the experiment, the nitrogen and helium flow rate were 0.345 $\mathrm{mL\,min^{-1}}$ and 0.225 $\mathrm{mL\,min^{-1}}$, respectively. At these conditions, the data provided in appendix B was fitted by a polynomial to find the relation between gas composition and power consumption:

$$\phi = 0.2308P^2 - 17.43P + 326.4 \tag{4.2}$$

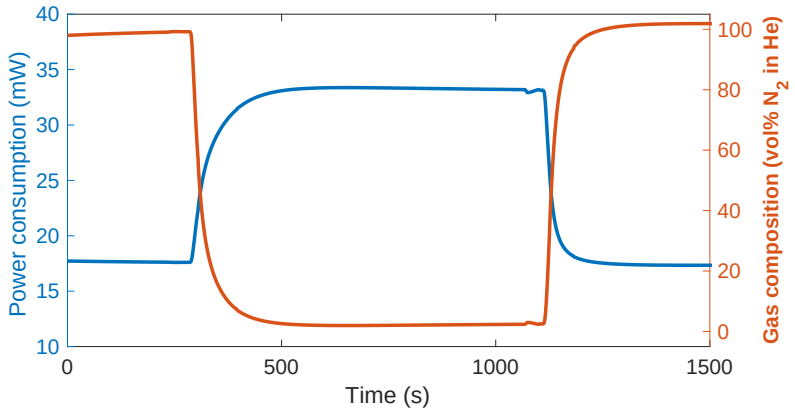

Figure 4.14: Power consumption and the thereof derived gas composition as function of time. The gas composition is expressed in vol% nitrogen, the remaining gas is helium.

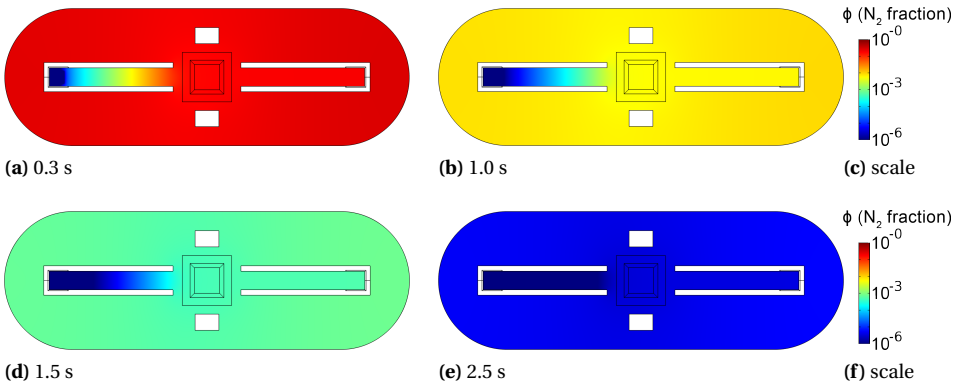

Figure 4.15: Gas switching from nitrogen to helium. The figures show the gas spatial gas composition for different moments in time. The gas composition is expressed as a fraction of the initial nitrogen condition; at t=0, the nitrogen fraction is 1 (100%), which rapidly decreases over time.

in which ϕ is the volumetric fraction of nitrogen in vol% and P the power consumption in mW. The power consumption and gas composition are shown as function of time in figure 4.14. It was found that 90 % of the nitrogen was replaced by helium after 120 s, and 99 % after 240 s. Switching from helium back to nitrogen went almost twice as fast, which can be explained by the higher nitrogen flow rate.

Results from the finite element model in figure 4.15 show very different behavior; it takes only 1.0 s to switch 99 % of the gas. After 1.5 s, the concentration of the old gas is less than 1 promille. For simulations, the gas is considered to be switched when the initial gas concentration is is below 1 ppm in every domain of the Nanoreactor, which is the case after 2.9 s.

The observed concentration gradients are well-explained by the gas switching theory of subsection 2.2.5. Using a characteristic length of 1 mm ($\sim W/2$), the gas flow from figure 4.4, and the binary diffusion coefficient for helium-nitrogen (appendix A), the Péclet number for mass transfer can be calculated. In the gas channel, $\mathrm{Pe}_{\mathrm{mass}} = 6.85$, which manifests itself by the gradient between the inlet and the Microheater region. Advection pushes the gas forward, but it is diffusing back at a significant rate. In the Microheater region, $\mathrm{Pe}_{\mathrm{mass}} = 0.66$, because the gas flow is slower. As diffusion occurs from multiple directions, gradients are hardly visible. For the outer regions, $\mathrm{Pe}_{\mathrm{mass}}$ =0.0001–0.06 , indicating those regions are diffusion dominated. As diffusion will thrive to smoothen gradients, the outer regions have roughly the same gas composition. The outlet channel has approximately the same composition as the Microheater and outer regions, because as soon as the particle enters the high flow speed region, it gets carried with the flow. Equation 2.23 further clarifies the dominance of diffusion; it only takes 4 ms for a gas particle to move an effective distance of 1 mm.

Since theory agrees with the model, it can be concluded that the gas switching time in this experiment was limited by the system rather than by the Nanoreactor. This makes sense, as tubing and valves all have dead volume which dilutes the incoming gas and smoothens the transition for one gas type to another.

According to equation 2.21, the diffusion coefficient scales $D \propto T^{\frac{3}{2}}$ with temperature. Also, gas flow speed increases with temperature as seen in figure 4.4. The increased mobility results in faster gas switching time. However, because the high temperature is very local, the effect of temperature is not very pronounced. Simulations show that the outgoing flux at 1000 °C is about 2 % higher than for room temperature. Simulations on the local Péclet numbers, and the temperature dependent binary diffusion coefficient of nitrogen-helium, can be found in appendix C and A, respectively.

4.2. Optimization

4.2.1. Mechanical stability

Membrane deflection

To meet the target, but in anticipation of the trade-off with power consumption, the bottom membrane size will be reduced to 500 µm, which should reduce membrane deflection to just below 10 µm. The top membrane already met the criteria, so it does not require to be reconsidered. Figure 4.16 shows the membrane deflection of the new bottom membrane as function of pressure. The results include the new Microheater design, which will be presented in subsection 4.2.3.

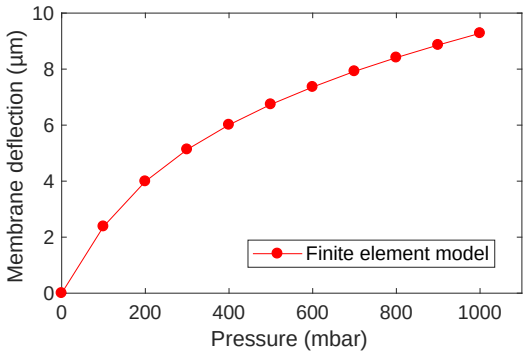

Figure 4.16: Membrane deflection as function of pressure. The optimized bottom chip membrane has an edge length of 500 µm.

The current Nanoreactor deflects 7 nm mbar^{-1}. With pressure fluctuations of 5 mbar (peak-to-peak), this equals up to 35 nm. This is acceptable for most high-resolution TEM purposes, but it can become a problem for STEM in which the focal length is less. The smaller membrane size reduces membrane deflection to less than 4 nm mbar^{-1}. It improves stability due to pressure fluctuations to 20 nm, which allows for more stable imaging at higher resolution. If an experiment requires even higher stability, the gas flow should be paused temporarily, because no fluctuations will occur in static gas conditions.

Spatial sample drift

The Nanoreactor has been optimized by reducing the heater size, improving the electrical probe design and reducing membrane deflection such that the gas layer becomes a lot thinner. These improvements have reduced the power consumption far below the minimal optimization target. It has decreased by 43 % for nitrogen and 50 % for helium. A few variants on the Microheater design have been simulated, which will be encountered in the upcoming subsections. Figure 4.17 shows the analogue of figure 4.3 for the optimized Microheater design and the 500 µm membrane.

4.2.2. Gas flow speed

In the current Nanoreactor, it was seen that the spacers guided the gas towards the Microheater, but the spacers stop at the center as they cannot continue on the membrane. As a result, the gas is able to spread in all directions and only a small portion actually passes the sample region. The current spacers were abandoned,

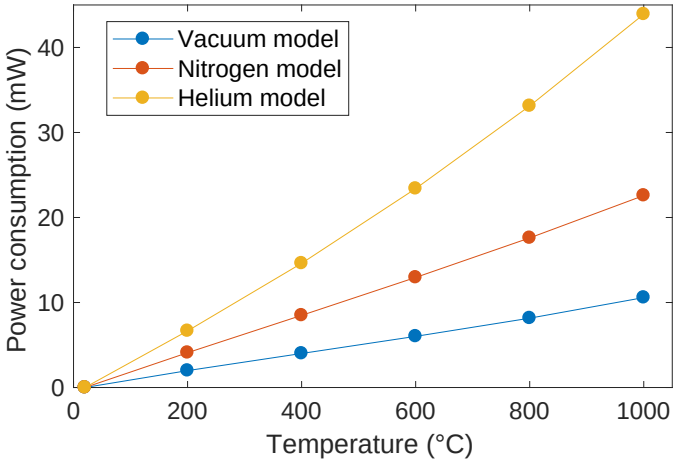

Figure 4.17: Power consumptions as function of temperature for the optimized Nanoreactor design, for vacuum and for the assembled Nanoreactor with 1 bar nitrogen or 1 bar helium inside.

and the design was started from the basic idea that all gas should go towards the heater. To do this, the spacers next to the membrane (from a flow perspective) were enlarged such that no flow could go besides the membrane. In effect, the principle was changed from guiding the gas in the proper direction to preventing the gas could go into other directions. These spacers were made wider at the edges of the chip than near the membrane to create a funnel that forces all gas to go towards the Microheater. Some tolerances had to be taken into account to ensure leak tightness and robustness. 100 µm space was kept between the spacer and the O-ring, which should not end up on top of the spacers as rough topography will result in gas leakage. A 50 µm distance was kept between the edge of the membrane and the start of the spacer, as tolerances on the wafer thickness or over-etching may cause the membrane to be a few tens of micrometers bigger. The reduced membrane size allows the side-spacers to become even larger and squeeze the gas into a narrower region. The new spacer design is highlighted in figure 4.18a. The triangular spacers are there to guide the gas towards the Microheater. The oval spacers are there to prevent that the top chip can tilt, ensuring the gas layer has the 5 µm thickness all over the Nanoreactor. Moreover, they are beneficial for gas switching purposes, but this will be discussed in subsection 4.2.4.

The new spacer design has a much lower flow resistance and ensures a much more uniform gas flow speed in the chip. The results for nitrogen are shown in figure 4.18. With the same pressure difference between the inlet and outlet, the total volumetric flow rate increased by 370 %. In the outer regions, where the gas flow speed was worst in the old design, the new design shows a flow speed up to 10000 times higher. This becomes very clear if the flow profiles are compared on the logarithmic scale; figure 4.4d and figure 4.18d. Of the total gas flow, 84 % passes the suspended membrane. In comparison, only ~30 % of the gas passes through the same region in the current design. This means the 90 percent target is not made. The target can be reached by reducing the safety margins on the tolerances that were included, or the triangular spacers could be made more obtuse to increase the flow resistance in the flow paths between the spacers and O-ring. However, that effectively reduces tolerances if the top chip would be placed slightly rotated, and increasing flow resistance will not be beneficial for the gas switching time or the overall flow rate.

Just as with the current Nanoreactor design, the effect of temperature results in a higher flow speed to keep the mass flow rate the same. The optimized design does not allow for much evasion, so the increase in flow speed with temperature is slightly higher. Considering other minor differences, figure 4.19 shows the difference between nitrogen and helium gas remain small. the gas flow speed is slightly lower for helium due to its higher viscosity. However, because the helium spreads heat more effectively, it experiences a larger flow speed increase with temperature. At 1000 °C, the top flow speed is almost 0.1 $\mathrm{m\,s^{-1}}$ higher.

The gas flow profile and flow rate have been greatly improved, but it was found that the gas flow settling time increased from 0.11 ms to 0.29 ms. This increase is a direct effect of the other improvements that were made. As more gas is flowing at a higher speed, the higher total inertia translates into a slower response. It is still much faster than the time scale at which the gas supply system works, so it remains insignificant.

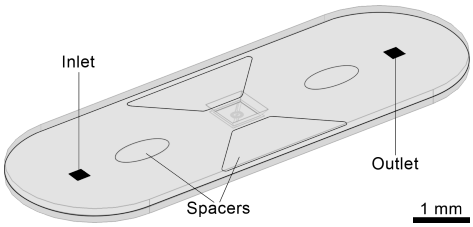

(a) Finite element model overview

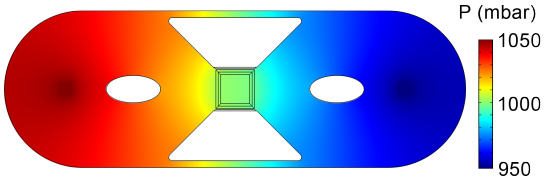

(b) Pressure distribution

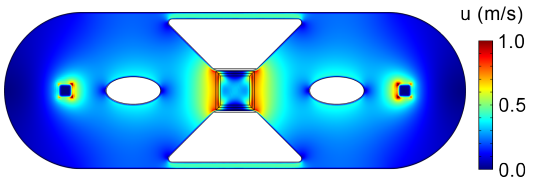

(c) Gas flow speed at room temperature

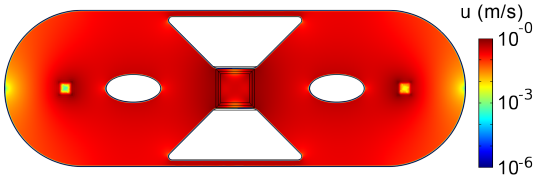

(d) Gas flow speed at room temperature

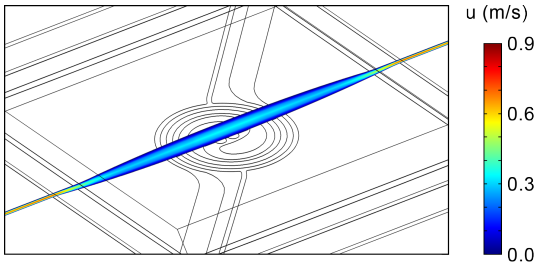

(e) Gas flow speed at room temperature

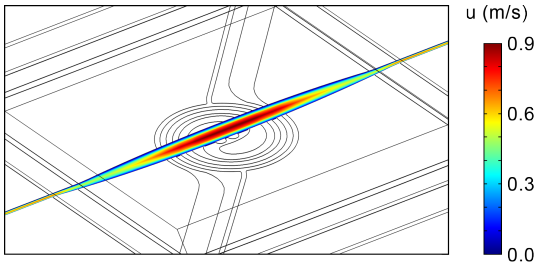

(f) Gas flow speed at high temperature

Figure 4.18: Optimized Nanoreactor finite element model with nitrogen gas. The gas flow direction is from left to right. **(a)** A schematic of the model. **(b)** Gas pressure distribution. **(c,d)** Gas flow speed over the gas volume plotted on a linear and logarithmic scale. **(e,f)** Close-up of gas flow in the Microheater region at room temperature and 1000 °C.

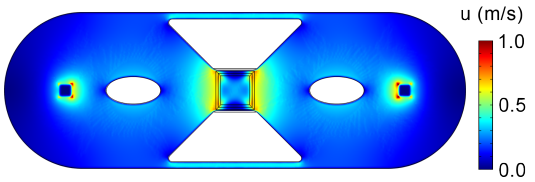

(a) Gas flow at room temperature

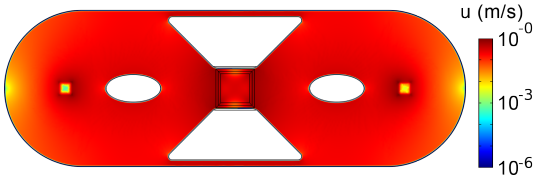

(b) Gas flow at room temperature

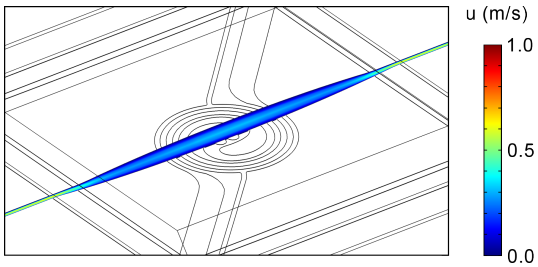

(c) Gas flow at room temperature

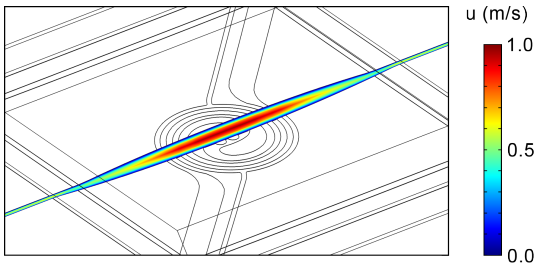

(d) Gas flow at high temperature

Figure 4.19: Optimized Nanoreactor cross-sections showing helium gas flow speed. The gas flow direction is from left to right. **(a)** Gas flow on a linear scale. To visualize the gas flow speed in the outer regions the same profile is plotted on logarithmic scales in **(b)**. The effect of temperature on the gas flow is shown by comparing **(c)** room temperature and **(d)** 1000 °C.

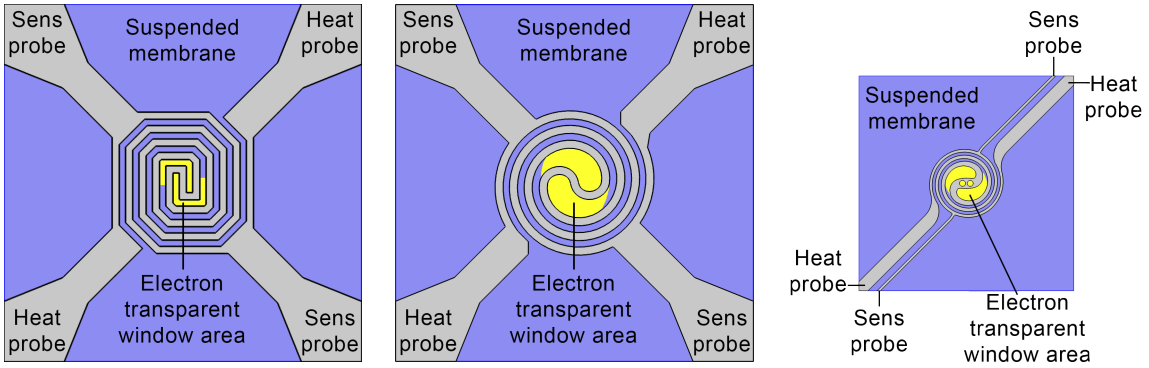

(a) Current design **(b)** An initial alternative design **(c)** Optimized heater design

Figure 4.20: Schematics to show the development of the heater design, drawn to scale. **(a)** The current heater design. **(b)** Existing alternative design to the current Microheater that formed the starting point for the optimization process. **(c)** The optimized heater design that followed from the optimization methods described in subsection 3.3.

4.2.3. Temperature and heat

Prior to the start of this project, a few alternative designs were fabricated, among them the design shown in figure 4.20b. The circular shape of this design avoids current crowding and it leaves more open silicon nitride space in the central region to include more electron transparent windows in the homogeneous area. It also has a slightly larger homogeneous area, but this is a bit of a delusion as the heater itself is simply bigger. This also exposes its major weakness; its power consumption is higher. As the design has the potential to include nearly all of the guidelines of table 2.2, 2.3 and 2.4, and because it allows for including electron transparent windows in the central area, this design became the starting point of exploring the optimization process.

The optimizations that followed from the intended methods (section 3.3) all affect the design. To explain the coherence in this subsection, a short preview of design optimizations related to the subsequent subsections is given. The first steps in the optimization were to reduce the heater size and introduce varying heater linewidth. A few practical constraints strongly couple the size and heater linewidth: preferably, the total heater resistance should stay about the same such that it remains compatible with the heating control electronics and software, the heater linewidth should not go below 5 µm to prevent microfabrication tolerances induced by the process from becoming significant, the pitch has a lower limit as well, to avoid dielectric breakdown of the silicon nitride, and last, enough space should be reserved to include electron transparent windows. In the optimization iterations for homogeneity, a trade-off was encountered between reducing size and including enough windows; space has to be kept between windows to avoid stress concentrations. A solution was inspired by the heat-spreading-structure design guideline; the metal wire is made wide enough in the center to have it encircle two windows. The advantage is twofold; the heat dissipation is distributed more evenly over the central region, and the metal spreads the heat smoothening the temperature profile. Due to the high thermal conductivity of the metal heater, a lot of heat is conducted to the substrate through the electric probes (see appendix C). The width of the sensing probe lines could be reduced easily, as they experience no Joule heating. The heating probe lines can be reduced until the additional Joule heating becomes comparable to the decline in heat flux, as in the end, it is the power consumption that should benefit from this adjustment. Furthermore, to improve the temperature accuracy for different gases, the sensing probes should be connected closer to the center. This unfortunately also creates a heat path which accounts for up to 3 % of additional power consumption. The heater design that will be analyzed in the remainder of this subsection is shown in figure 4.20c.

Homogeneity over the heater

The temperature distribution for the optimized design is shown in figure 4.21. Note that, in comparison to figure 4.7 and 4.8, the membrane edge length is 500 µm instead of 830 µm. As can be seen from the scale bar, the overall homogeneity for the optimized design is much higher. The hottest spot is no longer in the center of the heating spiral. In all cases, the center of the heater is at exactly 1000 °C, and depending on the gas condition the spot with the highest temperature varies by a few degrees. The advantage of having the hottest part surrounding the electron transparent window area is that it 'protects' the homogeneous region such that

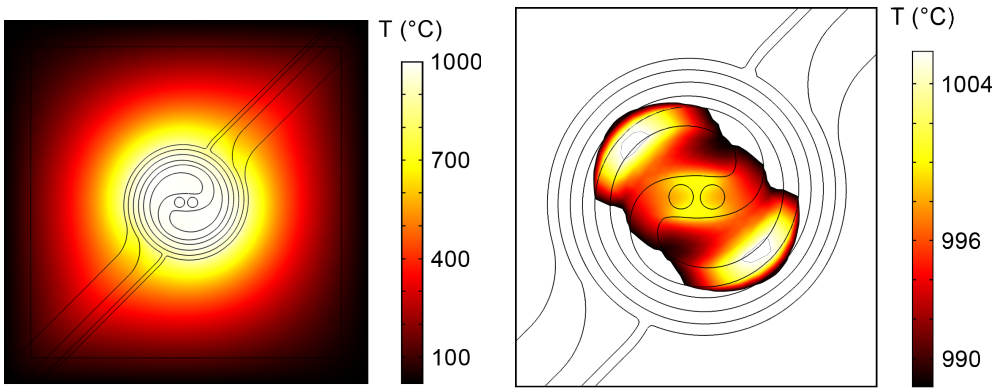

(a) Temperature distribution bottom membrane

(b) Homogeneity vacuum

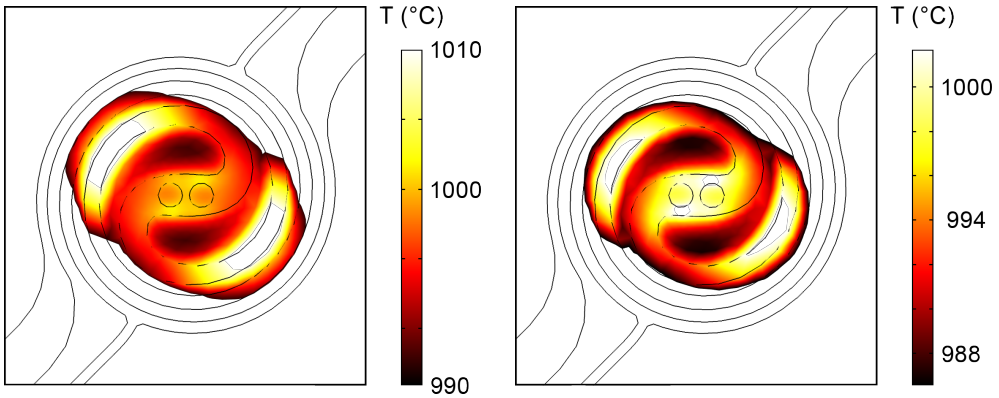

(c) Homogeneity nitrogen static

(d) Homogeneity helium static

Figure 4.21: Finite element analysis to determine temperature homogeneity over the region with electron transparent windows of the bottom chip at 1000 °C. **(a)** Temperature distribution over the membrane. Temperature distribution in the homogeneous area for **(b)** vacuum, **(c)** static nitrogen, and **(d)** static helium. The legends are adjusted to match the temperature distribution in the homogeneous region.

it is less affected by gas flow. It makes sure that, despite the smaller size, gas flow still affects homogeneity by a maximum of 0.2 %, just as in the current design. An overview of the homogeneity for vacuum, nitrogen, helium, static and flow conditions is given in table 4.3. Homogeneity is worst for high-temperature nitrogen gas flow conditions just as in the current design. The performance with helium is slightly better; this is due to the high thermal conductivity of helium which smoothens the temperature distribution. A disadvantage is that this also increases power consumption significantly. Although the results meet the 97.5 % target, homogeneity could be further improved by compensating for heat losses through the sensing probes. Simulations on the optimized heater design without sensing probes show an improvement, depending on the scenario, of up to 0.4 %. This would result in a homogeneity which is always 98.0 % or better. However, the sensing probes will be needed to improve temperature accuracy for different gas scenarios.

Homogeneity over the gas layer and top chip

By using the simplified analytical model shown in figure 3.6b, it was quickly identified that reducing the bottom membrane size was beneficial for power consumption as well as for homogeneity over the gas layer. As the top membrane is smaller, and the aspect ratios of the gas layer are such that heat easily transfers from bottom to top, the silicon frame of the top chip functions as the main heat sink. Therefore, the larger bottom membrane does not provide any additional thermal insulation, but results in more membrane deflection and a thicker gas layer that enhances the lateral heat conduction. The analysis of the homogeneity on the current Nanoreactor design in figure 4.9 confirms that tendency. It shows that the main temperature gradient is lateral and not much vertical, especially with helium.

Table 4.3: Temperature homogeneity over the central area in vacuum, nitrogen and helium conditions at different temperatures. For the nitrogen and helium cases, homogeneity is provided for static and flow conditions at a pressure of 1 bar. The gas flow conditions were as in figure 4.18 and 4.19. The results are obtained through finite element analysis. Read-out error is below 0.1 %.

Temperature (°C)	Homogeneity vacuum	Homogeneity nitrogen static	Homogeneity nitrogen flow	Homogeneity helium static	Homogeneity helium flow
20	100 %	100 %	100 %	100 %	100 %
200	98.5 %	98.5 %	98.2 %	98.7 %	98.6 %
400	98.4 %	98.3 %	98.1 %	98.6 %	98.6 %
600	98.5 %	98.1 %	98.0 %	98.5 %	98.5 %
800	98.6 %	97.9 %	97.9 %	98.5 %	98.5 %
1000	98.3 %	97.8 %	97.7 %	98.5 %	98.4 %

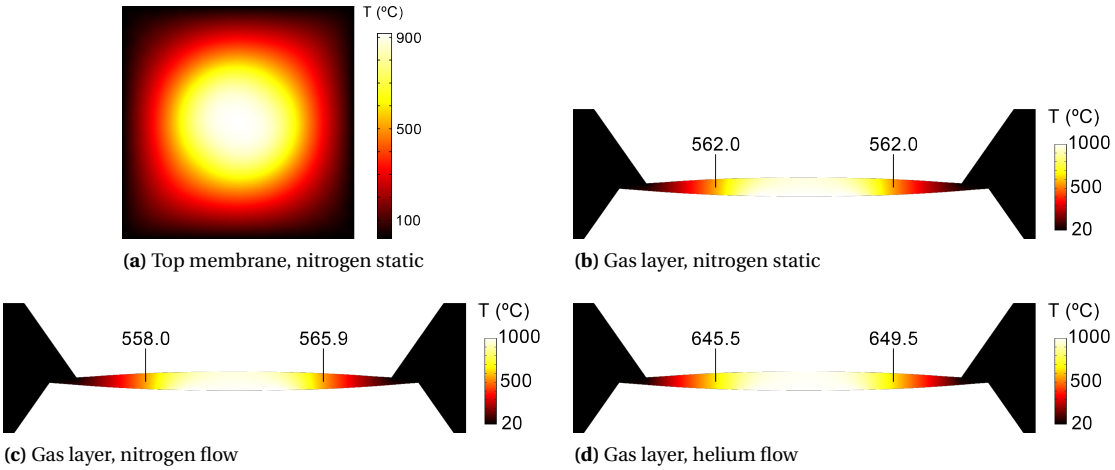

(a) Top membrane, nitrogen static

(b) Gas layer, nitrogen static

(c) Gas layer, nitrogen flow

(d) Gas layer, helium flow

Figure 4.22: Finite element analysis on temperature distribution with the optimized Microheater set to 1000 °C and gas pressure of 1 bar for the **(a)** top membrane with static nitrogen, **(b)** static nitrogen layer, **(c)** nitrogen layer with gas flow, and **(d)** helium with gas flow. The gas flow direction is from left to right.

The homogeneity over the gas layer has been analyzed for the optimized design. Due to the much smaller bottom membrane deflection, the gas layer thickness reduced from 35 µm to 23 µm at room temperature and 1 bar. The thinner gas layer results in a closer proximity between the bottom and top chip temperature:

$$\begin{aligned} T_{\text{top,nitrogen}} &= 0.953\ T_{\text{bottom}} \\ T_{\text{top,helium}} &= 0.985\ T_{\text{bottom}}\ . \end{aligned} \tag{4.3}$$

Even though the new Microheater is much smaller, its higher homogeneous high-temperature area contributes to the higher top chip temperature. However, the vertical temperature gradient has not changed a lot; the temperature is still 0.2 % less 1 µm above the Microheater, for nitrogen. Although a minor improvement was expected, the potential sample temperature error resulting from this gradient is so small that it cannot be considered significant with respect to the overall temperature accuracy.

Another remarkable result in figure 4.22 is how far the heat reaches laterally. The temperatures indicated at a 100 µm distance from the heater have dropped by about 100 °C, this drop is related to the reduced Microheater size. The confinement of the high-temperature homogeneous central region, and the sharp temperature gradient at the edge of the heater, clarify why this resulted in a much lower power consumption. The relative effect that gas flow has on the difference between the points up and down the flow direction has not changed by more than 1 °C, even though the gas flow speed went up and their is no heater underneath the measurement point. The Péclet number for heat transfer changes from 0.06 to 0.27, which shows that advection is starting to play a role, but its effect is counteracted by the higher homogeneity of the heater. Also, making the hottest points in the heater surround the electron transparent windows, instead of having the hottest point in the center, compensates for the additional power that is required to heat the higher flow rate of the incoming gas.

Table 4.4: The table on the left provides the temperature-resistance relations for vacuum, nitrogen and helium. As the four-point-probe measures resistance, the relations manifest themselves in a temperature difference. The table on the right shows the simulated deviation for when the Nanoreactor is calibrated in one environment (left column) and used in another (top row).

Environment	$\frac{\Delta R}{\Delta T}$
vacuum	0.2288
nitrogen	0.2312
helium	0.2314

	vacuum	nitrogen	helium
vacuum	0%	+1.0%	+1.1%
nitrogen	-1.0%	0%	+0.1%
helium	-1.1%	-0.1%	0%

Temperature settling and stability

The simulations for the optimized design shows comparable settling time to the current design: 6–11 ms for vacuum and 5–9 ms for nitrogen. For vacuum, the settling time reduction is achieved by a reduction in thermal mass while keeping thermal resistance approximately the same, as nothing has changed on membrane layer materials and thicknesses. For nitrogen, it appears that two opposing effects neatly cancel each other out. On the one hand, the reduced heater size and gas layer thickness result in a reduced thermal mass. On the other hand, the power consumption of the optimized design is so much lower that the required current is also much lower. Although the current density in the outer wires is higher, the effective average current density over the volume that has to be heated, is slightly reduced. In the end, even though the power consumption has been drastically reduced, the temperature settling time remains unchanged and the design constraint that demands not to increase response time is met. Opportunity is there to improve settling time by reducing the total resistance of the spiral such that a higher current can flow. However, for compatibility with the temperature control setup, it is desired that the heater resistance should not be changed. Additionally, the magnetic interference design constraint (subsection 3.1.3) demands that the current will not increase. So before a resistance reduction will be considered, the effect of violating this constraint on imaging related performance parameters should be identified.

To improve the temperature stability, the resistance measurement has to become more sensitive with temperature changes. The sensitivity of the optimized design is

$$\frac{\partial R/\partial T}{R} = 6.52 \cdot 10^{-4}/°\text{C}. \tag{4.4}$$

The improvement as compared to the current design (sensitivity of $5.94 \cdot 10^{-4}/°$C) is 9.8 %. This is perfect for stationary operating conditions, as the stability which was already fine improves further. In the gas switching scenario a temperature fluctuation of 2 % was measured in the current design. The attained improved predicts the temperature fluctuation will reduce to 1.8 %, which means that the 1 % target has not been achieved. As the sensing probes were connected as close to the central region as this design allows, and considering the point at which the sensing probes connect the heater reach about 80 % of the maximum temperature, it can be concluded that the 1 % target was never feasible. Only if the probes would connect to a theoretically maximum, a completely homogeneous area, the target will just be or just not be made. Therefore, to improve gas switching temperature stability further, the Microheater design should be completely different allowing to connect the sense probes to the hottest point in the center of the heater, or the electronics and the heating control algorithm should be optimized. In the first scenario, it will be very hard to maintain the current improvements on temperature homogeneity and power consumption, because extending the sensing probes all the way to the hottest points will certainly increase thermal conductivity of the membrane and enhance heat losses.

Temperature accuracy for different gases

The results for the redesigned sensing probes are presented in table 4.4. As compared to the current design, a major improvement has been achieved in temperature accuracy differences between different gas types. The new sensing probes, combined with the improved homogeneity, decrease the potential error by a factor 10 to 1.1 %, in the worst case. Although the mismatch is still to significant to neglect, it is minimized to be much smaller than standard calibration errors. Moreover, as the effect of gas type on temperature has been characterized, it can be taken into account to determine the exact sample temperature at which a certain phenomenon occurred.

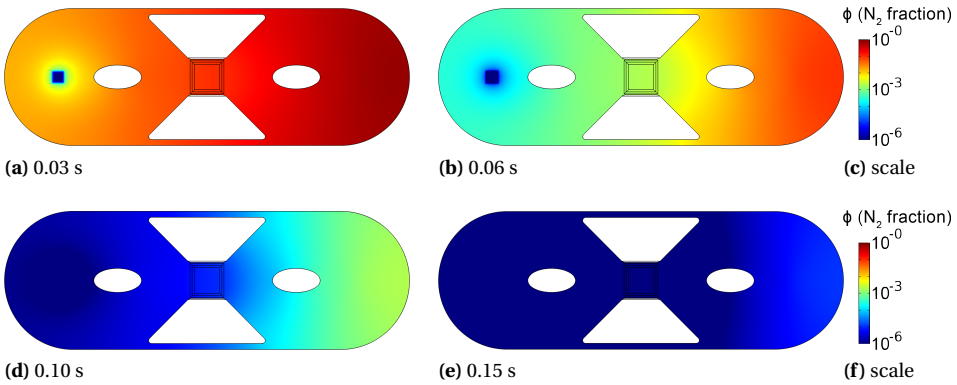

(a) 0.03 s **(b)** 0.06 s **(c)** scale

(d) 0.10 s **(e)** 0.15 s **(f)** scale

Figure 4.23: Gas switching from nitrogen to helium with optimized spacers. The figures show the spatial gas composition for different moments in time. The gas composition is expressed as a fraction of the initial nitrogen condition; at t=0, the nitrogen fraction is 1 (100%), which rapidly decreases over time.

4.2.4. Gas switching time

During the characterization it was found that gas switching time was greatly limited by the, basically absent, gas flow speed in the outer regions of the Nanoreactor. In those regions, gas switching relied on mass diffusion rather than advection. This was quantified through the Péclet number for mass transfer. The target was set to achieve $\mathrm{Pe}_{\mathrm{mass}} \geq 1$ in the entire Nanoreactor. To achieve this, the current spacers were removed such that the gas flow would spread over the entire volume of the Nanoreactor. To further distribute the flow equally (and to make sure the top chip has enough supports) oval spacers were introduced in the direct flow path. These force the gas flow to move sideways which further improves gas flow speed in the outer regions.

Using the same characteristic length as for the current design of 1 mm ($\sim W/2$), the binary diffusion coefficient for nitrogen-helium at room temperature, and the local gas flow speed, the Péclet number for mass transfer is determined. It is found to be 3.9 in the flow path surrounding the oval spacer and 4.7 in between the membranes. In the outer regions, which were formerly the bottleneck in gas switching time, the Péclet number went up a factor 400 to 0.04. Strictly speaking, those regions are not making the target, but since these domains are so small, equation 2.23 tells that it takes only 0.6 ms until this gas will have diffused into surrounding domains with Péclet higher than 1. Due to the optimized geometry and the high Péclet regions nearby, the contribution to gas switching time of these regions is far from significant. Appendix C contains a figure that shows the Péclet number everywhere in the Nanoreactor.

Simulations were run under the same conditions as for the current design in figure 4.15, with the only change in spacer design. The improvement in gas switching time is enormous: 99% of the gas had already switched after only 65 ms, the 1 promille concentration was reached in every domain of the Nanoreactor at 110 ms, and the point at which the gas is defined to be switched, 1 ppm, is found after 175 ms. To show the gas switching process, intermediate results are shown in figure 4.23 for a few moments in time. Note that these moments are chosen very different from the ones in figure 4.15, which is because gas switching time has become 16.5 times faster.

5

Discussion on the results and improvements

5.1. Optimized design proposal and its reliability

This section summarizes the design optimizations that were done to improve membrane deflection, spatial sample drift, temperature homogeneity, temperature stability, gas flow speed, and gas switching time. The proposed optimized Nanoreactor, of which the detailed results were presented in section 4.2, is shown in figure 5.1. All the changes on the design, including their purpose, are pointed out.

The intended optimization procedure explained before in subsection 3.1.1 was followed. The review of the state of the art in Microheaters and Nanoreactors provided a set of design guidelines. The study on the physics involved with thin film mechanics, heat transfer and micro gas flows, was used to identify in which regimes of physics the Nanoreactor manifests itself. The acquired knowledge was used to select appropriate experimental methods to characterize the Nanoreactor, and to confirm the physics regimes. The experimental results were used to develop a finite element model of the Nanoreactor in COMSOL Multiphysics. The model was tuned to match the characterization results by adjusting material properties based on characterizations and correlation between different performance parameters, while taking into account how material properties are different for thin films and at high temperature.

The reliability of the model is demonstrated by ensuring coherence between the simulation results and experimental results. The development of the model was started with the parameters that could be characterized with large certainty: membrane deflection with pressure, resistance of the metal heater at room temperature, the relation between current, voltage, resistance and power as function of temperature, pressure, and gas composition. On top of agreement for these phenomena, the temperature distributions that came out of the model were experimentally verified among the top and bottom membrane.

The sole weakness of the model regarding physics remains with the thermal material properties of the thin film membranes. Although these are made trustworthy by measuring all the performance parameters that rely on them, they lack the hard proof of a direct measurement. As discussed in the literature review, many material property characterization methods are proposed, but most of them are only reliable on a small temperature range or interfere with temperature themselves. To best substantiate the thermal aspects of the model, its variables were reduced by going back solely to the bottom chip in ultra high vacuum. In this experimental setup, the only heat loss mechanisms are thermal radiation, which can directly be measured using an infrared camera, and conduction through the membrane. The fact that the thermal radiation can be measured directly does not mean the temperature is known; it merely provides how much heat is radiated for a given Microheater power consumption (the temperature was obtained by Raman thermometry). This setup again provides an indirect measurement. However, the only unknown variable is the heat conduction through the membrane. If this scenario matches the model in vacuum, and still consistently matches the experimental results with nitrogen and helium (of which theory shows that very well known bulk properties apply, at least in the 1 bar gas pressure condition), the thermal material properties become incontestable.

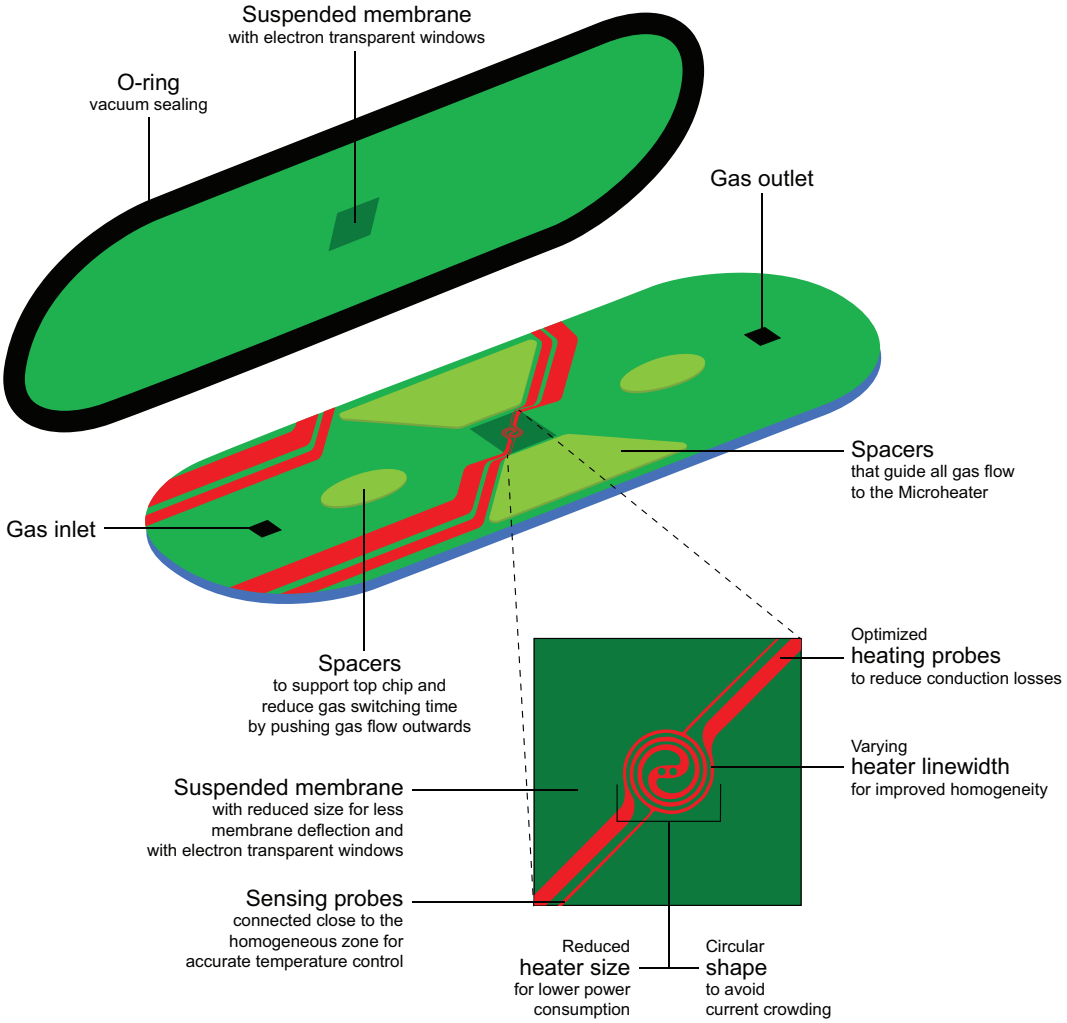

Figure 5.1: Schematic figure of the proposed optimized Nanoreactor with an overview of all the major optimizations.

As always with finite element analysis, the element quality plays an important role in the accuracy of the model. Typically, the smaller the elements, the better. Also, elements with large aspect ratios should generally be avoided as they limit the dimensional quality of the model. These elements can only be permitted if the dominating physics also has a lower dimensionality. The most evident method to ensure accuracy is by identifying the sensitivity of the model to the element quality. If a small step in element quality results in a significant change in simulation results, the element quality is too low. Increasing the element quality increases the degrees of freedom exponentially, which requires high computational resources. Often symmetry can be used to reduce the size of the model. However, in the case of the Nanoreactor, in which the major goal is to model the interdependence of various performance parameters and types of physics, no symmetry can be used. The first reason is that symmetry will break the heater lines, making it unable to model the interdependence of current, Joule heating, and the temperature dependent resistance. The second reason is that including inlet-outlet symmetry would not allow for modeling compressible gas flow; compressibility has to be taken into account to model local gas flow speeds accurately, as gas density varies with 10 % due to the pressure distribution and varies even more as function of temperature. To keep all types of physics active in the same model, the element quality had to be optimized for performance without reducing quality. The dependency of different types of physics on the element size were identified in minimum working examples. The most important results of this characterization can be found in appendix E. Furthermore, the computational requirements were reduced by simulating only part of the silicon substrate thickness and by limiting physics types to the domains in which they are relevant. Structural mechanics was only analyzed for the suspended membranes and electric current only in the metal Microheater. As gas is only present within the O-ring vacuum sealing, the MEMS part outside of this region was excluded.

5.2. Compliance of the obtained results

While the results in chapter 4 are usually directly discussed on whether they are plausible with regards to the literature and theory in chapter 2, the compliance of the obtained results and optimized Nanoreactor design have not been considered regarding the design constraints in subsection 3.1.3. In this section, a moment of thought will be given to them, one by one. Whenever possible, it was assessed if the design constraints are not violated, but unfortunately this sometimes could not be done for cases that require to have a prototype. If relevant, substantiations can be found in appendix B for experimental data and appendix C for simulation data.

Mechanical stress was supposed not to increase. Already by the theory, no issue was expected here, because reducing the membrane size results in lower stress levels. Although finite element analysis is not very reliable in determining stress levels absolutely, it is very suitable in determining them relatively. This was done, and a decrease of 25 % in Von Mises stress was observed.

Thermal stress itself was not assessed in the models. However, as it was found that the top membrane gets nearly as hot as the bottom membrane, a smaller membrane size will not cause problems here. Since the layer composition has stayed the same, and the total heated area has decreased, the thermal stress decreases as well.

Stress distribution will remain the same as the membrane remains square. The circular heater does not affect the distribution significantly for mechanical stresses, and for thermal stress, circular shapes are generally better.

Range and lifetime could not be directly tested, as this would require to leave a prototype up and running for hours or probably a few days. However, electromigration is often mentioned in literature as a failure mechanisms for high-temperature operation. Tests on the current Nanoreactor design have shown that electromigration does not play a role in its 20–1000 °C operating range. In fact, electromigration remains insignificant (and undetectable) up to 1300 °C. The optimized design requires less current, but also has much thinner lines. However, the optimized design does not suffer from current crowding. As a result, the current density in the thinnest heater lines is the same as near the sharp corners of the current design. Moreover, the outer lines experience less heat and are therefore more resistant to electromigration than the sharp corners at the center of the current design. Therefore, it is concluded that the current density will not impair lifetime.

Accuracy mainly depends on the calibration and not on the Nanoreactor design. However, results show that not correcting for the gas composition causes a reduce in accuracy. In the optimized design, the increased homogeneity and the new sensing probe design have reduced this problem to a minimum.

Response time was assessed in the finite element model. Simulations show that, in the worst case, the temperature settling time remains unchanged, whereas for some conditions an (unintended) improvement of a few milliseconds was achieved.

Sample compatibility has improved a little. Although the electron transparent windows have not been included in the design and simulations, figure 4.20 compares the regions assigned to include electron transparent windows. The surface area in which windows can be embedded has been increased by a small amount. The topography that surrounds the windows has decreased, because the windows no longer need to have metal lines close by (except for the central two window spots).

Resolution depends on the thickness of the silicon nitride windows and gas layer thickness. The first has not been changed and the latter reduces from 35 µm to 22 µm, so if it was not already on the TEM's resolution limit, it may further improve.

Ultra high vacuum will, as expected, not be affected. The vacuum sealing remains unchanged and the gas volume in the Nanoreactor has barely changed.

Magnetic field interference goes down. The total current drops by approximately 25 %, resulting in smaller magnetic fields. Moreover, the heater lines with opposing current directions are spaced closer together, enhancing their capability to compensate each others magnetic fields through superposition.

Charging of the membrane will happen to the same extent. However, the two central spots for windows are completely surrounded by very nearby heater lines. These two windows should be able to discharge floating charges more easily.

Microfabrication tolerances on heater linewidth and feature size spacing have all been taken into account. SEM inspections have been done to identify roughness of the heater wire sides. As a reference for feature spacing and sizes, another MEMS-based sample carrier for heating-biasing with even smaller features has been used as a benchmark, presented by Pérez Garza *et al.* [1].

To conclude, none of the design constraints have been violated. It could be argued that a minor concession has been made regarding current density, but since the current design already experienced the higher values locally, and because its limit was not reached, no issues are expected here. Regarding the other constraints, some stayed the same, while some even experienced improvements.

5.3. Comparison of the current and optimized design

Chapter 4 presents the results subject by subject, including various in-between results on the underlying physics and mechanisms. However, the goal was to improve the performance of the Nanoreactor regarding the six performance parameters that are important to enable rapid real-time *in-situ* TEM studies. This section aims to provide a clear overview that compares the optimized design to the current design, expressed in these performance parameters. To do this, general and relative results are put into absolute numbers for the most typical scenario; high temperature and atmospheric pressure. Also from a technological perspective, this scenario is most interesting, because this is where the technological boundaries have to be pushed.

Table 5.1 provides the overview of the performance of the current and the optimized Nanoreactor design. A brief explanation has been added to define to which specific scenario the numbers apply. However, the cases are representative for the relative performance over the full operating range of the Nanoreactor. The table shows that improvements for mechanical deflection, spatial sample drift (power consumption) and temperature homogeneity are around 50 %. For stability it is a little less, and for gas flow speed and gas switching time it is much more than that.

Table 5.1: Performance of the current and optimized Nanoreactor design. Unless specified otherwise, the performance is defined at a gas pressure of 1 bar at room temperature.

Performance parameter	**Experimental or modeling conditions**	**Current Nanoreactor design**	**Optimized Nanoreactor design**
Membrane deflection	Deflection of the bottom chip Sensitivity of deflection to pressure fluctuations	22.1 µm 7 nm mbar^{-1}	9.3 µm 4 nm mbar^{-1}
Spatial sample drift*	Power consumption static nitrogen at 1000 °C Power consumption static helium at 1000 °C	39.7 mW 81.0 mW	22.6 mW 43.9 mW
Temperature homogeneity	Static nitrogen at 1000 °C Static helium at 1000 °C	93.9 % 94.7 %	97.8 % 98.5 %
Temperature stability	Constant gas composition at 500 °C Changing gas composition 500 °C	0.0054 °C 10.0 °C	0.0049 °C 9.0 °C
Gas flow speed	Between the membranes for an inlet-outlet pressure difference of 100 mbar	4.3 cm s^{-1}	33.1 cm s^{-1}
Gas switching time	Defined as when the initial gas concentration is below 1 ppm	2.9 s	0.175 s

*Considered through its main influential factor; power consumption.

5.4. Reflection on the obtained improvements

The results as shown in table 5.1 are insightful for the experimental use of the Nanoreactor, but to reflect on the obtained improvements from a technological perspective, the physics behind them are relevant. The underlying physics determines how far the optimization is pushed towards the limits, what these limits were for the current design, and are for the optimized design. The attained performance will be discussed one by one with regards to the targets set in subsection 3.1.1. It will follow whether the conceptual solutions were adequate and sufficient to make the target. Furthermore, the benefits of the improvements will be discussed regarding to what extent they solve the problem as it was described in the problem statement in section 1.2.

A summarizing table is provided that lists the attained performance and the target: table 5.2.

Membrane deflection was the first optimization that was executed. It has been tackled by reducing the membrane size until the target was made, which was suggested as the only conceptual solution within the constraints that were set. The target was not based on a hard number as deflection itself does not necessarily limit the research possibilities of the Nanoreactor. It is desired to define the gas layer thickness more accurately and was based on what seemed realistically achievable considering that power consumption was also desired to decrease. However, in the heater optimization, it was found that the power consumption could be reduced further than expected. This leaves room to explore smaller membrane sizes and further reduce membrane deflection, but at the cost of the power consumption improvement. The more important specification is how pressure fluctuations can cause defocussing. The goal was ambitiously set to have no defocussing at all. However, the broad type of experiments that TEM, and especially STEM, allow for, can require the deflection to be of single nanometers. The attained improvement does not make this target, but will make a step forward in enabling higher quality TEM imaging and increase the chance of successfully executing STEM experiments. This does not mean high quality STEM cannot be done at all; by closing the valves of the holder the pressure will not experience any fluctuations anymore, but the gas flow will also be stopped. Therefore, it can be concluded that the target is met for a range of applications, and the target is partially met.

Spatial sample drift depends, as discussed in subsection 3.2.1, on various aspects. From the MEMS perspective, power consumption is the most important influential factor. As drift was already good enough to enable high resolution imaging of solid-gas interactions, no major improvements were aimed for. However, while reducing the heater size and optimizing the geometry, it was found that it had much more room for improvement than expected. Contrary to initial expectations, the reduction of the bottom membrane size contributed to a reduction in power consumption. The reason for this is that the top chip was already the most significant heat sink, and the thinner gas layer reduces lateral heat conduction through the gas. Simulations show that putting the optimized heater on a membrane of 800 µm instead of 500 µm shows an approximate 7 % increase in power consumption. It turned out the ratio between bottom and top membrane size is of a significant importance. The target for power consumption was largely exceeded, which could therefore potentially be compromised in a trade-off to other performance parameters.

Temperature homogeneity was, as expected from literature, greatly improved by introducing varying linewidth. When the targets were set, it was expected that gas would have a negative influence on the homogeneity. However, judging by the results in table 4.22 this turned out to be not as straightforward. Depending on the temperature and type of gas it can also have a smoothening effect on the temperature distribution. The target was made for vacuum, nitrogen and helium conditions over the full temperature range. Although it was not the goal, the foreseen 99 % homogeneity for vacuum was not obtained. Before judging this, it must be said that the heater was optimized for gas scenarios and space had to be reserved for electron transparent windows. Because of that, the heater lines could not be placed as close to each other as was the case in the literature examples that did obtain the 99 %. The space in between the heater lines experiences radiative heat losses that explain why 98.5 % homogeneity in vacuum was the limit for a design including electron transparent windows.

Temperature stability turned out to be a more complicated performance parameter to improve. Initially it was thought that the sensitivity to temperature fluctuations could be improved significantly by measuring closer to the center of the Microheater. Although the principles behind this concept stand, it appeared that the fundamental limit was closer than foreseen. Sensitivity depends on how much the relative resistance changes to temperature. In the current Nanoreactor design, the relative resistance change is unnecessarily low because it averages over heater lines which experience a lower temperature and thus a lower resistance change. To avoid this averaging, the sensing lines should probe an area that is as homogeneous as possible. This was attempted in the optimized design by improving homogeneity and the probing location. However, it was found that the resistance change, or the TCR of the heater material, imposes a fundamental limit on the relative sensitivity. Artificial simulations with 100 % homogeneity show that the optimized design reaches to within 99.8 % of the theoretical maximum sensitivity of $6.53 \cdot 10^{-4}$ /°C at 1000 °C. Therefore, it can be concluded that the optimization limit has been reached from the MEMS perspective, which means the optimization result is the best that can be achieved.

Gas flow speed had the target to ensure 90 % of the gas flow would pass the membrane area. The target was almost made by reaching 84 %. The remaining gas slips through the narrow channels in between the spacers and the O-ring vacuum sealing. Those narrow channels are necessary to ensure leak tightness, as minor

misalignments should not result in that the O-ring ends up on top the spacers. Next to this concrete limitation, it has become harder to achieve the result due to the way the target was formulated. Getting a certain percentage of the gas flow in the membrane region becomes harder if the size of the membrane is reduced. The target could be achieved by reducing the pressure drop over the side-channels by carefully positioning other spacers. For example, the oval spacers which are now there to benefit gas switching time and support to the top chip should be removed, instead additional spacers should be placed near the entries and exits of the side-channels. The reasons why this has not been done is due to the trade-off with gas switching time. Having the proposed alternative would further reduce the gas flow speed in the regions where it is already lowest. Therefore, it is accepted that the target is just not made.

Gas switching time would normally be expressed in a time-unit. However, since the actual time depends on the gas type and the applied pressure difference between the inlet and outlet, the Péclet number for mass transfer provides a more technical and generally applicable measure of the performance. Advection has improved enormously by the new spacer design which has greatly harmonized the gas flow speed distribution in the Nanoreactor. When not taking into account local extremes in domains on the scale in which diffusion is still able to rapidly smoothen gradients, the Péclet number varies between 1 and 15, which means the target has been achieved, and often overachieved. Also judging by the improvement in time (table 5.1) the new spacer design is a major improvement for fast gas switching, and therefore, for having a much more accurately defined gas composition inside the Nanoreactor.

Table 5.2: Attained improvements with the optimized Nanoreactor design and the targets set in subsection 3.1.1.

Performance parameter	**Experimental or modeling conditions**	**Optimized Nanoreactor design**	**Target**	**Success**
Membrane deflection	Gas pressure of 1 bar at 20 °C Stationary gas conditions at 1 bar	9.3 µm 4 nm mbar^{-1}	<10 µm No loss of focus	✔ ✓✗
Spatial sample drift	Static 1 bar nitrogen at 1000 °C Static 1 bar helium at 1000 °C	22.6 mW (43 %) 43.9 mW (50 %)	reduce by >10 %	✔
Temperature homogeneity	Static 1 bar nitrogen at 1000 °C Static 1 bar helium at 1000 °C	97.8 % 98.5 %	97.5 %	✔
Temperature stability	Constant gas composition at 500 °C Changing gas composition 500 °C	0.0049 °C 1.8 %	<0.01 °C <1 %	✔ ✘
Gas flow speed	Between membranes for inlet-outlet pressure difference of 100 mbar	84 %	90 %	✓✗
Gas switching time	Characteristic length of 1 mm, excluding extremes in domains with radius <0.5 mm	Pe_{mass} =1–15	$Pe_{mass} \geq 1$	✔

6

Conclusion

6.1. Achievements

The goal of this project was to design an optimized Nanoreactor that enables real-time *in-situ* TEM studies without interventions, while applying and changing stimuli to the sample.

A literature review was performed to study the state of the art in Microheater and Nanoreactor technology and find out which mechanisms are currently limiting real-time TEM imaging. An abundant amount of literature was found on Microheater development and optimization for various application fields. Since no review on this matter was encountered, the literature study was written as a review article of which the revision is currently under review by the Journal of Microelectromechanical Systems. It provides designers with an overview of the relevant physics and a set of design guidelines to achieve the desired Microheater performance. The available literature on Nanoreactors was limited, which is why it was necessary to determine the Nanoreactor design guidelines directly from the governing physics. Next to the presentation of conceptual solutions to optimize membrane deflection, spatial sample drift, temperature homogeneity, temperature stability, gas flow speed, and gas switching time, it was concluded that the Nanoreactor operates in various transition regimes regarding thermal convection, laminar or molecular flow, and gas advection or diffusion.

Given the predictions by literature and theory, appropriate microscale inspection techniques were selected. Infrared imaging and Raman thermometry were used to characterize temperature and heat, white light interferometry was used to measure membrane deflection, and the Climate system setup was used to determine electrical aspects and power consumption for nitrogen and helium gas at different temperatures, pressures and flowrates. With the experimental results and theory from the literature study, a finite element model was developed in COMSOL Multiphysics that simulates the thermo-electro-mechanical behavior of the Nanoreactor. This model was used to analyze the relevant parameters that limit the performance, and how these are interrelated. Within the given constraints, the design guidelines were turned into conceptual solutions. The finite element model was used to answer how the performance could be improved, and to predict the effect of redesigning and optimizing the Nanoreactor.

The optimized design shows improvements in all performance parameters. By reducing the membrane size, membrane deflection has improved from 22 µm to 9.3 µm at 1 bar gas pressure. Spatial sample drift has improved through reducing the power consumption by 43–50 %. This was achieved by reducing the heater size and optimizing the electrical contact probes, while keeping the electron transparent window area similar. Temperature homogeneity over the windows was improved from 93.9 % to 97.7 % by carefully tuning the local Joule heating through the concept of varying heater linewidth. A 9.8 % improvement was obtained in temperature sensitivity of the sensing probes, by connecting them closer to the center of the Microheater. This reduces temperature fluctuations and improves accuracy in circumstances with varying gas compositions. The gas flow that passes and can potentially interact with the sample is now 84 % instead of 30 %, and additionally the gas flow speed has increased by a factor 7.7 to 33 $\mathrm{cm\,s^{-1}}$. The gas switching time has been reduced by omitting spacers that prevent the occurrence of isolated regions. The spacers have been redesigned to enhance advection, resulting in a locally up to 400 times higher Péclet number for mass transfer. In effect, the gas switching time reduced from 2.9 s down to 0.175 s.

The obtained improvements in homogeneity, stability and gas switching time make sure the sample experiences more accurately defined temperature and gas stimuli such that it is known exactly under which circumstances the investigated phenomena occur. The improvements on membrane deflection and spatial sample drift reduce the loss of focus and tracing of the sample, which effectively allows to exploit higher magnifications. Moreover, at the same magnification, larger changes in temperature of gas stimuli will no longer result in loss of focus, which enables the real-time study of rapid solid-gas interactions inside the TEM.

6.2. Recommendations

Although the optimization has come a long way, the trade-off between membrane size and power consumption has not been fully exploited yet and may be worth additional analysis. In addition, the optimization achievements have not yet been experimentally confirmed. The recommended way to proceed this research is as following:

1. The membrane size was reduced far enough to meet the membrane deflection target, but the heater size reduction decreased the power consumption more than expected, leaving room to further exploit this trade-off. In the optimized design proposal the power consumption and temperature homogeneity get the full priority in the trade-off. However, the other requirement on membrane deflection sensitivity to pressure fluctuations has not been completely fulfilled. It is recommended to investigate how reducing the membrane size to 450 or even 400 µm would affect the various performance parameters. Depending on the extent of the improvements and impairments, a choice must be made in the trade-off. Note that the membrane size can always be changed in retrospect by using another wafer thickness.
2. Depending on the choice in bottom membrane size, consider adjusting the top membrane to the exact same dimensions. The obtained results have indicated that differences between top and bottom membrane size are not beneficial for power consumption; the larger membrane causes unnecessary deflection, while the smaller membrane defines the heat sink.
3. Consider including the interdependence of gas flow, mechanical and thermal membrane deflection to further increase the reliability of the model. Until now, a choice was made to include temperature and mechanics, temperature and gas flow, or gas flow and mechanics, but not all three simultaneously. This would, however, require a resourceful computer, especially in terms of memory usage.
4. Fabricate and characterize the prototype of the optimized Nanoreactor design using the methods described in this thesis. If necessary, refine the finite element model based on the characterization results.
5. Fabricate the (refined) optimized Nanoreactor. If necessary, confirm that the refinements provide the desired results.

Based on the results of this research, is was found that certain performance parameters were limited by the setup rather than by the Nanoreactor itself. To improve the performance on the parameters for which this statement holds, the following recommendations are made:

- Although the Nanoreactor allows for some more improvement on how deflection depends on pressure, it should also be considered if pressure stability can be improved from the source. This may further enable high resolution TEM and STEM imaging.
- The optimized Nanoreactor design reached the theoretical limit to within 99.8 % regarding temperature control sensitivity. As this was not enough to make the target on temperature stability during gas switching, it is recommended to optimize the heating control electronics and software. The stability could be increased by increasing the sampling rate, resulting in that the temperature corrections are executed at a faster rate, or by amplifying the controller's reaction, such that the corrections are of a larger amplitude. When increasing the reaction, care has to be taken that stationary stability is not mitigated. Increasing the sampling rate would therefore be the preferred option.
- It was shown that the Nanoreactor allows for very fast gas switching times in the order of a second. However, the gas switching time of the experimental setup is in the order of a minute. To exploit the Nanoreactor's capabilities to a maximum, it should be considered to study the cause, reduce dead volume and improve gas switching time of the gas supply system.

Bibliography

[1] H. H. Pérez Garza, Y. Pivak, L. Molina Luna, J. T. van Omme, R. G. Spruit, M. Sholkina, M. Pen, and Q. Xu, "MEMS-based sample carriers for simultaneous heating and biasing experiments: A platform for in-situ TEM analysis," in *2017 19th International Conference on Solid-State Sensors, Actuators and Microsystems (TRANSDUCERS)*. IEEE, jun 2017, pp. 2155–2158. doi:10.1109/TRANSDUCERS.2017.7994502

[2] M. L. Taheri, E. A. Stach, I. Arslan, P. Crozier, B. C. Kabius, T. LaGrange, A. M. Minor, S. Takeda, M. Tanase, J. B. Wagner, and R. Sharma, "Current status and future directions for in situ transmission electron microscopy," *Ultramicroscopy*, vol. 170, pp. 86–95, nov 2016. doi:10.1016/j.ultramic.2016.08.007

[3] A. Ziegler, H. Graafsma, X. F. Zhang, and J. W. Frenken, Eds., *In-situ Materials Characterization*, ser. Springer Series in Materials Science. Berlin, Heidelberg: Springer Berlin Heidelberg, 2014, vol. 193. doi:10.1007/978-3-642-45152-2

[4] D. B. Williams and C. Barry Carter, *Transmission Electron Microscopy*. Cham: Springer International Publishing, 2016. doi:10.1007/978-3-319-26651-0

[5] H. Saka, T. Kamino, and S. Arai, "In Situ Heating Electron Microscopy," *Materials Research Society*, vol. 33, no. February, pp. 93–100, 2008.

[6] A. K. Erdamar, S. Malladi, F. D. Tichelaar, and H. W. Zandbergen, "Closed Cell Systems for In Situ TEM with Gas Environments Ranging from 0.1 to 5 Bar," in *Controlled Atmosphere Transmission Electron Microscopy*, T. W. Hansen and J. B. Wagner, Eds. Cham: Springer International Publishing, 2016, vol. August, pp. 165–210. doi:10.1007/978-3-319-22988-1_6

[7] S. Chaturvedi, P. N. Dave, and N. Shah, "Applications of nano-catalyst in new era," *Journal of Saudi Chemical Society*, vol. 16, no. 3, pp. 307–325, jul 2012. doi:10.1016/j.jscs.2011.01.015

[8] H. H. Perez-Garza, D. Morsink, J. Xu, M. Sholkina, Y. Pivak, M. Pen, S. van Weperen, and Q. Xu, "The "Climate" system: Nano-Reactor for in-situ analysis of solid-gas interactions inside the TEM," *2016 IEEE 11th Annual International Conference on Nano/Micro Engineered and Molecular Systems (NEMS)*, pp. 85–90, 2016. doi:10.1109/NEMS.2016.7758206

[9] H. H. Pérez Garza, D. Morsink, J. Xu, M. Sholkina, Y. Pivak, M. Pen, S. van Weperen, and Q. Xu, "MEMS-based nanoreactor for in situ analysis of solid–gas interactions inside the transmission electron microscope," *Micro & Nano Letters*, vol. 12, no. 2, pp. 69–75, feb 2017. doi:10.1049/mnl.2016.0290

[10] P. Bhattacharyya, "Technological Journey Towards Reliable Microheater Development for MEMS Gas Sensors: A Review," *IEEE Transactions on Device and Materials Reliability*, vol. 14, no. 2, pp. 589–599, jun 2014. doi:10.1109/TDMR.2014.2311801

[11] K.-N. Lee, D.-S. Lee, S.-W. Jung, Y.-H. Jang, Y.-K. Kim, and W.-K. Seong, "A high-temperature MEMS heater using suspended silicon structures," *Journal of Micromechanics and Microengineering*, vol. 19, no. 11, p. 115011, nov 2009. doi:10.1088/0960-1317/19/11/115011

[12] D. Beckel, D. Briand, A. Bieberle-Hütter, J. Courbat, N. F. de Rooij, and L. J. Gauckler, "Micro-hotplates A platform for micro-solid oxide fuel cells," *Journal of Power Sources*, vol. 166, no. 1, pp. 143–148, mar 2007. doi:10.1016/j.jpowsour.2006.12.072

[13] J. Duvigneau, H. Schönherr, and G. J. Vancso, "Nanoscale Thermal AFM of Polymers: Transient Heat Flow Effects," *ACS Nano*, vol. 4, no. 11, pp. 6932–6940, nov 2010. doi:10.1021/nn101665k

[14] P. Dubois, E. Vela, S. Koster, D. Briand, H. R. Shea, and N. F. de Rooij, "Paraffin-PDMS composite thermo microactuator with large vertical displacement capability," in *Proc. 10th Int. Conf. New Actuators, Bremen, Germany*, 2006, pp. 215–218. [Online]. Available: https://infoscience.epfl.ch/record/114025/files/LMTS-CONF-2006-002.pdf

[15] P. Machtle, R. Berger, A. Dietzel, M. Despont, W. Haberle, R. Stutz, G. Binnig, and P. Vettiger, "Integrated microheaters for in-situ flying-height control of sliders used in hard-disk drives," in *Technical Digest. MEMS 2001. 14th IEEE International Conference on Micro Electro Mechanical Systems (Cat. No.01CH37090)*. IEEE, 2001, pp. 196–199. doi:10.1109/MEMSYS.2001.906512

[16] V. Milanovic, E. Bowen, M. E. Zaghloul, N. H. Tea, J. S. Suehle, B. Payne, and M. Gaitan, "Micromachined convective accelerometers in standard integrated circuits technology," *Applied Physics Letters*, vol. 76, no. 4, p. 508, 2000. doi:10.1063/1.125803

[17] J.-s. Han, Z.-y. Tan, K. Sato, and M. Shikida, "Thermal characterization of micro heater arrays on a polyimide film substrate for fingerprint sensing applications," *Journal of Micromechanics and Microengineering*, vol. 15, no. 2, pp. 282–289, feb 2005. doi:10.1088/0960-1317/15/2/006

[18] R. V. Gargate and D. Banerjee, "In Situ Synthesis of Carbon Nanotubes on Heated Scanning Probes Using Dip Pen Techniques," *Scanning*, vol. 30, no. 2, pp. 151–158, mar 2008. doi:10.1002/sca.20094

[19] N. O. Savage, S. Roberson, G. Gillen, M. J. Tarlov, and S. Semancik, "Thermolithographic Patterning of Sol-Gel Metal Oxides on Micro Hot Plate Sensing Arrays Using Organosilanes," *Analytical Chemistry*, vol. 75, no. 17, pp. 4360–4367, sep 2003. doi:10.1021/ac0301797

[20] D. Hohlfeld, M. Epmeier, and H. Zappe, "A thermally tunable, silicon-based optical filter," *Sensors and Actuators A: Physical*, vol. 103, no. 1-2, pp. 93–99, jan 2003. doi:10.1016/S0924-4247(02)00320-5

[21] U. Dillner, E. Kessler, S. Poser, V. Baier, and J. Müller, "Low power consumption thermal gas-flow sensor based on thermopiles of highly effective thermoelectric materials," *Sensors and Actuators A: Physical*, vol. 60, no. 1-3, pp. 1–4, may 1997. doi:10.1016/S0924-4247(96)01409-4

[22] K. A. Makinwa and J. H. Huijsing, "A smart wind sensor using thermal sigma-delta modulation techniques," *Sensors and Actuators A: Physical*, vol. 97-98, pp. 15–20, apr 2002. doi:10.1016/S0924-4247(02)00034-1

[23] J. M. Phillips, "Up Close: Nanoscale Science Research Centers," *MRS Bulletin*, vol. 31, no. 01, pp. 45–49, jan 2006. doi:10.1557/mrs2006.5

[24] V. Miralles, A. Huerre, F. Malloggi, and M.-C. Jullien, "A Review of Heating and Temperature Control in Microfluidic Systems: Techniques and Applications," *Diagnostics*, vol. 3, no. 1, pp. 33–67, jan 2013. doi:10.3390/diagnostics3010033

[25] V. T. Fauske, J. Huh, G. Divitini, D. L. Dheeraj, A. M. Munshi, C. Ducati, H. Weman, B.-O. Fimland, and A. T. J. van Helvoort, "In Situ Heat-Induced Replacement of GaAs Nanowires by Au," *Nano Letters*, vol. 16, no. 5, pp. 3051–3057, may 2016. doi:10.1021/acs.nanolett.6b00109

[26] P. Ferreira, K. Mitsuishi, and E. Stach, "In Situ Transmission Electron Microscopy," *MRS Bulletin*, vol. 33, no. 02, pp. 83–90, feb 2008. doi:10.1557/mrs2008.20

[27] J. C. Yang, M. W. Small, R. V. Grieshaber, and R. G. Nuzzo, "Recent developments and applications of electron microscopy to heterogeneous catalysis," *Chemical Society Reviews*, vol. 41, no. 24, p. 8179, 2012. doi:10.1039/c2cs35371g

[28] J. Wu, H. Shan, W. Chen, X. Gu, P. Tao, C. Song, W. Shang, and T. Deng, "In Situ Environmental TEM in Imaging Gas and Liquid Phase Chemical Reactions for Materials Research," *Advanced Materials*, sep 2016. doi:10.1002/adma.201602519

[29] L. Mele, F. Santagata, E. Iervolino, M. Mihailovic, T. Rossi, A. Tran, H. Schellevis, J. Creemer, and P. Sarro, "A molybdenum MEMS microhotplate for high-temperature operation," *Sensors and Actuators A: Physical*, vol. 188, pp. 173–180, dec 2012. doi:10.1016/j.sna.2011.11.023

[30] L. Mele, S. Konings, P. Dona, F. Evertz, C. Mitterbauer, P. Faber, R. Schampers, and J. R. Jinschek, "A MEMS-based heating holder for the direct imaging of simultaneous in-situ heating and biasing experiments in scanning/transmission electron microscopes," *Microscopy Research and Technique*, vol. 79, no. 4, pp. 239–250, apr 2016. doi:10.1002/jemt.22623

[31] L. F. Allard, W. C. Bigelow, M. Jose-Yacaman, D. P. Nackashi, J. Damiano, and S. E. Mick, "A new MEMS-based system for ultra-high-resolution imaging at elevated temperatures," *Microscopy Research and Technique*, vol. 72, no. 3, pp. 208–215, mar 2009. doi:10.1002/jemt.20673

[32] M. Zhang, E. Olson, R. Twesten, J. Wen, L. Allen, I. Robertson, and I. Petrov, "In situ Transmission Electron Microscopy Studies Enabled by Microelectromechanical System Technology," *Journal of Materials Research*, vol. 20, no. 07, pp. 1802–1807, jul 2005. doi:10.1557/JMR.2005.0225

[33] I. Hotovy, V. Rehacek, F. Mika, T. Lalinsky, S. Hascik, G. Vanko, and M. Drzik, "Gallium arsenide suspended microheater for MEMS sensor arrays," *Microsystem Technologies*, vol. 14, no. 4-5, pp. 629–635, apr 2008. doi:10.1007/s00542-007-0470-6

[34] M. A. van Huis, N. P. Young, G. Pandraud, J. F. Creemer, D. Vanmaekelbergh, A. I. Kirkland, and H. W. Zandbergen, "Atomic Imaging of Phase Transitions and Morphology Transformations in Nanocrystals," *Advanced Materials*, vol. 21, no. 48, pp. 4992–4995, dec 2009. doi:10.1002/adma.200902561

[35] F. Lucklum, A. Schwaiger, and B. Jakoby, "High temperature micro-hotplates on porous silicon substrates," in *2013 Transducers and Eurosensors XXVII: The 17th International Conference on Solid-State Sensors, Actuators and Microsystems (TRANSDUCERS and EUROSENSORS XXVII)*. IEEE, jun 2013, pp. 1907–1910. doi:10.1109/Transducers.2013.6627165

[36] N.-K. Song, J.-I. Yun, and S.-K. Joo, "A study on the electrical properties of Pb(Zr, Ti)O3 thin films crystallized by the electrical resistive heating of Pt thin film," *Materials Research Bulletin*, vol. 43, no. 2, pp. 292–296, feb 2008. doi:10.1016/j.materresbull.2007.03.012

[37] R. M. Tiggelaar, J. W. Berenschot, J. H. de Boer, R. G. P. Sanders, J. G. E. Gardeniers, R. E. Oosterbroek, A. van den Berg, and M. C. Elwenspoek, "Fabrication and characterization of high-temperature microreactors with thin film heater and sensor patterns in silicon nitride tubes," *Lab on a Chip*, vol. 5, no. 3, p. 326, 2005. doi:10.1039/b414857f

[38] L. F. Allard, S. H. Overbury, W. C. Bigelow, M. B. Katz, D. P. Nackashi, and J. Damiano, "Novel MEMS-Based Gas-Cell/Heating Specimen Holder Provides Advanced Imaging Capabilities for In Situ Reaction Studies," *Microscopy and Microanalysis*, vol. 18, no. 04, pp. 656–666, aug 2012. doi:10.1017/S1431927612001249

[39] E. Barborini, S. Vinati, M. Leccardi, P. Repetto, G. Bertolini, O. Rorato, L. Lorenzelli, M. Decarli, V. Guarnieri, C. Ducati, and P. Milani, "Batch fabrication of metal oxide sensors on micro-hotplates," *Journal of Micromechanics and Microengineering*, vol. 18, no. 5, p. 055015, may 2008. doi:10.1088/0960-1317/18/5/055015

[40] M. Baroncini, P. Placidi, G. Cardinali, and A. Scorzoni, "Thermal characterization of a microheater for micromachined gas sensors," *Sensors and Actuators A: Physical*, vol. 115, no. 1, pp. 8–14, sep 2004. doi:10.1016/j.sna.2004.03.012

[41] A. Bontempi, L. Thiery, D. Teyssieux, D. Briand, and P. Vairac, "Quantitative thermal microscopy using thermoelectric probe in passive mode," *Review of Scientific Instruments*, vol. 84, no. 10, p. 103703, 2013. doi:10.1063/1.4824069

[42] ——, "DC and AC scanning thermal microscopy using micro-thermoelectric probe," *High Temperatures-High Pressures*, vol. 46, pp. 321–332, 2014. [Online]. Available: https://infoscience.epfl.ch/record/201093

[43] D. Briand, S. Colin, A. Gangadharaiah, E. Vela, P. Dubois, L. Thiery, and N. de Rooij, "Micro-hotplates on polyimide for sensors and actuators," *Sensors and Actuators A: Physical*, vol. 132, no. 1, pp. 317–324, nov 2006. doi:10.1016/j.sna.2006.06.003

[44] D. Briand, S. Heimgartner, M.-A. Gr tillat, B. van der Schoot, and N. F. de Rooij, "Thermal optimization of micro-hotplates that have a silicon island," *Journal of Micromechanics and Microengineering*, vol. 12, no. 6, pp. 971–978, nov 2002. doi:10.1088/0960-1317/12/6/330

[45] J. F. Creemer, S. Helveg, P. J. Kooyman, A. M. Molenbroek, H. W. Zandbergen, and P. M. Sarro, "A MEMS Reactor for Atomic-Scale Microscopy of Nanomaterials Under Industrially Relevant Conditions," *Journal of Microelectromechanical Systems*, vol. 19, no. 2, pp. 254–264, apr 2010. doi:10.1109/JMEMS.2010.2041190

[46] J. F. Creemer, F. Santagata, B. Morana, L. Mele, T. Alan, E. Iervolino, G. Pandraud, and P. M. Sarro, "An all-in-one nanoreactor for high-resolution microscopy on nanomaterials at high pressures," in *2011 IEEE 24th International Conference on Micro Electro Mechanical Systems*. IEEE, jan 2011, pp. 1103–1106. doi:10.1109/MEMSYS.2011.5734622

[47] J. Creemer, D. Briand, H. Zandbergen, W. van der Vlist, C. de Boer, N. de Rooij, and P. Sarro, "Microhotplates with TiN heaters," *Sensors and Actuators A: Physical*, vol. 148, no. 2, pp. 416–421, dec 2008. doi:10.1016/j.sna.2008.08.016

[48] J. Creemer, S. Helveg, G. Hoveling, S. Ullmann, P. Kooyman, A. Molenbroek, H. Zandbergen, and P. Sarro, "MEMS Nanoreactor for Atomic-Resolution Microscopy of Nanomaterials in their Working State," in *2009 IEEE 22nd International Conference on Micro Electro Mechanical Systems*. IEEE, jan 2009, pp. 76–79. doi:10.1109/MEMSYS.2009.4805323

[49] J. Creemer, S. Helveg, G. Hoveling, S. Ullmann, A. Molenbroek, P. Sarro, and H. Zandbergen, "Atomic-scale electron microscopy at ambient pressure," *Ultramicroscopy*, vol. 108, no. 9, pp. 993–998, aug 2008. doi:10.1016/j.ultramic.2008.04.014

[50] A. Götz, I. Gràcia, C. Cané, E. Lora-Tamayo, M. Horrillo, J. Getino, C. García, and J. Gutiérrez, "A micromachined solid state integrated gas sensor for the detection of aromatic hydrocarbons," *Sensors and Actuators B: Chemical*, vol. 44, no. 1-3, pp. 483–487, oct 1997. doi:10.1016/S0925-4005(97)00171-8

[51] S. Hamann, M. Ehmann, S. Thienhaus, A. Savan, and A. Ludwig, "Micro-hotplates for high-throughput thin film processing and in situ phase transformation characterization," *Sensors and Actuators A: Physical*, vol. 147, no. 2, pp. 576–582, oct 2008. doi:10.1016/j.sna.2008.05.007

[52] M. N. Hasan, D. Acharjee, D. Kumar, A. Kumar, and S. Maity, "Simulation of Low Power Heater for Gas Sensing Application," *Procedia Computer Science*, vol. 92, pp. 213–221, 2016. doi:10.1016/j.procs.2016.07.348

[53] W.-J. Hwang, K.-S. Shin, J.-H. Roh, D.-S. Lee, and S.-H. Choa, "Development of Micro-Heaters with Optimized Temperature Compensation Design for Gas Sensors," *Sensors*, vol. 11, no. 12, pp. 2580–2591, mar 2011. doi:10.3390/s110302580

[54] Y. W. Lai, N. Koukourakis, N. C. Gerhardt, M. R. Hofmann, R. Meyer, S. Hamann, M. Ehmann, K. Hackl, E. Darakis, and A. Ludwig, "Integrity of Micro-Hotplates During High-Temperature Operation Monitored by Digital Holographic Microscopy," *Journal of Microelectromechanical Systems*, vol. 19, no. 5, pp. 1175–1179, oct 2010. doi:10.1109/JMEMS.2010.2067442

[55] H.-Y. Lee, S. Moon, S. Park, J. Lee, K.-H. Park, and J. Kim, "Micro-machined resistive micro-heaters for high temperature gas sensing applications," *Electronics Letters*, vol. 44, no. 25, p. 1460, 2008. doi:10.1049/el:20082563

[56] L. Mele, T. Rossi, M. Riccio, E. Iervolino, F. Santagata, A. Irace, G. Breglio, J. Creemer, and P. Sarro, "Electro-thermal analysis of MEMS microhotplates for the optimization of temperature uniformity," *Procedia Engineering*, vol. 25, pp. 387–390, 2011. doi:10.1016/j.proeng.2011.12.096

[57] L. Mele, F. Santagata, E. Iervolino, M. Mihailovic, T. Rossi, A. Tran, H. Schellevis, J. Creemer, and P. Sarro, "Sputtered molybdenum as conductive material for high-temperature microhotplates," in *2011 16th International Solid-State Sensors, Actuators and Microsystems Conference*. IEEE, jun 2011, pp. 2690–2693. doi:10.1109/TRANSDUCERS.2011.5969500

[58] L. Mele, F. Santagata, G. Pandraud, B. Morana, F. D. Tichelaar, J. F. Creemer, and P. M. Sarro, "Wafer-level assembly and sealing of a MEMS nanoreactor for in situ microscopy," *Journal of Micromechanics and Microengineering*, vol. 20, no. 8, p. 085040, aug 2010. doi:10.1088/0960-1317/20/8/085040

[59] B. Morana, F. Santagata, L. Mele, M. Mihailovic, G. Pandraud, J. Creemer, and P. Sarro, "A silicon carbide MEMS microhotplate for nanomaterial characterization in TEM," in *2011 IEEE 24th International Conference on Micro Electro Mechanical Systems*. IEEE, jan 2011, pp. 380–383. doi:10.1109/MEMSYS.2011.5734441

[60] J. Puigcorb, D. Vogel, B. Michel, A. Vil, I. Gr cia, C. Can, and J. R. Morante, "High temperature degradation of Pt/Ti electrodes in micro-hotplate gas sensors," *Journal of Micromechanics and Microengineering*, vol. 13, no. 4, pp. S119–S124, jul 2003. doi:10.1088/0960-1317/13/4/320

[61] F. Udrea, J. Gardner, D. Setiadi, J. Covington, T. Dogaru, C. Lu, and W. Milne, "Design and simulations of SOI CMOS micro-hotplate gas sensors," *Sensors and Actuators B: Chemical*, vol. 78, no. 1-3, pp. 180–190, aug 2001. doi:10.1016/S0925-4005(01)00810-3

[62] A. Y. Ahmed, J. O. Dennis, Mohamad Naufal Mohamad Saad, and W. A. Talah, "Design and simulation of a high temperature MEMS micro-hotplate for application in trace gas detection," in *2008 IEEE International Conference on Semiconductor Electronics*. Johor Bahru: IEEE, nov 2008, pp. 153–157. doi:10.1109/SMELEC.2008.4770297

[63] J. C. Belmonte, J. Puigcorbé, J. Arbiol, A. Vilà, J. Morante, N. Sabaté, I. Gràcia, and C. Cané, "High-temperature low-power performing micromachined suspended micro-hotplate for gas sensing applications," *Sensors and Actuators B: Chemical*, vol. 114, no. 2, pp. 826–835, apr 2006. doi:10.1016/j.snb.2005.07.057

[64] G.-S. Chung and J.-M. Jeong, "Fabrication of micro heaters on polycrystalline 3C-SiC suspended membranes for gas sensors and their characteristics," *Microelectronic Engineering*, vol. 87, no. 11, pp. 2348–2352, nov 2010. doi:10.1016/j.mee.2010.04.005

[65] D. DeVoe, "Thermal issues in MEMS and microscale systems," *IEEE Transactions on Components and Packaging Technologies*, vol. 25, no. 4, pp. 576–583, dec 2002. doi:10.1109/TCAPT.2003.809110

[66] V. K. Khanna, M. Prasad, V. K. Dwivedi, C. Shekhar, A. C. Pankaj, and J. Basu, "Design and electro-thermal simulation of a polysilicon microheater on a suspended membrane for use in gas sensing," *Indian Journal of Pure and Applied Physics*, vol. 45, no. 4, pp. 332–335, 2007. [Online]. Available: http://nopr.niscair.res.in/bitstream/123456789/2333/1/IJPAP45(4)332-335.pdf

[67] M. Prasad, D. S. Arya, and V. K. Khanna, "Fabrication and reliability study of a double spiral platinum-based MEMS hotplate," *Journal of Micro/Nanolithography, MEMS, and MOEMS*, vol. 14, no. 2, p. 025003, jun 2015. doi:10.1117/1.JMM.14.2.025003

[68] F. Samaeifar, H. Hajghassem, A. Afifi, and H. Abdollahi, "Implementation of high-performance MEMS platinum micro-hotplate," *Sensor Review*, vol. 35, no. 1, pp. 116–124, jan 2015. doi:10.1108/SR-05-2014-654

[69] O. Sidek, M. Z. Ishak, M. A. Khalid, M. Z. Abu Bakar, and M. A. Miskam, "Effect of heater geometry on the high temperature distribution on a MEMS micro-hotplate," in *2011 3rd Asia Symposium on Quality Electronic Design (ASQED)*. IEEE, jul 2011, pp. 100–104. doi:10.1109/ASQED.2011.6111709

[70] J. Spannhake, A. Helwig, G. Müller, G. Faglia, G. Sberveglieri, T. Doll, T. Wassner, and M. Eickhoff, "SnO2:Sb – A new material for high-temperature MEMS heater applications: Performance and limitations," *Sensors and Actuators B: Chemical*, vol. 124, no. 2, pp. 421–428, jun 2007. doi:10.1016/j.snb.2007.01.004

[71] J. Spannhake, O. Schulz, A. Helwig, A. Krenkow, G. Müller, and T. Doll, "High-temperature MEMS Heater Platforms: Long-term Performance of Metal and Semiconductor Heater Materials," *Sensors*, vol. 6, no. 4, pp. 405–419, apr 2006. doi:10.3390/s6040405

[72] G. Wiche, A. Berns, H. Steffes, and E. Obermeier, "Thermal analysis of silicon carbide based micro hotplates for metal oxide gas sensors," *Sensors and Actuators A: Physical*, vol. 123-124, pp. 12–17, sep 2005. doi:10.1016/j.sna.2005.03.028

[73] G. Yan, Z. Tang, P. C. Chan, J. K. Sin, I.-M. Hsing, and Y. Wang, "An experimental study on high-temperature metallization for micro-hotplate-based integrated gas sensors," *Sensors and Actuators B: Chemical*, vol. 86, no. 1, pp. 1–11, aug 2002. doi:10.1016/S0925-4005(02)00070-9

[74] R. Zhang, Y. Gu, D. Zhu, J. Hao, and Z. Tang, "Thermal measurement and analysis of micro hotplate array using thermography," *Sensors and Actuators A: Physical*, vol. 100, no. 2-3, pp. 144–152, sep 2002. doi:10.1016/S0924-4247(02)00061-4

[75] M. R. Abel, T. L. Wright, W. P. King, and S. Graham, "Thermal Metrology of Silicon Microstructures Using Raman Spectroscopy," *IEEE Transactions on Components and Packaging Technologies*, vol. 30, no. 2, pp. 200–208, jun 2007. doi:10.1109/TCAPT.2007.897993

[76] J. Lee and W. P. King, "Microcantilever hotplates: Design, fabrication, and characterization," *Sensors and Actuators A: Physical*, vol. 136, no. 1, pp. 291–298, may 2007. doi:10.1016/j.sna.2006.10.051

[77] H. Ma, W. Wang, and X. Liu, "Methane detection with high temperature all-silicon microheater," in *IEEE SENSORS 2014 Proceedings*. IEEE, nov 2014, pp. 186–189. doi:10.1109/ICSENS.2014.6984964

[78] B. A. Nelson and W. P. King, "Thermal Calibration of Heated Silicon Atomic Force Microscope Cantilevers," in *TRANSDUCERS 2007 - 2007 International Solid-State Sensors, Actuators and Microsystems Conference*. IEEE, 2007, pp. 607–610. doi:10.1109/SENSOR.2007.4300203

[79] A. N. Nordin, I. Voiculescu, and M. Zaghloul, "Micro-hotplate based temperature stabilization system for CMOS SAW resonators," *Microsystem Technologies*, vol. 15, no. 8, pp. 1187–1193, aug 2009. doi:10.1007/s00542-009-0786-5

[80] N. L. Privorotskaya and W. P. King, "Silicon microcantilever hotplates with high temperature uniformity," *Sensors and Actuators, A: Physical*, vol. 152, no. 2, pp. 160–167, 2009. doi:10.1016/j.sna.2009.03.020

[81] R. Triantafyllopoulou, S. Chatzandroulis, C. Tsamis, and A. Tserepi, "Alternative micro-hotplate design for low power sensor arrays," *Microelectronic Engineering*, vol. 83, no. 4-9, pp. 1189–1191, apr 2006. doi:10.1016/j.mee.2006.01.224

[82] S. Franssila, *Introduction to Microfabrication*, 2nd ed. Chichester, UK: John Wiley and Sons, Ltd, sep 2010. doi:10.1002/9781119990413

[83] J. Laconte, C. Dupont, D. Flandre, and J.-P. Raskin, "SOI CMOS Compatible Low-Power Microheater Optimization for the Fabrication of Smart Gas Sensors," *IEEE Sensors Journal*, vol. 4, no. 5, pp. 670–680, oct 2004. doi:10.1109/JSEN.2004.833516

[84] M. Mecklenburg, W. A. Hubbard, E. R. White, R. Dhall, S. B. Cronin, S. Aloni, and B. C. Regan, "Nanoscale temperature mapping in operating microelectronic devices," *Science*, vol. 347, no. 6222, pp. 629–632, feb 2015. doi:10.1126/science.aaa2433

[85] P. Ruther, M. Herrscher, and O. Paul, "A micro differential thermal analysis (μDTA) system," in *17th IEEE International Conference on Micro Electro Mechanical Systems. Maastricht MEMS 2004 Technical Digest*. IEEE, 2004, pp. 165–168. doi:10.1109/MEMS.2004.1290548

[86] X. Yi, J. Lai, H. Liang, and X. Zhai, "Fabrication of a MEMS micro-hotplate," *Journal of Physics: Conference Series*, vol. 276, p. 012098, feb 2011. doi:10.1088/1742-6596/276/1/012098

[87] W. K. Schomburg, "Membranes," in *Introduction to Microsystem Design*, ser. RWTHedition. Berlin, Heidelberg: Springer Berlin Heidelberg, 2011, ch. 6, pp. 29–52. doi:10.1007/978-3-642-19489-4_6

[88] J. Vlassak and W. Nix, "A new bulge test technique for the determination of Young's modulus and Poisson's ratio of thin films," *Journal of Materials Research*, vol. 7, no. 12, pp. 3242–3249, dec 1992. doi:10.1557/JMR.1992.3242

[89] J. Shackelford and W. Alexander, *CRC Materials Science and Engineering Handbook, Third Edition*, 3rd ed. Boca Raton, Florida: CRC Press, dec 2000. doi:10.1201/9781420038408

[90] P. A. Tipler and G. Mosca, *Physics for Scientists and Engineers*, 6th ed. New York: W.H. Freeman and Company, 2008. [Online]. Available: http://www.macmillanlearning.com/Catalog/Product.aspx?isbn=0716789647

[91] T. L. Bergman, A. S. Lavine, F. P. Incropera, and D. P. DeWitt, *Fundamentals of Heat and Mass Transfer*, 7th ed. Hoboken, NJ: John Wiley and Sons, Inc, 2011. [Online]. Available: http://eu.wiley.com/WileyCDA/WileyTitle/productCd-EHEP001810.html

[92] L. Janssen and M. Warmoeskerken, *Transport Phenomena Data Companion*. Delft: VSSD, 2006. [Online]. Available: http://www.vssd.nl/hlf/c017.htm

[93] ASM International Handbook Committee, Ed., *ASM Handbook Volume 2: Properties and Selection: Nonferrous Alloys and Special-Purpose Materials*. ASM International, 1990. [Online]. Available: http://products.asminternational.org/hbk/index.jsp

[94] R. A. Serway and J. W. Jewett, *Physics for Scientists and Engineers*, 6th ed. Brooks Cole, 2003. [Online]. Available: http://www.cengage.com/cgi-wadsworth/course_products_wp.pl?fid=M20b&product_isbn_issn=0534408427

[95] E. a. Bel'skaya and E. Y. Kulyamina, "Electrical resistivity of titanium in the temperature range from 290 to 1800 K," *High Temperature*, vol. 45, no. 6, pp. 785–796, dec 2007. doi:10.1134/S0018151X07060090

[96] E. Naimon, W. Weston, and H. Ledbetter, "Elastic properties of two titanium alloys at low temperatures," *Cryogenics*, vol. 14, no. 5, pp. 246–249, may 1974. doi:10.1016/0011-2275(74)90223-9

[97] N. Kumar, K. Pourrezaei, M. Fissel, T. BegleyB Lee, and E. Douglas, "Growth and properties of radio frequency reactively sputtered titanium nitride thin films," *Journal of Vacuum Science and Technology A: Vacuum, Surfaces, and Films*, vol. 5, no. 4, p. 1778, jul 1987. doi:10.1116/1.574494

[98] Y. Touloukian, R. Powell, C. Ho, and P. Klemens, *Thermophysical Properties of Matter - The TPRC Data Series. Volume 2. Thermal Conductivity - Nonmetallic Solids*. New York: Plenum Publishing Corporation, 1971. [Online]. Available: http://oai.dtic.mil/oai/oai?verb=getRecord&metadataPrefix=html&identifier=ADA951936

[99] Y. S. Touloukian, R. K. Kirby, E. R. Taylor, and T. Y. R. Lee, *Thermophysical Properties of Matter - The TPRC Data Series. Volume 13. Thermal Expansion - Nonmetallic Solids*. New York: Plenum Publishing Corporation, 1977. [Online]. Available: http://oai.dtic.mil/oai/oai?verb=getRecord&metadataPrefix=html&identifier=ADA129116

[100] G. Benn, "Design of a silicon carbide micro-hotplate geometry for high temperature chemical sensing," Master Thesis, Massachusetts Institute of Technology, 2000. [Online]. Available: http://hdl.handle.net/1721.1/17535

[101] A. A. Kovalevskii, A. V. Dolbik, and S. N. Voitekh, "Effect of doping on the temperature coefficient of resistance of polysilicon films," *Russian Microelectronics*, vol. 36, no. 3, pp. 153–158, may 2007. doi:10.1134/S1063739707030031

[102] M. Ashby, H. Shercliff, and D. Cebon, *Materials: Engineering, Science, Processing and Design*, 3rd ed. Oxford, UK: Elsevier Ltd, 2014. [Online]. Available: http://store.elsevier.com/product.jsp?locale=en_EU&isbn=9780080977737

[103] W. N. Sharpe, J. Pulskamp, D. S. Gianola, C. Eberl, R. G. Polcawich, and R. J. Thompson, "Strain Measurements of Silicon Dioxide Microspecimens by Digital Imaging Processing," *Experimental Mechanics*, vol. 47, no. 5, pp. 649–658, sep 2007. doi:10.1007/s11340-006-9010-z

[104] Q. Zhou, A. Sussman, J. Chang, J. Dong, A. Zettl, and W. Mickelson, "Fast response integrated MEMS microheaters for ultra low power gas detection," *Sensors and Actuators A: Physical*, vol. 223, pp. 67–75, mar 2015. doi:10.1016/j.sna.2014.12.005

[105] D. Whitehouse, *Handbook of Surface and Nanometrology, Second Edition*, 2nd ed. Boca Raton, Florida: CRC Press, 2010. [Online]. Available: https://www.crcpress.com/Handbook-of-Surface-and-Nanometrology-Second-Edition/Whitehouse/p/book/9781420082029

[106] J. M. Olson, "Analysis of LPCVD process conditions for the deposition of low stress silicon nitride. Part I: preliminary LPCVD experiments," *Materials Science in Semiconductor Processing*, vol. 5, no. 1, pp. 51–60, feb 2002. doi:10.1016/S1369-8001(02)00058-6

[107] A. Kaushik, H. Kahn, and A. Heuer, "Wafer-level mechanical characterization of silicon nitride MEMS," *Journal of Microelectromechanical Systems*, vol. 14, no. 2, pp. 359–367, apr 2005. doi:10.1109/JMEMS.2004.839315

[108] A. Tarraf, J. Daleiden, S. Irmer, D. Prasai, and H. Hillmer, "Stress investigation of PECVD dielectric layers for advanced optical MEMS," *Journal of Micromechanics and Microengineering*, vol. 14, no. 3, pp. 317–323, mar 2004. doi:10.1088/0960-1317/14/3/001

[109] C. A. Zorman, R. C. Roberts, and L. Chen, "Additive Processes for Semiconductors and Dielectric Materials," in *MEMS Materials and Processes Handbook*. Springer US, 2011, pp. 37–136. doi:10.1007/978-0-387-47318-5_2

[110] R. Ghodssi and P. Lin, Eds., *MEMS Materials and Processes Handbook*, ser. MEMS Reference Shelf. Boston, MA: Springer US, 2011, vol. 1. doi:10.1007/978-0-387-47318-5

[111] G. Srivastava, "Lattice Thermal Conduction Mechanism in Solids," in *High Thermal Conductivity Materials*. New York: Springer-Verlag, 2006, pp. 1–35. doi:10.1007/0-387-25100-6_1

[112] L. Zeng, K. C. Collins, Y. Hu, M. N. Luckyanova, A. A. Maznev, S. Huberman, V. Chiloyan, J. Zhou, X. Huang, K. A. Nelson, and G. Chen, "Measuring Phonon Mean Free Path Distributions by Probing Quasiballistic Phonon Transport in Grating Nanostructures," *Scientific Reports*, vol. 5, no. August, p. 17131, nov 2015. doi:10.1038/srep17131

[113] S. R. Mirmira and L. S. Fletcher, "Review of the Thermal Conductivity of Thin Films," *Journal of Thermophysics and Heat Transfer*, vol. 12, no. 2, pp. 121–131, apr 1998. doi:10.2514/2.6321

[114] D. M. Bhusari, C. W. Teng, K. H. Chen, S. L. Wei, and L. C. Chen, "Traveling wave method for measurement of thermal conductivity of thin films," *Review of Scientific Instruments*, vol. 68, no. 11, p. 4180, 1997. doi:10.1063/1.1148364

[115] D. Briand, A. Krauss, B. van der Schoot, U. Weimar, N. Barsan, W. Göpel, and N. de Rooij, "Design and fabrication of high-temperature micro-hotplates for drop-coated gas sensors," *Sensors and Actuators B: Chemical*, vol. 68, no. 1-3, pp. 223–233, aug 2000. doi:10.1016/S0925-4005(00)00433-0

[116] S. Edalatpour and M. Francoeur, "Size effect on the emissivity of thin films," *Journal of Quantitative Spectroscopy and Radiative Transfer*, vol. 118, pp. 75–85, mar 2013. doi:10.1016/j.jqsrt.2012.12.012

[117] A. Hofer, J. Schlacher, J. Keckes, J. Winkler, and C. Mitterer, "Sputtered molybdenum films: Structure and property evolution with film thickness," *Vacuum*, vol. 99, pp. 149–152, jan 2014. doi:10.1016/j.vacuum.2013.05.018

[118] D. Gall, "Electron mean free path in elemental metals," *Journal of Applied Physics*, vol. 119, no. 8, p. 085101, feb 2016. doi:10.1063/1.4942216

[119] F. Lacy, "Developing a theoretical relationship between electrical resistivity, temperature, and film thickness for conductors," *Nanoscale Research Letters*, vol. 6, no. 1, p. 636, 2011. doi:10.1186/1556-276X-6-636

[120] J. R. Hook and H. E. Hall, *Solid State Physics*, 2nd ed. John Wiley and Sons Ltd, 1991. [Online]. Available: http://eu.wiley.com/WileyCDA/WileyTitle/productCd-0471928054.html

[121] Y. V. Polezhaev, "THERMAL CONDUCTIVITY," in *A-to-Z Guide to Thermodynamics, Heat and Mass Transfer, and Fluids Engineering*. Begellhouse, 2011. doi:10.1615/AtoZ.t.thermal_conductivity

[122] Y. S. Touloukian, R. W. Powell, C. Y. Ho, and P. G. Klemens, *Thermophysical Properties of Matter - The TPRC Data Series. Volume 1. Thermal Conductivity - Metallic Elements and Alloys.* New York: Plenum Publishing Corporation, 1970. [Online]. Available: http://oai.dtic.mil/oai/oai?verb=getRecord&metadataPrefix=html&identifier=ADA951935

[123] Y. S. Touloukian and E. H. Buyco, *Thermophysical Properties of Matter - The TPRC Data Series. Volume 4. Specific Heat - Metallic Elements and Alloys.* New York: Plenum Publishing Corporation, 1971. [Online]. Available: http://oai.dtic.mil/oai/oai?verb=getRecord&metadataPrefix=html&identifier=ADA951938

[124] ——, *Thermophysical Properties of Matter - The TPRC Data Series. Volume 5. Specific Heat - Nonmetallic Solids.* New York: Plenum Publishing Corporation, 1970. [Online]. Available: http://oai.dtic.mil/oai/oai?verb=getRecord&metadataPrefix=html&identifier=ADA951939

[125] Y. S. Touloukian and D. P. DeWitt, *Thermophysical Properties of Matter - The TPRC Data Series. Volume 7. Thermal Radiative Properties - Metallic Elements and Alloys.* New York: Plenum Publishing Corporation, 1970. [Online]. Available: http://oai.dtic.mil/oai/oai?verb=getRecord&metadataPrefix=html&identifier=ADA951941

[126] ——, *Thermophysical Properties of Matter - The TPRC Data Series. Volume 8. Thermal Radiative Properties - Nonmetallic Solids.* New York: Plenum Publishing Corporation, 1972. [Online]. Available: http://oai.dtic.mil/oai/oai?verb=getRecord&metadataPrefix=html&identifier=ADA951942

[127] Y. S. Touloukian, R. K. Kirby, R. E. Taylor, and P. D. Desai, *Thermophysical Properties of Matter - The TPRC Data Series. Volume 12. Thermal Expansion Metallic Elements and Alloys.* New York: Plenum Publishing Corporation, 1975. [Online]. Available: http://oai.dtic.mil/oai/oai?verb=getRecord&metadataPrefix=html&identifier=ADA129115

[128] N. Ravindra, S. Abedrabbo, Wei Chen, F. Tong, A. Nanda, and A. Speranza, "Temperature-dependent emissivity of silicon-related materials and structures," *IEEE Transactions on Semiconductor Manufacturing*, vol. 11, no. 1, pp. 30–39, 1998. doi:10.1109/66.661282

[129] P. Y. Wong, "Coherent thermal radiation effects on temperature-dependent emissivity of thin-film structures on optically thick substrates," *Optical Engineering*, vol. 34, no. 6, p. 1776, jun 1995. doi:10.1117/12.203137

[130] A. Pike and J. W. Gardner, "Thermal modelling and characterisation of micropower chemoresistive silicon sensors," *Sensors and Actuators B: Chemical*, vol. 45, no. 1, pp. 19–26, nov 1997. doi:10.1016/S0925-4005(97)00261-X

[131] C. Rossi, P. Temple-Boyer, and D. Estève, "Realization and performance of thin SiO2/SiNx membrane for microheater applications," *Sensors and Actuators A: Physical*, vol. 64, no. 3, pp. 241–245, jan 1998. doi:10.1016/S0924-4247(97)01627-0

[132] A. Wisitsoraat, A. Tuantranont, and T. Lomas, "Design and Simulation of Electro-fabricated MEMS Microhotplate for Gas Sensor Applications," *Journal of Physics: Conference Series*, vol. 34, pp. 643–649, apr 2006. doi:10.1088/1742-6596/34/1/106

[133] P. Giesen and E. Folgering, "Design guidelines for thermal stability in optomechanical instruments," in *Proceedings of SPIE*, A. E. Hatheway, Ed., vol. 5176, oct 2003, p. 126. doi:10.1117/12.510285

[134] M. Yajima, N. Yoshida, S. Kajita, M. Tokitani, T. Baba, and N. Ohno, "In situ observation of structural change of nanostructured tungsten during annealing," *Journal of Nuclear Materials*, vol. 449, no. 1-3, pp. 9–14, jun 2014. doi:10.1016/j.jnucmat.2014.02.027

[135] M. Duchamp, Q. Xu, and R. E. Dunin-Borkowski, "Convenient Preparation of High-Quality Specimens for Annealing Experiments in the Transmission Electron Microscope," *Microscopy and Microanalysis*, vol. 20, no. 06, pp. 1638–1645, dec 2014. doi:10.1017/S1431927614013476

[136] D. Gardini, J. M. Christensen, C. D. Damsgaard, A. D. Jensen, and J. B. Wagner, "Visualizing the mobility of silver during catalytic soot oxidation," *Applied Catalysis B: Environmental*, vol. 183, pp. 28–36, apr 2016. doi:10.1016/j.apcatb.2015.10.029

[137] F. Niekiel, S. M. Kraschewski, J. Müller, B. Butz, and E. Spiecker, "Local Temperature Measurement in TEM by Parallel Beam Electron Diffraction," *Ultramicroscopy*, dec 2016. doi:10.1016/j.ultramic.2016.11.028

[138] M. Picher, S. Mazzucco, S. Blankenship, and R. Sharma, "Vibrational and optical spectroscopies integrated with environmental transmission electron microscopy," *Ultramicroscopy*, vol. 150, pp. 10–15, mar 2015. doi:10.1016/j.ultramic.2014.11.023

[139] P. Fürjes, G. Bognár, and I. Bársony, "Powerful tools for thermal characterisation of MEMS," *Sensors and Actuators B: Chemical*, vol. 120, no. 1, pp. 270–277, dec 2006. doi:10.1016/j.snb.2006.02.041

[140] G. Sberveglieri, W. Hellmich, and G. Müller, "Silicon hotplates for metal oxide gas sensor elements," *Microsystem Technologies*, vol. 3, no. 4, pp. 183–190, aug 1997. doi:10.1007/s005420050078

[141] Y. Yao, K. K. Fu, C. Yan, J. Dai, Y. Chen, Y. Wang, B. Zhang, E. Hitz, and L. Hu, "Three-Dimensional Printable High-Temperature and High-Rate Heaters," *ACS Nano*, vol. 10, no. 5, pp. 5272–5279, may 2016. doi:10.1021/acsnano.6b01059

[142] D. Sinar, G. K. Knopf, S. Nikumb, and A. Andrushchenko, "Laser micromachining of oxygen reduced graphene-oxide films," in *Proceedings of the SPIE - The International Society for Optical Engineering*, M. A. Maher and P. J. Resnick, Eds., mar 2014, p. 89730K. doi:10.1117/12.2038423

[143] L. E. Delle, R. Lanche, J. K.-Y. Law, M. Weil, X. T. Vu, P. Wagner, and S. Ingebrandt, "Reduced graphene oxide micropatterns as an interface for adherent cells," *physica status solidi (a)*, vol. 210, no. 5, pp. 975–982, may 2013. doi:10.1002/pssa.201200864

[144] S. Giorgio, S. Sao Joao, S. Nitsche, D. Chaudanson, G. Sitja, and C. Henry, "Environmental electron microscopy (ETEM) for catalysts with a closed E-cell with carbon windows," *Ultramicroscopy*, vol. 106, no. 6, pp. 503–507, apr 2006. doi:10.1016/j.ultramic.2006.01.006

[145] T. Yaguchi, M. Suzuki, A. Watabe, Y. Nagakubo, K. Ueda, and T. Kamino, "Development of a high temperature-atmospheric pressure environmental cell for high-resolution TEM," *Journal of Electron Microscopy*, vol. 60, no. 3, pp. 217–225, jun 2011. doi:10.1093/jmicro/dfr011

[146] B. J. Kirby, *Micro- and Nanoscale Fluid Mechanics: Transport in Microfluidic Devices*, 1st ed. Cambridge: Cambridge University press, 2010. [Online]. Available: www.cambridge.org/9780521119030

[147] J. C. Harley, Y. Huang, H. H. Bau, and J. N. Zemel, "Gas flow in micro-channels," *Journal of Fluid Mechanics*, vol. 284, p. 257, feb 1995. doi:10.1017/S0022112095000358

[148] J. Pan, P. Lin, F. Maseeh, and S. Senturia, "Verification of FEM analysis of load-deflection methods for measuring mechanical properties of thin films," in *IEEE 4th Technical Digest on Solid-State Sensor and Actuator Workshop.* IEEE, 1990, pp. 70–73. doi:10.1109/SOLSEN.1990.109823

[149] V. Balaji and K. N. Bhat, "A Comparison of Burst Strength and Linearity of Pressure Sensors having Thin Diaphragms of Different Shapes," *JOURNAL OF ISSS*, vol. 2, no. 2, pp. 18–26, 2013. [Online]. Available: http://www.isssonline.in/journal-isss/journalarchives.html#223

[150] R. Zhang, "Mechanical characterization of thin films with application to ferroelectrics," Ph.D., California Institute of Technology, 2006. [Online]. Available: http://resolver.caltech.edu/CaltechETD:etd-01312006-170959

[151] W. Sauter, "Thin Film Mechanics Bulging and Stretching," PhD Dissertation, University of Vermont, 1999.

[152] W. D. Nix, "Mechanical properties of thin films," Class notes, Stanford University, 2005. [Online]. Available: http://imechanica.org/files/353ClassNotes2005.pdf

[153] T. Yokosawa, T. Alan, G. Pandraud, B. Dam, and H. Zandbergen, "In-situ TEM on (de)hydrogenation of Pd at 0.5–4.5bar hydrogen pressure and 20–400°C," *Ultramicroscopy*, vol. 112, no. 1, pp. 47–52, jan 2012. doi:10.1016/j.ultramic.2011.10.010

[154] H. H. Pérez Garza, E. W. Kievit, G. F. Schneider, and U. Staufer, "Controlled, Reversible, and Nondestructive Generation of Uniaxial Extreme Strains (>10%) in Graphene," *Nano Letters*, vol. 14, no. 7, pp. 4107–4113, jul 2014. doi:10.1021/nl5016848

[155] D. Schroeder, *An Introduction to Thermal Physics*, 1st ed. Essex: Pearson, 2014. [Online]. Available: http://www.pearsoned.co.uk/bookshop/detail.asp?item=100000000553692

[156] J. P. M. Trusler, "MEAN FREE PATH," in *A-to-Z Guide to Thermodynamics, Heat and Mass Transfer, and Fluids Engineering*. Begellhouse, 2011. doi:10.1615/AtoZ.m.mean_free_path

[157] Y. S. Touloukian, P. E. Liley, and S. C. Saxena, *Thermophysical Properties of Matter - The TPRC Data Series. Volume 3. Thermal Conductivity - Nonmetallic Liquids and Gases*. New York: Plenum Publishing Corporation, 1970. [Online]. Available: http://oai.dtic.mil/oai/oai?verb=getRecord&metadataPrefix=html&identifier=ADA951937

[158] N. Vargaftik, L. Filippov, A. Tarzimanov, and E. Totskii, *Handbook of Thermal Conductivity of Liquids and Gases*. CRC Press, 1993. [Online]. Available: https://www.crcpress.com/Handbook-of-Thermal-Conductivity-of-Liquids-and-Gases/Vargaftik/p/book/9780849393457

[159] Dortmund Data Bank, "Thermal Conductivity of Nitrogen." [Online]. Available: http://www.ddbst.com/en/EED/PCP/TCN_C1056.php

[160] N. B. Vargaftik and L. V. Yakush, "Temperature dependence of thermal conductivity of helium," *Journal of Engineering Physics*, vol. 32, no. 5, pp. 530–532, may 1977. doi:10.1007/BF00860600

[161] C. Minter, "Effect of pressure on the thermal conductivity of a gas," U.S. Naval Research Laboratory, Washington D.C., Tech. Rep., 1963. [Online]. Available: http://www.dtic.mil/dtic/tr/fulltext/u2/298997.pdf

[162] S. Jennings, "The mean free path in air," *Journal of Aerosol Science*, vol. 19, no. 2, pp. 159–166, apr 1988. doi:10.1016/0021-8502(88)90219-4

[163] E. Litovsky, M. Shapiro, and A. Shavit, "Gas Pressure and Temperature Dependences of Thermal Conductivity of Porous Ceramic Materials: Part 2, Refractories and Ceramics with Porosity Exceeding 30the American Ceramic Society, vol. 79, no. 5, pp. 1366–1376, may 1996. doi:10.1111/j.1151-2916.1996.tb08598.x

[164] J. K. Robertson and K. D. Wise, "Modeling a microfluidic system using Knudsen's empirical equation for flow in the transition regime," *Journal of Vacuum Science & Technology A: Vacuum, Surfaces, and Films*, vol. 19, no. 1, pp. 358–364, jan 2001. doi:10.1116/1.1335837

[165] V. Félix, Y. Jannot, and A. Degiovanni, "A thermal porosimetry method to estimate pore size distribution in highly porous insulating materials." *The Review of scientific instruments*, vol. 83, no. 5, p. 054903, may 2012. doi:10.1063/1.4704842

[166] G. L. Shires, "PECLET NUMBER," in *A-to-Z Guide to Thermodynamics, Heat and Mass Transfer, and Fluids Engineering*. Begellhouse, 2011. doi:10.1615/AtoZ.p.peclet_number

[167] F. P. Incropera, D. P. DeWitt, T. L. Bergman, and A. S. Lavine, *Fundamentals of Heat and Mass Transfer*, 6th ed. Hoboken, NJ: John Wiley and Sons, Inc, 2007.

[168] I. L. Mostinsky, "DIFFUSION COEFFICIENT," in *A-to-Z Guide to Thermodynamics, Heat and Mass Transfer, and Fluids Engineering*. Begellhouse, 2011. doi:10.1615/AtoZ.d.diffusion_coefficient

[169] T. S. Ursell, "The Diffusion Equation: A Multi- dimensional Tutorial," California Institute of Technology, Pasadena, Tech. Rep., 2013.

[170] B. Michen, C. Geers, D. Vanhecke, C. Endes, B. Rothen-Rutishauser, S. Balog, and A. Petri-Fink, "Avoiding drying-artifacts in transmission electron microscopy: Characterizing the size and colloidal state of nanoparticles," *Scientific Reports*, vol. 5, no. 1, p. 9793, sep 2015. doi:10.1038/srep09793

[171] J. Orloff, *Handbook of Charged Particle Optics*, 2nd ed. Boca Raton, Florida: CRC Press, 2008. [Online]. Available: https://www.crcpress.com/Handbook-of-Charged-Particle-Optics-Second-Edition/Orloff/p/book/9781420045543

[172] S. Middelhoek, A. A. Bellekom, U. Dauderstadt, P. J. French, S. R. i. t. Hout, W. Kindt, F. Riedijk, and M. J. Vellekoop, "Silicon sensors," *Measurement Science and Technology*, vol. 6, no. 12, pp. 1641–1658, dec 1995. doi:10.1088/0957-0233/6/12/001

[173] X. Wang, N. Wang, R.-B. Chen, H.-S. San, and X.-Y. Chen, "3D-FEM electrical–thermal–mechanical analysis and experiment of Si-based MEMS infrared emitters," *Journal of Micromechanics and Microengineering*, vol. 26, no. 11, p. 115007, nov 2016. doi:10.1088/0960-1317/26/11/115007

[174] R. T. Blunt, "White Light Interferometry – a production worthy technique for measuring surface roughness on semiconductor wafers," *CS MANTECH Conference*, vol. 44, no. 0, pp. 59–62, 2006. [Online]. Available: http://csmantech.org/OldSite/Digests/2006/2006Digests/4B.pdf

[175] E. Hecht, *Optics*, 4th ed. San Francisco: Addison-Wesley, 2002.

[176] BrukerNanoSurfaces, "An Introduction to Non Destructive 3D Surface Texture Studies using 3D Optical Microscopy," 2017. [Online]. Available: https://youtu.be/FW0ijgckfRM?t=17m9s

[177] S. Aurantiaca, "Figure 3. White light interferometric microscope," 2012. [Online]. Available: https://en.wikipedia.org/wiki/White_light_scanner#/media/File:White_light_interferometric_microscope.gif

[178] M. Kuball and J. W. Pomeroy, "A Review of Raman Thermography for Electronic and Opto-Electronic Device Measurement With Submicron Spatial and Nanosecond Temporal Resolution," *IEEE Transactions on Device and Materials Reliability*, vol. 16, no. 4, pp. 667–684, dec 2016. doi:10.1109/TDMR.2016.2617458

[179] T. R. Hart, R. L. Aggarwal, and B. Lax, "Temperature Dependence of Raman Scattering in Silicon," *Physical Review B*, vol. 1, no. 2, pp. 638–642, jan 1970. doi:10.1103/PhysRevB.1.638

[180] Z. Su, J. Sha, G. Pan, J. Liu, D. Yang, C. Dickinson, and W. Zhou, "Temperature-Dependent Raman Scattering of Silicon Nanowires," *The Journal of Physical Chemistry B*, vol. 110, no. 3, pp. 1229–1234, jan 2006. doi:10.1021/jp055869o

[181] M. R. Abel, S. Graham, J. R. Serrano, S. P. Kearney, and L. M. Phinney, "Raman Thermometry of Polysilicon Microelectro- mechanical Systems in the Presence of an Evolving Stress," *Journal of Heat Transfer*, vol. 129, no. 3, p. 329, 2007. doi:10.1115/1.2409996

[182] S. Thyageswaran, "Developments in Thermometry from 1984 to 2011: A Review," *Recent Patents on Mechanical Engineeringe*, vol. 5, no. 1, pp. 4–44, jan 2012. doi:10.2174/2212797611205010004

[183] M. Balkanski, R. F. Wallis, and E. Haro, "Anharmonic effects in light scattering due to optical phonons in silicon," *Physical Review B*, vol. 28, no. 4, pp. 1928–1934, aug 1983. doi:10.1103/PhysRevB.28.1928

[184] The Prashant Kamat Laboratory, "Spectroscopic Characterization," 2012. [Online]. Available: https://www3.nd.edu/~kamatlab/facilities_spectroscopy.html#Pos7

[185] Moxfyre, "Raman energy levels," 2009. [Online]. Available: https://commons.wikimedia.org/w/index.php?curid=7845122

[186] H. Adhikari, A. F. Marshall, I. A. Goldthorpe, C. E. D. Chidsey, and P. C. McIntyre, "Metastability of Au-Ge Liquid Nanocatalysts: Ge Vapor-Liquid-Solid Nanowire Growth Far below the Bulk Eutectic Temperature," *ACS Nano*, vol. 1, no. 5, pp. 415–422, dec 2007. doi:10.1021/nn7001486

[187] F. L. Dorman, E. B. Overton, J. J. Whiting, J. W. Cochran, and J. Gardea-Torresdey, "Gas Chromatography," *Analytical Chemistry*, vol. 80, no. 12, pp. 4487–4497, jun 2008. doi:10.1021/ac800714x

[188] J. Očenášek and J. Voldřich, "Raman thermometry: Effective temperature of the nonuniform temperature field induced by a Gaussian laser," *Journal of Applied Physics*, vol. 118, no. 23, p. 233104, dec 2015. doi:10.1063/1.4937904

[189] J. J. Swab, A. A. Wereszczak, J. Tice, R. Caspe, R. H. Kraft, and J. W. Adams, "Mechanical and Thermal Properties of Advanced Ceramics for Gun Barrel Applications," *Materials Research*, no. February, 2005. [Online]. Available: http://www.arl.army.mil/arlreports/2005/ARL-TR-3417.pdf

[190] J. Winkelmann, "Diffusion of helium (1); nitrogen (2)," in *Diffusion in Gases, Liquids and Electrolytes · Gases in Gases, Liquids and their Mixtures*, M. Lechner, Ed. Springer Materials, 2007, vol. 15A, no. 1, pp. 1439–1443. doi:10.1007/978-3-540-49718-9_1082

[191] W. He, W. Lv, and J. Dickerson, *Gas Transport in Solid Oxide Fuel Cells*, ser. SpringerBriefs in Energy. Cham: Springer International Publishing, 2014. doi:10.1007/978-3-319-09737-4

[192] B. G. Higgins and H. Binous, "Binary Diffusion Coefficients for Gases," 2013. [Online]. Available: http://demonstrations.wolfram.com/BinaryDiffusionCoefficientsForGases/

A

Appendix: material property characterization

A.1. Membrane deflection offset

As explained in the text in subsection 4.1.1, an offset was found in the pressure bulging of the bottom chip. To get an idea of where this offset could come from, simple 1-dimensional calculations on arc length are presented. The geometry is shown in figure A.1. From the figure, the following relations can be deducted:

$$r\sin(\alpha) = \frac{830}{2} \qquad \text{gives} \qquad \alpha = \arcsin\left(\frac{830}{2r}\right) \tag{A.1}$$

$$d = r - r\cos(\alpha), \tag{A.2}$$

with r the radius in µm of the circle that is fitted through the deflected membrane, α the angle in radians, 830 µm is the bottom membrane width edge length, and d the membrane deflection magnitude in µm. From these relations it follows that the offset of $d = 2.4$ µm, corresponds to $r = 35\,881$ µm and $\alpha = 0.0116$ rad (or 0.663 deg). The arc length is a part of the perimeter of a circle, given by

$$\text{arc length} = 2\alpha r. \tag{A.3}$$

The arc length is found to be 830.0185 µm. This means an additional 18.5 nm arc length already results in 2.4 µm membrane deflection. Optical inspection of the chip that was used for the membrane deflection already shows that the membrane is not completely flat; it looks a bit bumpy. So the likely explanation is that the membrane is not stretched, maybe due to how this membrane was fabricated, maybe due to degradation, as this chip has been used for various experiments that are reported in this thesis. Deeper analysis is required to find the exact reason. However, it did not affect the temperature calibration, so it does not affect the results in this thesis with significance.

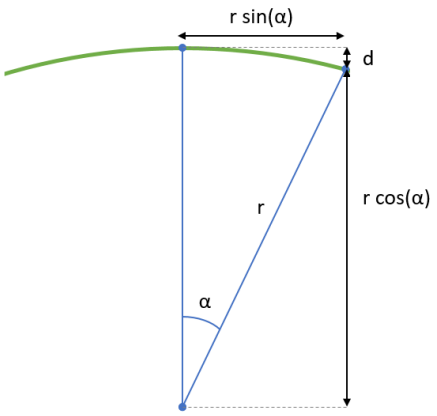

Figure A.1: Schematic of the membrane geometry. The green arc represents the suspended membrane.

A.2. Emissivity

The emissivity of the Microheater was determined using an infrared camera (FLIR A655SC) with an operating range from 100–650 °C. Images of the bottom chip were taken in steps of 100 °C. Figure A.2 shows an image of the heater at 600 °C. The data was fitted using the Stefan-Boltzmann law. An emissivity was found of 0.227 with an error of 0.005.

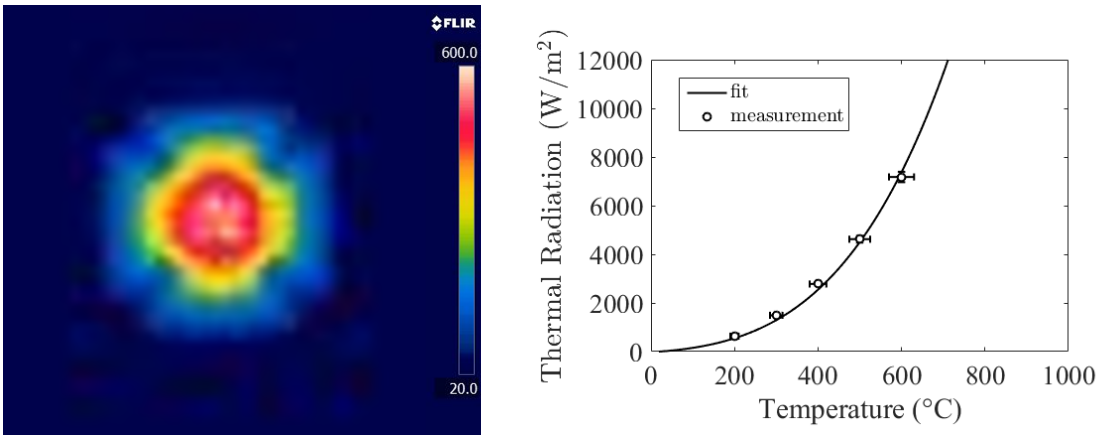

Figure A.2: (left) Infrared camera image of the bottom chip set to 600 °C. **(right)** Thermal radiation data points measured by the infrared camera. The data was fitted using the Stefan-Boltzmann law.

A.3. Thermal conductivity of nitrogen and helium

As explained in the theory of subsection 2.2.4, bulk gas properties can be assumed with high accuracy if the Nanoreactor is used with a gas pressure of 1 bar. The temperature dependent thermal conductivity that was used in the finite element model is given in figure A.3.

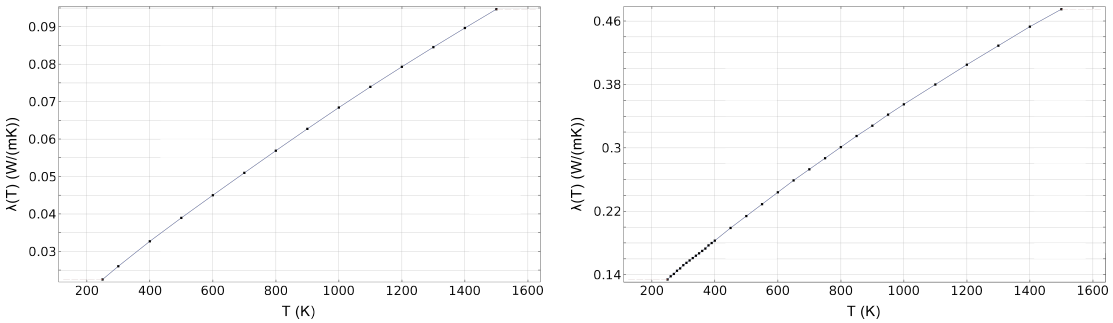

Figure A.3: (left) Temperature dependent thermal conductivity of nitrogen that was used for finite element analysis. The data was obtained from the Dortmund Data Bank [159]. **(right)** Temperature dependent thermal conductivity of helium that was used for finite element analysis. The data was obtained from Vargaftik *et al.* [160] who obtained it through combining results from multiple sources.

A.4. Coefficient of thermal expansion

The coefficient of thermal expansion (CTE) as function of temperature turned out to be necessary to model membrane deflection more accurately. The CTE of bulk silicon nitride are shown in the table of figure A.4 [189]. These values were taken as a starting point for the modeling of temperature dependent membrane deflection. The average values of the two silicon nitride types were scaled and carefully tuned to match the experimental data. The trend, as reported in literature, is maintained to stay in agreement with the governing physics.

Temp (°C)	Material	
	SN47	SN5P
50	1.5	1.6
100	1.9	1.9
200	2.4	2.2
300	2.9	2.9
400	3.3	3.2
500	3.4	3.7
600	3.6	3.8
700	3.7	3.9
800	3.6	4.0
900	3.9	4.2
1000	3.5	4.9

Figure A.4: Temperature dependent coefficient of thermal expansion for two types of silicon nitride in 10^{-6}/°C as reported by Swab *et al.* [189].

A.5. Diffusion of nitrogen and helium

Diffusion of nitrogen and helium follows the theory has been described before in subsection 2.2.5. There it was derived that the diffusion coefficient scales with temperature and pressure according to $D \propto T^{\frac{3}{2}} P^{-1}$. However, the experimental data that Winkelmann [190] has collected from various sources does not completely follow this trend. It turns out that the theory was not complete yet; the temperature dependence of the collision integral was not taken into account [191, 192]. Therefore, the experimental data was fitted with

$$D = \mathrm{A} \cdot T^{\alpha} \tag{A.4}$$

in which A is a constant, T the temperature in K, and α the temperature power. The data fit-curve found $A = 3.097410^{-9}$ and $\alpha = 1.75$. Figure A.5 shows the data set fitted with and without the correction from the collision integral. These parameters are used in the simulation results shown in this thesis.

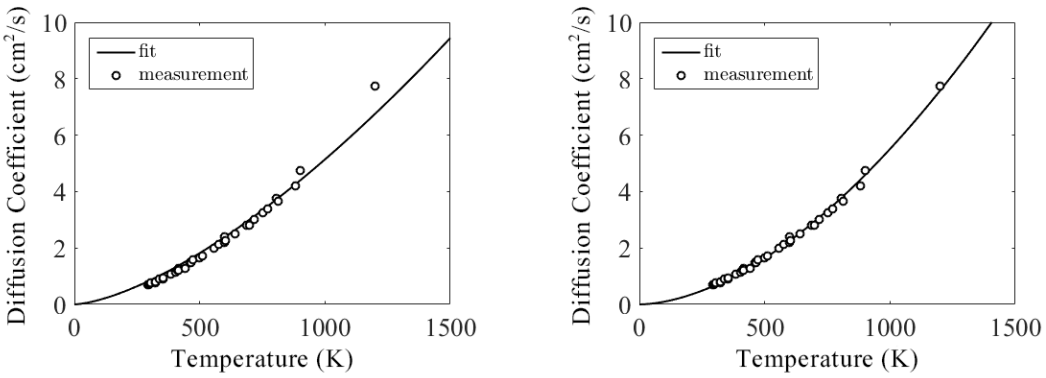

Figure A.5: (left) Temperature dependent diffusion fitted with the dependency as prescribed by equation 2.21. **(right)** Temperature dependent diffusion fitted including the contribution from the collision integral. Data obtained from Winkelmann [190].

B

Appendix: experimental data

B.1. Mechanical stability

For the lower limit in varying heater linewidth, the roughness of the edges of the heating spiral were measured, as shown in the figure underneath.

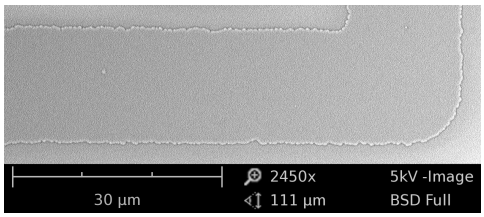

Figure B.1: Roughness on the sides of the heater lines that had to be taken into account when designing the varying heater linewidth; the roughness should not become significant compared to the heater linewidth to avoid high current densities locally.

Another thing, membrane deflection was measured as function of pressure, temperature, and gas flow rate. The results of the latter were not shown in the thesis as it was found to be insignificant. The results are shown in the figure underneath.

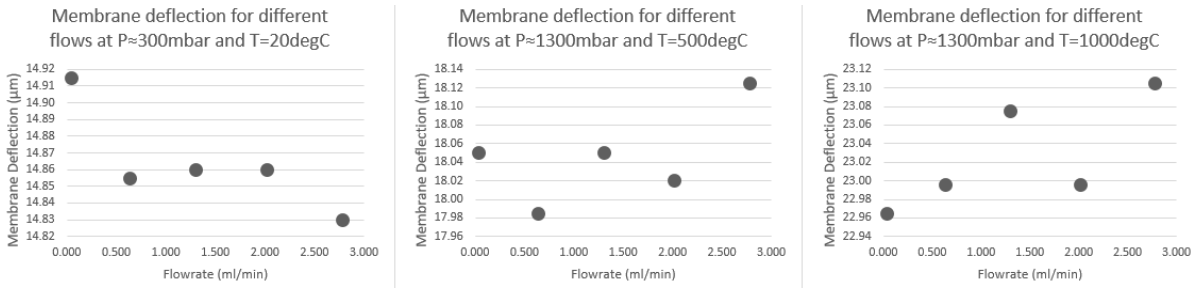

Figure B.2: Bottom membrane deflection as function of gas flow rate for ~300 mbar at room temperature, 500 °C, and 1000 °C. The pressure has not been corrected for the atmospheric air pressure, but the results were measured subsequently so the absolute results may be inaccurate, but relative to each other they are accurate. Note that the variations between the data points are within the error bars (not drawn, see appendix D).

B.2. Temperature and heat

As reported in subsection 3.2.3, the top chip temperature was going to be confirmed by a TEM experiment. The results were not included in the main part of the body because they were inconclusive. They confirmed indeed that the top reaches approximately the same temperature as the bottom chip, but the exact temperature difference could not be extracted.

Au-Ge nanowires were deposited on both the bottom and top chip. The Au-Ge nanowires were provided by Stanford University. According to Adhikari *et al.* [186], the Au-Ge nanowires have a eutectic melting point which is 349 °C for a 40 nm wire diameter. This exact transition temperature could not be reproduced, which may have to do with the accuracy in temperature calibration (~95%), the limited homogeneity over the electron transparent windows (~94%), the adhesion between the sample and the chip or the presence of nitrogen gas. To conclude on the absolute temperature, further analysis is required.

However, the experiment is suitable for the purpose of the experiment: determining the difference in temperature between the bottom and top chip. The transition happened for both the bottom and top chip between 430–450 °C, as can be seen in figure B.3. A slightly lower transition temperature was expected at the top chip; considering the windows on which the nanowires were located, the Nanoreactor model predicts a difference of about 30 °C. Part of the discrepancy may be due to the different nanowire diameters; the bottom nanowire has a diameter of 78 nm and the top nanowire a diameter of 55 nm. Extrapolating the results of Adhikari *et al.* [186] this size difference explains a temperature discrepancy of about 10 °C. No explanation has been found for the remaining 20 °C difference. A repetition of this experiment is required to see if the difference is reproducible. However, the main point is confirmed: the top chip reaches (almost) the same temperature as the bottom chip, proving that the high temperature homogeneity that should be expected from the chip is maintained through the thickness of the gas layer.

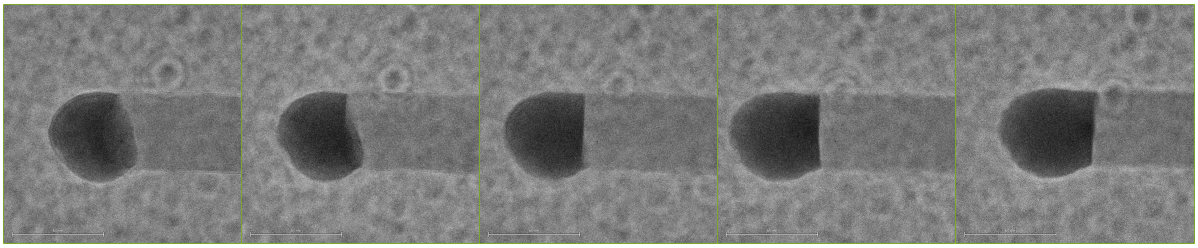

(a) Top 410 °C **(b)** Top 420 °C **(c)** Top 430 °C **(d)** Top 440 °C **(e)** Top 450 °C

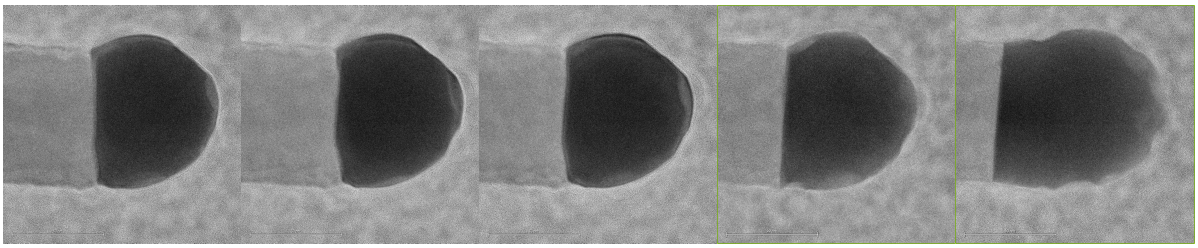

(f) Bottom 410 °C **(g)** Bottom 420 °C **(h)** Bottom 430 °C **(i)** Bottom 440 °C **(j)** Bottom 450 °C

Figure B.3: TEM images of the Au-nanoparticle on the Ge-nanowire for various temperatures indicated with the figures. The top row contains the images of the nanowire on the top chip and the bottom row contains the images of the nanowire on the bottom chip.

B.3. Gas switching time

To determine gas switching time, the dependence of power consumption as function of gas composition, temperature, pressure, and flow rate have to be known. The intention was to experimentally determine the gas switching time of the Nanoreactor. However, after the first experimental results were compared to the model and to theory, it was found that gas switching time was limited by the experimental setup rather than the Nanoreactor itself. Therefore, the experimental determination of gas switching time was discontinued. The preceding characterization of power consumption, which was used to translate changes in power consumption to gas composition, are presented in the figures shown underneath. In addition, these graphs show

the potential that the Nanoreactor has to function as an actuator (providing stimuli) and also as a sensor (detecting gas compositions, or measuring exothermic/endothermic reactions through changes in power consumption). The graphs in the figures are not always very smooth, the reason for this is likely due to gas bottles had to be switched prior to the experiments. The experiments were spread over multiple days, it appears that on the day when the 40 and 50 % nitrogen content data points were obtained, the gas supply system was not properly flushed. Ideally, these experiments should be repeated. However, experimental and modeled gas switching should not be compared, accurate characterization is not that important. To filter out some of the error, the data was fitted, as explained in subsection 4.1.4.

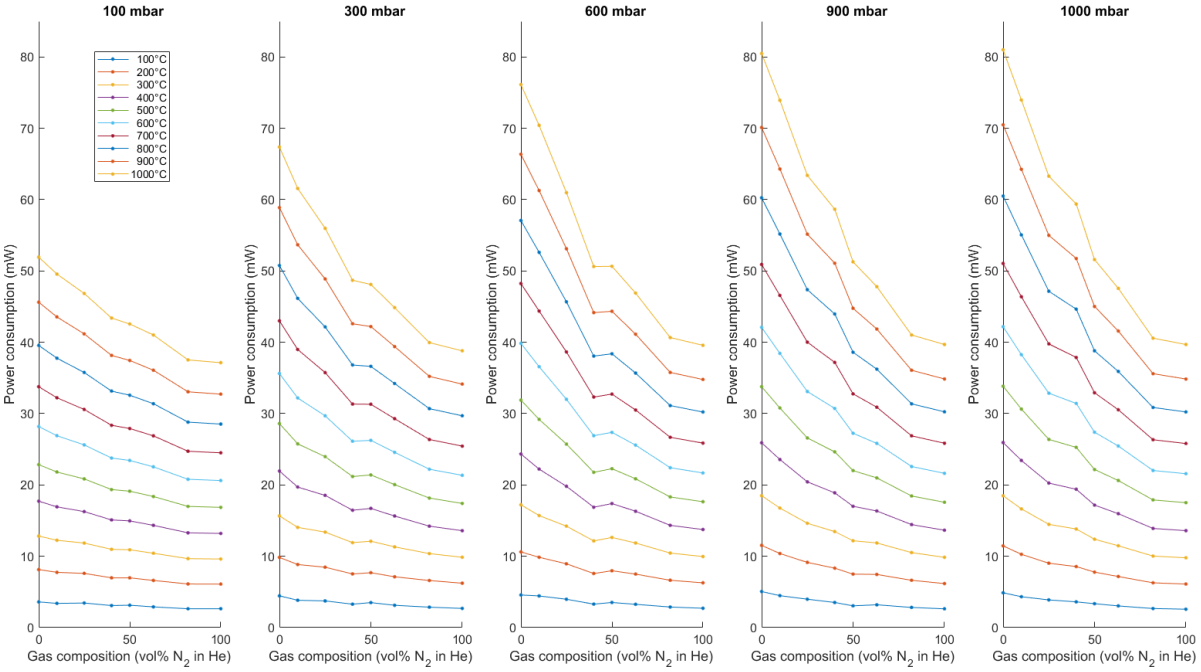

Figure B.4: Power consumption as function of gas composition, categorized per pressure.

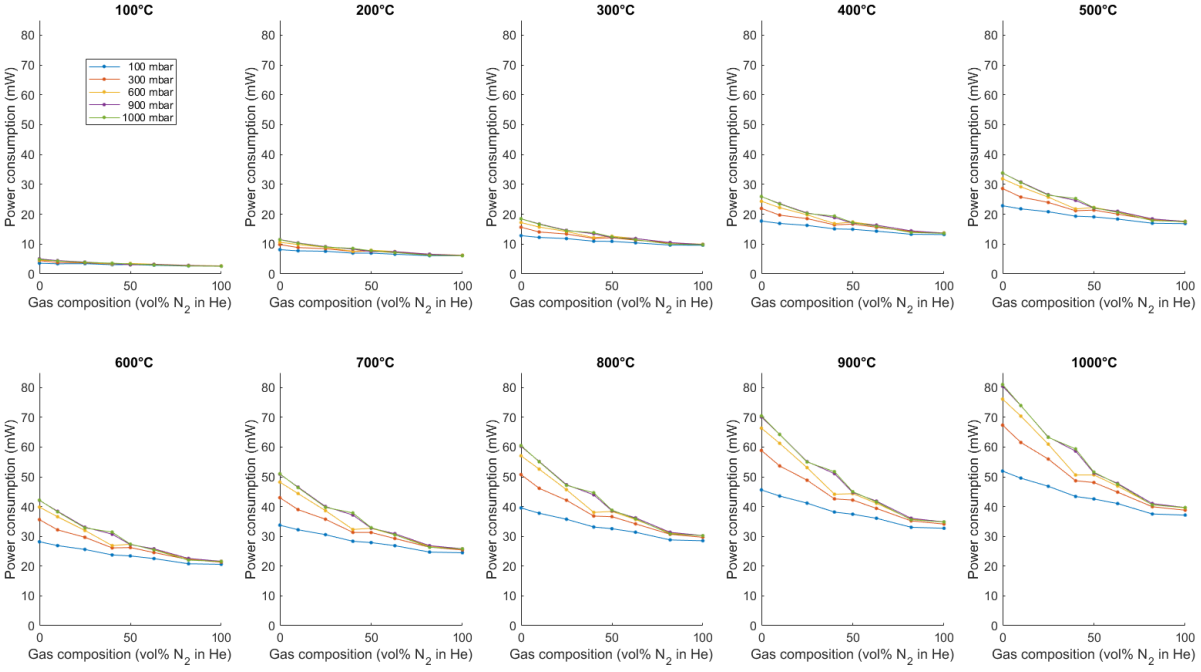

Figure B.5: Power consumption as function of gas composition, categorized per temperature.

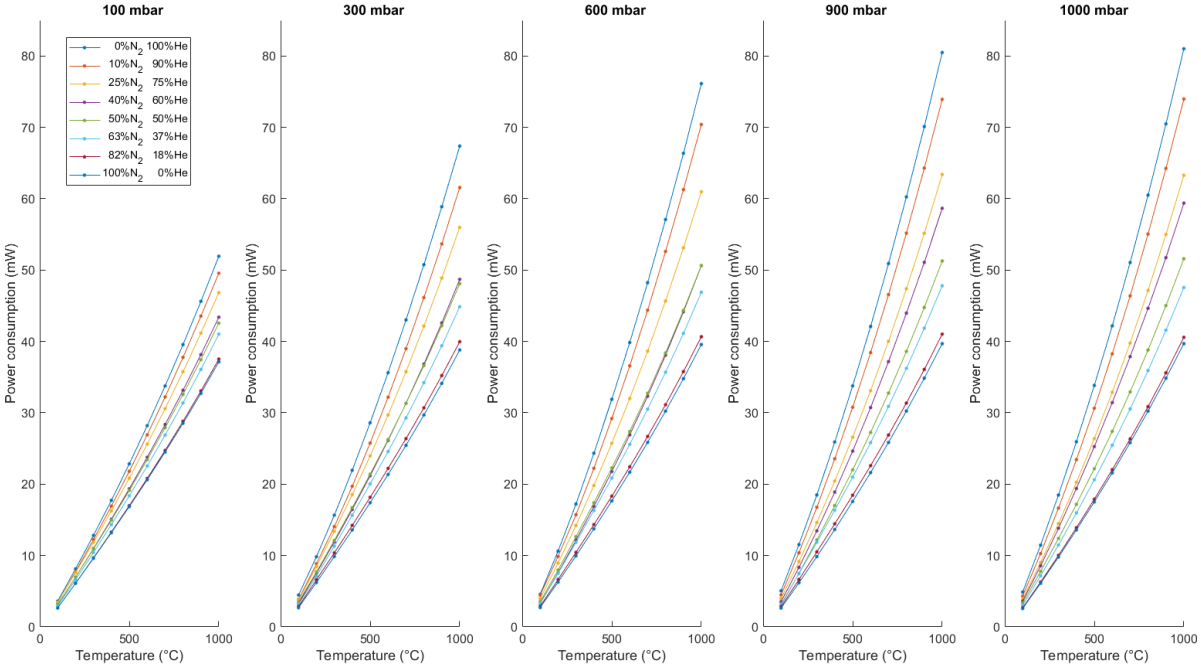

Figure B.6: Power consumption as function of temperature, categorized per pressure.

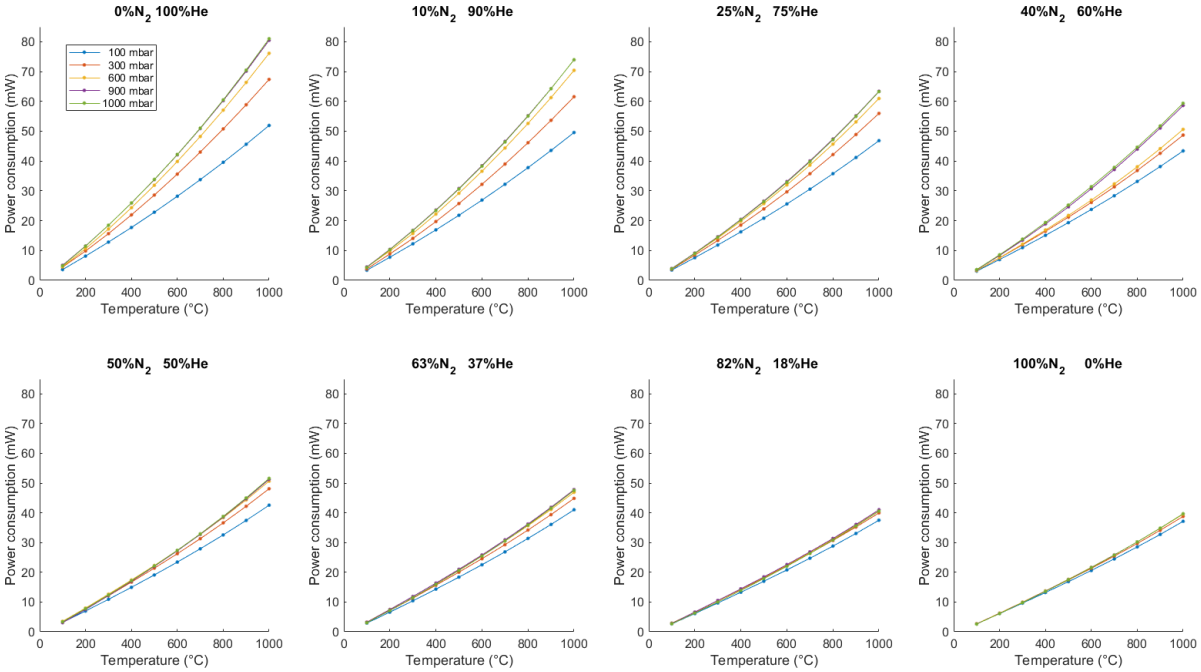

Figure B.7: Power consumption as function of temperature, categorized per gas composition.

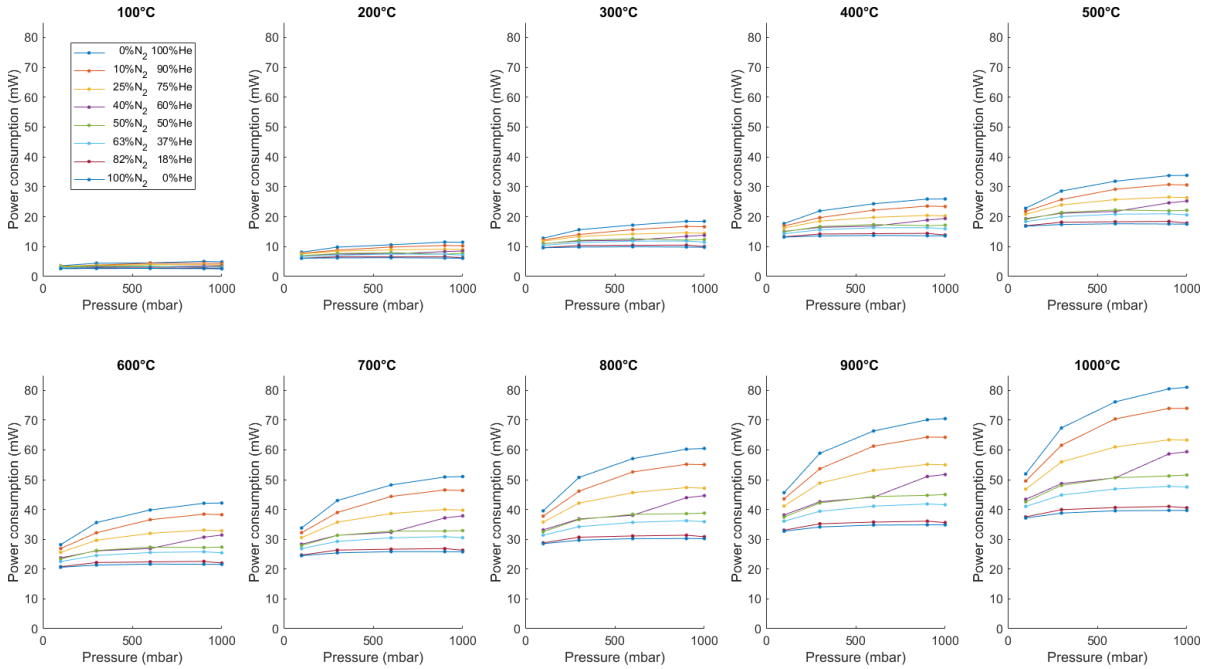

Figure B.8: Power consumption as function of pressure, categorized per pressure.

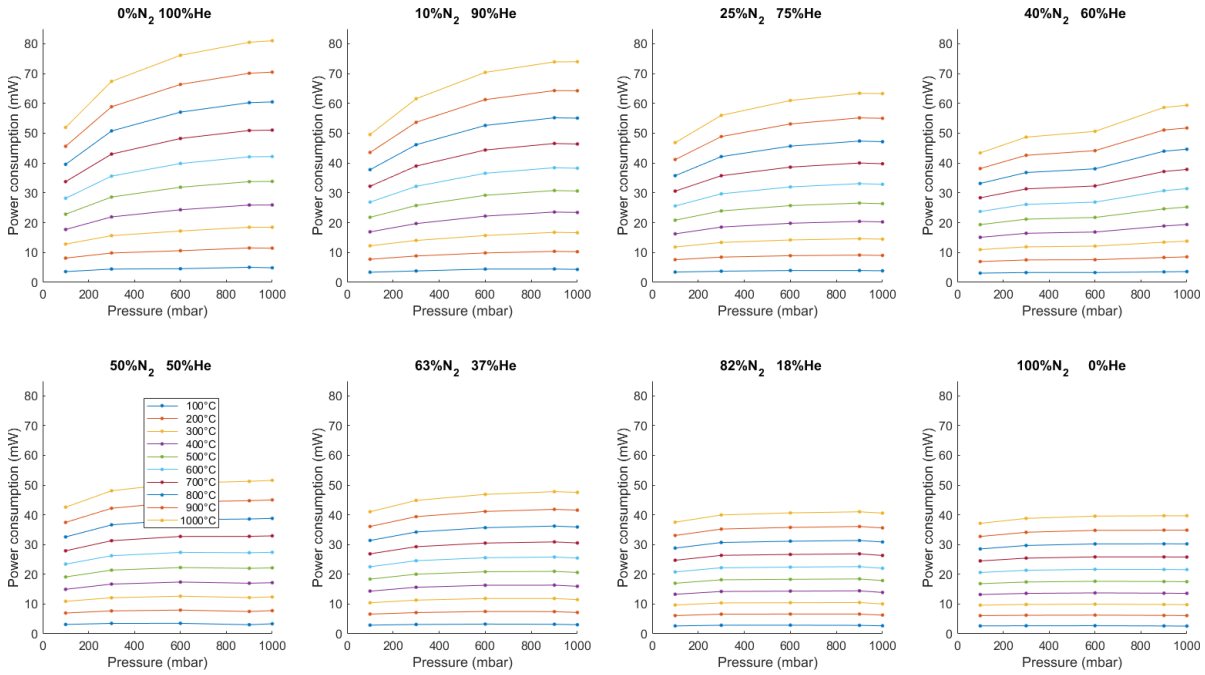

Figure B.9: Power consumption as function of pressure, categorized per gas composition.

C

Appendix: modeling and simulation data

This appendix contains simulation results that do not directly relate to the performance of the Nanoreactor, but do describe the physics that governs it. The results in this chapter come from arbitrary cases that are typical for the Nanoreactor. These cases are not always specified. The intention of these figures is to illustrate which mechanisms have constantly been taken into account in the optimization steps.

C.1. Mechanical stability

The stress levels are expected to decrease when smaller membrane sizes are adopted. This was verified using a simulation:

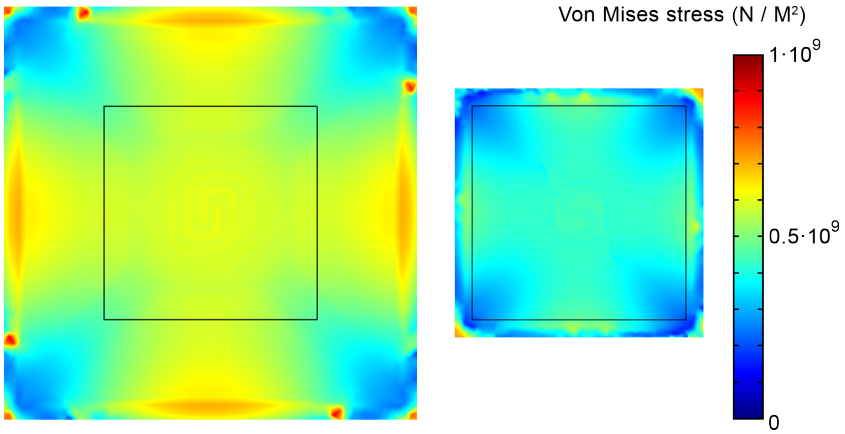

Figure C.1: Von Mises stress in the **(left)** current membrane and **(right)** optimized membrane.

C.2. Temperature and heat

Various electro-thermal aspects were monitored to ensure no current crowding and hotspots will occur in the optimized heater design. For these purposes, current, voltage, Joule heating, and heat flux analyses were performed for various temperature, pressure and gas scenarios. An impression of these intermediate studies are given in the figures underneath. Moreover, the temperature settling graphs are provided that on which the numbers in subsections 4.1.3 and 4.2.3 are based on.

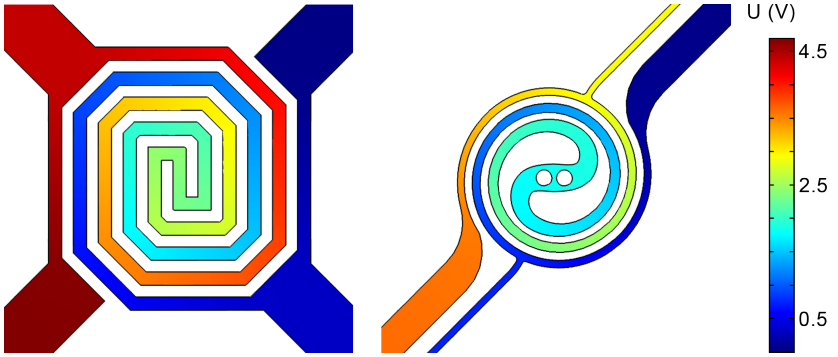

Figure C.2: Electric potential for a typical scenario of the **(left)** current heater and **(right)** optimized heater.

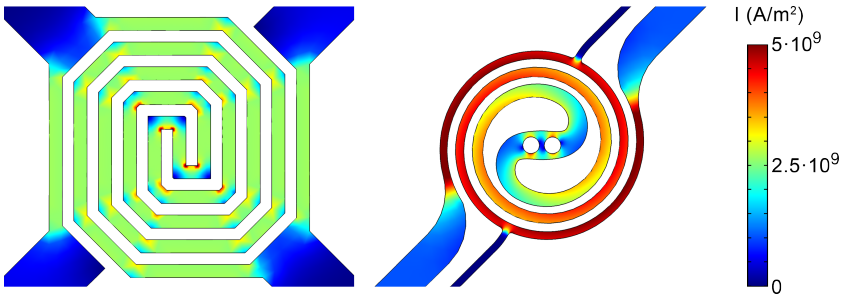

Figure C.3: Current density for a typical scenario in the **(left)** current heater and **(right)** optimized heater. Note the current crowding in the sharp corners in the center of the current heater and the much more uniform current density over the width of the optimized heater lines.

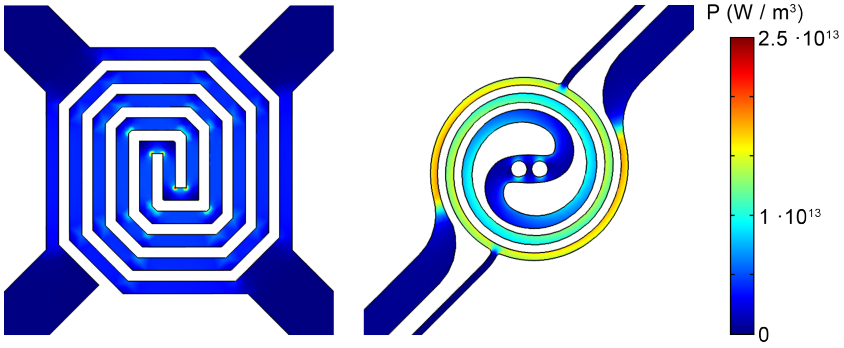

Figure C.4: Joule heating for a typical scenario in the **(left)** current heater and **(right)** optimized heater. Although it is hard to see, the sharp corner sin the current heater design reach the dark red peaks of the highest Joule heating. these spots experience intense Joule heating due to current crowding. The optimized design has a much smoother Joule heating distribution, especially on the outer heating circle to compensate the heat losses, and to get the whole heater at a high and homogeneous temperature.

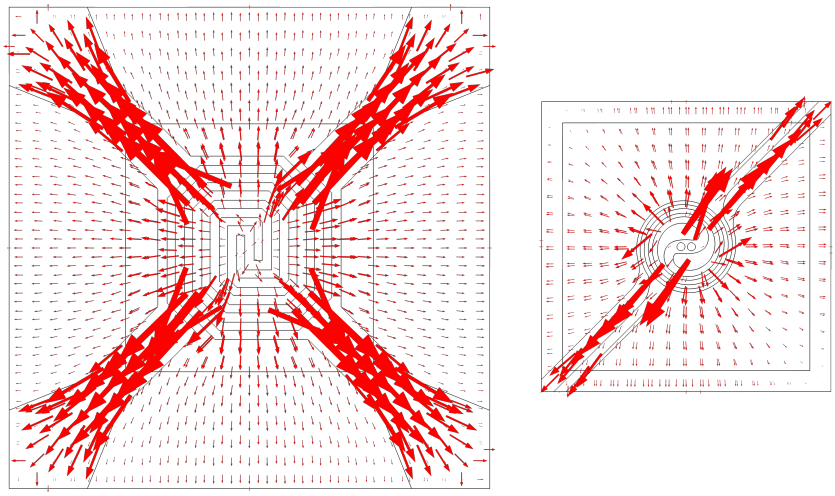

Figure C.5: Heat conduction for a typical temperature in the **(left)** current membrane and heater design and the **(right)** optimized membrane and heater design. Note how the optimized electrical probes contribute a lot less to the heat conduction. These images apply to vacuum conditions.

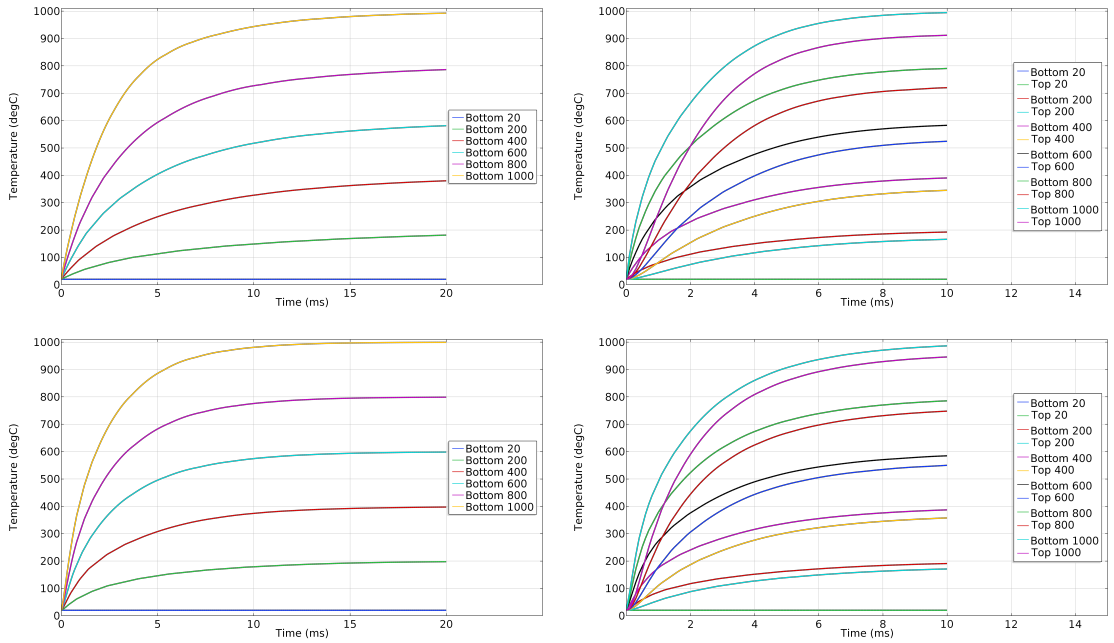

Figure C.6: Temperature settling graphs for **(topleft)** the current Nanoreactor in vacuum, **(topright)** the current Nanoreactor in nitrogen, **(bottomleft)** the optimized Nanoreactor in vacuum, and **(bottomright)** the optimized Nanoreactor in nitrogen.
These results are obtained from simulations by providing a voltage at the heating probes at time zero. Therefore, these results do not present the actual real-life performance in which closed-loop feedback control is used on the heater resistance, but they do provide good insights in how temperature settling changes with the design and they given an order of magnitude estimate of the settling time. Note that for the nitrogen cases, the top chip temperature is also included. As is evident, the top chip temperature traces the bottom chip temperature with a small delay related to the time that the heat needs to travel through the gas layer.

C.3. Gas flow speed

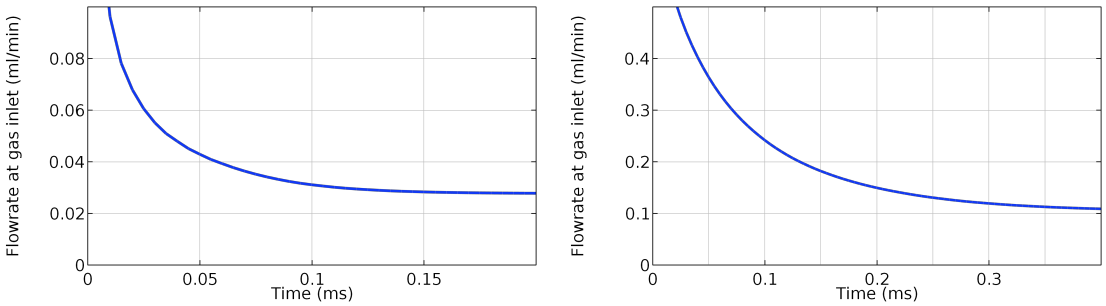

Figure C.7: Time dependent gas flow rate for **(left)** the current Nanoreactor design and **(right)** the optimized Nanoreactor design. After applying an instantaneous pressure gradient among the inlet and outlet of 100 mbar, a settling time is found of 0.11 ms (for the flow rate to reach within 10 % of its final value). Note that the x- and y-axes are different for both figures.

C.4. Gas switching time

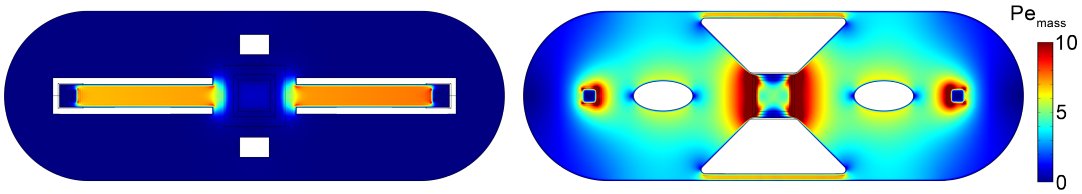

Figure C.8: Péclet number for mass transfer distribution of helium-nitrogen for **(left)** the current Nanoreactor design and **(right)** the optimized Nanoreactor design. To calculate Péclet the local gas flow speed and a characteristic length of 1 mm were used.

D

Appendix: error analysis for experiments

D.1. Nanoreactor calibration and degradation

It has been discussed before, in subsection 4.1.3, that it was determined that the Raman temperature accuracy is better than 1 %. At higher temperatures, the error becomes larger due to peak broadening and spreading of the intensity [188]. Next to this effect, it was reported in literature that the laser intensity can interfere with the temperature measurement [188]. This was confirmed: if high laser intensities are used the four-point-probe detects temperature fluctuations of a few °C. The laser intensity was reduced until this error got below 0.1 °C. The accumulation time was increased to obtain enough Raman scattering data for reliable measurements. This high-accuracy calibration method requires to put silicon particles on the chip, which is undesirable for other experiments. A set of 5 chips from the same wafer were individually calibrated with infrared pyrometry to reach an accumulated error of 3 % at most, which was considered sufficient for the purpose of this project.

The Raman laser positioning error is estimated to be 3 µm (2 standard deviations). This error does not originate from the Raman itself, which has a resolution of about 0.5 µm [178], but from the position read-out which was done using optical microscopy.

In literature, it was found that heater degradation affects the temperature read-out accuracy over time. This graph by Mele *et al.* [29] is shown in figure D.1. The heating control unit that was used for the experiments compensates for potential resistance degradation at high temperature by also monitoring and correcting the power consumption. However, to confirm that the chips were not suffering from temperature inaccuracies, re-calibrations were done in between and after experiments. It was found that the Nanoreactor did not experienced degradation due to high-temperature operation or many pressure cycles. While not exceeding a 1000 °C temperature range, it was found that the heater degradation due to temperature was insignificant. A dedicated one-day test with 100 pressure cycles from low vacuum to 1 bar was found not to have any affect on the temperature accuracy.

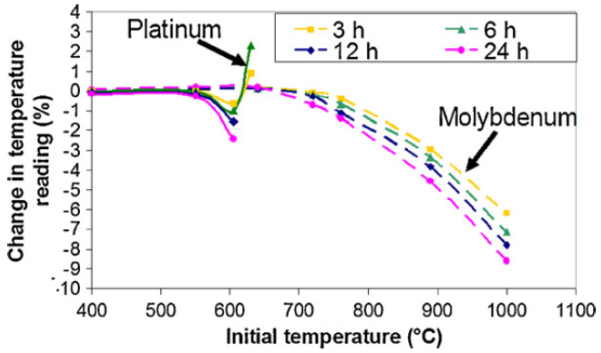

Figure D.1: This figure was obtained from Mele *et al.* [29]. It shows the change in temperature read-out as a result of heater degradation after hours of high-temperature operation, for their Microheater.

D.2. White light interferometry

A small statistical error analysis was done to determine the accuracy of the WLI measurements. It was done for the bottom and top chip separately, as their different membrane size and topography result affect both the amplitude and the error differently. The procedure was as follows: Membrane deflection was measured three times for an overpressure of 300, 600 and 900 mbar at temperatures of 100, 500 and 1000 °C (so a total of 27 points). The 27 data points were determined in a random order. An overall standard deviation was determined. Since different scenarios are combined, the average was determined for each of the 9 scenarios. This analysis does not fully complies with the official procedure for statistical error analysis, but this is also not necessary as long as it is confirmed that the error is small and it is not underestimated.

For the bottom membrane the standard deviation was found to be 248 nm. To see where this error comes from, various contributions were analyzed. The read-out error due to topography and surface roughness was empirically found to be 87 nm. Although the WLI setup is on a anti-vibration table, some vibrations were observed. Judging by the distance the fringes vibrate, and assuming a white light wavelength of 600 nm, the error from vibrations is determined to be up to 150 nm. The WLI was calibrated using a dedicated calibration sample. The software provided a calibration error that corresponds to 20 nm. The contribution that could potentially coming from the gas supply system, because of pressure and flow accuracies was found to be too small to distinguish it from the errors caused by topography and vibrations.

The same analysis was done for the top membrane the standard deviation was found to be only 48 nm. The contribution from topography was found to be 50 nm at the most. Vibrations can account for up to 38 nm, and the calibration error remains up to 20 nm. Since the contributions appear worse than the actual statistical result, it can be concluded that the determined contributions are adequate and represent the worst cases.

E

Appendix: error analysis for modeling and simulations

Some simplifications and assumptions are made to enable modeling. Additionally, small errors are introduced by the limited element quality. Generally speaking, minor deviations are acceptable, as long as the trends are clear. In the end, the purpose of the model is to help understand the physics and to make reliable predictions on what influences the performance of the Nanoreactor, such that it becomes clear how the Nanoreactor can be optimized.

E.1. Simplifications and assumptions

The model includes some simplifications of which potential errors are not taken into account:

- The electron transparent windows are not taken into account for temperature homogeneity analysis. In subsection 2.1.4 it was determined that in the very worst case, in vacuum and with large samples, the error can go up to 1 % at the highest temperatures. However, the Nanoreactor contains gas which, as has been shown, smoothens the temperature profile especially at high temperatures. Therefore, it can be safely assumed that the error for the Nanoreactor is less than 0.1 % at the worst.
- The surfaces of the Nanoreactor are assumed to be atomically smooth such that a no-slip condition applies to the gas flow in the Nanoreactor. This assumption is quite accurate, as in reality the surface roughness is on the single nanometer scale, which is insignificant to the 5 µm thick gas layer.
- For the gas behavior, bulk material properties are assumed. However, in the theory it was shown that for gases like helium, molecular flow effects may start occurring at very high temperatures. The effects are minor, as proven by the small discrepancy between experimental and simulated power consumption. However, at high temperature and low pressure, these effects may not be negligible anymore. Since low-pressure cases are not considered, the assumption is valid for the results presented in this thesis.

E.2. Mesh quality analysis

With mesh quality, gas flow turned out to be the most demanding. As all elements have to be connected to their neighboring elements, having a good quality for the gas layer ensures good element quality for the other types of physics.

The effect on the element quality was analyzed by simulating gas flow as function of the number of mesh elements in the thickness of the gas layer, for different pressure gradients. The analysis was done on a minimum example geometry of 200 x 100 x 5µm. As shown in figure E.1a, some data points are missing for odd-numbered element numbers. For these cases the model did not converge. The minimum amount of elements over the gas layer thickness was found to be 4. The graphs show that 4 elements result in a slight underestimate of the gas flow rate as compared to the much higher number of elements. The error was determined to

be 1.3 % for a pressure gradient of 100 mbar, which is the number used in the gas flow analyses throughout this thesis. Choosing 6 elements would reduce the error to 0.2 %, but this turned out to be too memory demanding for the Nanoreactor, in combination with other physics. The same analysis has been done for gas flow speed. The results are shown in figure E.1b. Here, it matters whether an even or odd number of elements is chosen. This makes sense; an even number of elements has a node exactly in the center of the Poiseuille flow profile and will therefore find a larger flow speed. 4 elements turned out to be accurate within less than 1 % from 10 elements.

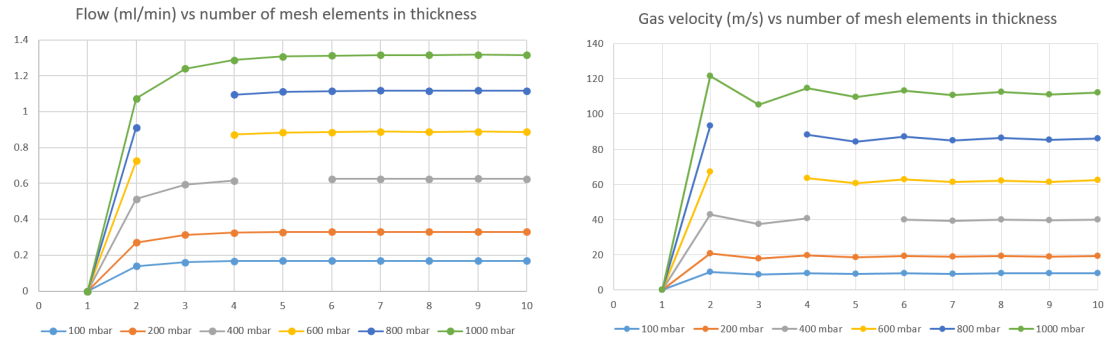

Figure E.1: Gas flow rate and gas flow speed as function of the number of mesh elements in the thickness of the gas layer, for different pressure gradients

Next to the mesh quality for thickness, the effect of lateral element quality was analyzed regarding gas flow. This was done by COMSOL's default meshing options: extra coarse, coarser, coarse, normal and fine (finer already became too memory demanding for this geometry). These meshing options correspond to 1, 2, 3, 4 and 5 on the x-axis of figure E.2. The effect of the lateral element size seemed to affect the maximum gas flow velocity in the model. However, this analysis was done on a mimic of the actual Nanoreactor geometry, without the outer regions, but with the gas guiding spacers. The maximum gas velocity increases with element quality because of gas flow line concentrations at the corners of the spacers. This effect can also be observed in figure 4.4c. However, the flow speed at these points is not that interesting so the quality analysis should be concluded on the flow rate instead. Here, it follow that the difference between normal and fine is 1 %. Since the difference is getting smaller with every quality increase, it is assumed that it does not improve much further beyond fine. Therefore, fine is selected for the gas flow analysis.

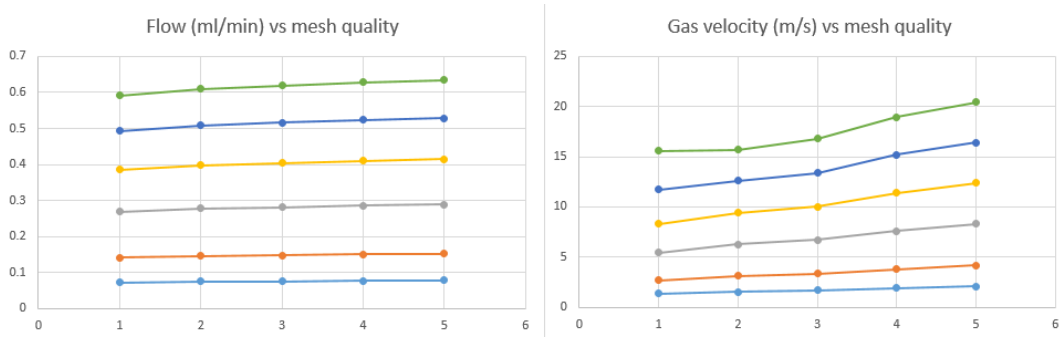

Figure E.2: Gas flow rate and gas flow speed as function of the lateral mesh quality of the gas layer as determined by COMSOL's automatic meshing. The different lines are for different pressure gradients. The legend is the same as in figure E.1

From both these analyses, it can be concluded that gas flow rate and gas flow speed are determined with an approximate 2.3 % error to the actual value. The effect of this is neglected in the results, as this small amount of additional flow will not be significant enough to reduce homogeneity for gas flow. It may make gas switching faster by 2.3 %, but considering the order of magnitude improvement that is obtained, this difference is insignificant.